Thesis report

Wind turbine main bearing degradation monitoring using physics-based analysis of SCADA data

Ilkin Mammadov

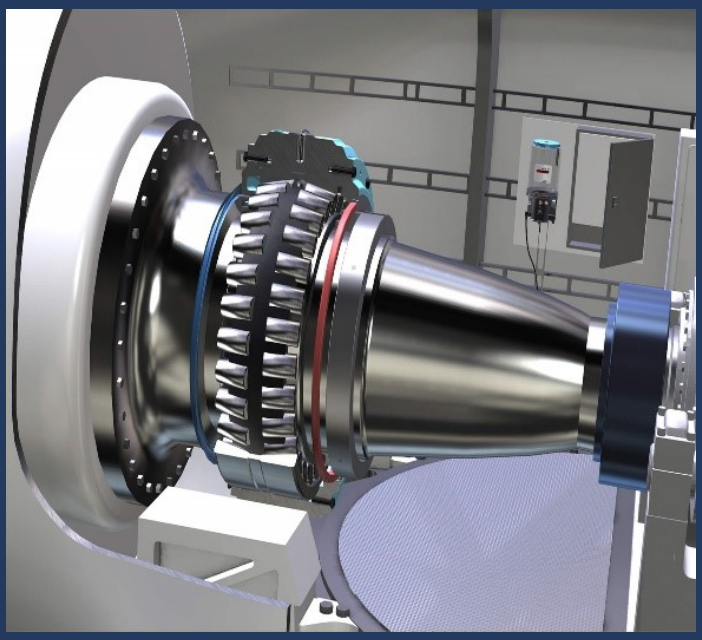

TU Delft

Thesis report

Wind turbine main bearing degradation monitoring using physics-based analysis of SCADA data

Thesis report

by

Ilkin Mammadov

to obtain the degree of Master of Science
at the Delft University of Technology
to be defended publicly on February 26th, 2024 at 14:00 CET

Thesis committee:	
Chair:	Prof. Dr. Simon Watson
Supervisors:	Dr. Donatella Zappalá
	Ph.D. Ali Eftekhari Milani
External examiner:	Dr. Márcia Baptista
Project Duration:	November, 2022 - February, 2024
Student number:	5475600

An electronic version of this thesis is available at `http://repository.tudelft.nl/`.

Faculty of Aerospace Engineering · Delft University of Technology

[1] Figure on the cover page taken from [1]

Preface

This master's thesis marks the end of my studies in Sustainable Energy Technology at the Technical University of Delft. Throughout my academic journey, I have been deeply passionate about sustainability and the role of wind energy in addressing the energy transition. Writing this thesis has been a constant learning process. I would like to thank the people who have supported and helped me to complete it.

I would like to express my deepest gratitude to my supervisor, Dr. Donatella Zappalá, for the time she dedicated and for her invaluable guidance throughout this thesis project. Moreover, I extend my appreciation to the Ph.D. candidate Ali Eftekhari Milani for his consistent support and feedback. Furthermore, I would like to thank Dr. Edward Hart from the University of Strathclyde for sharing the data for this research. I also thank Prof. Dr. Simon Watson and Dr. Marcia Baptista for joining my thesis committee.

I would like to thank my family for their support. Lastly, friends I made during my time in Delft, I would like to thank you for this time.

Abstract

Wind energy is a rapidly growing renewable energy source and a dominant driver in the energy transition. Reducing costs associated with wind energy increases its competitiveness and enables wider adoption of this renewable energy source. Notably, for onshore wind farms, operation and maintenance (O&M) accounts for approximately 25% of the lifetime costs, while for offshore farms, this number reaches up to 35%. This emphasizes the need for a condition-based maintenance (CBM) strategy in order to reduce O&M costs. To implement CBM, it is necessary to conduct fault detection and degradation trend monitoring. Fault detection enables the identification of malfunctioning components in advance, while monitoring the degradation trend allows panning the maintenance of the component.

The main bearing is a critical wind turbine drivetrain component, and its failure can cause the turbine shutdown and expensive repair. As the main bearing degrades, its temperature increases, indicating health deterioration of the component. Various methods proposed in the literature employ physics-based normal behavior models (NBMs) using Standard Supervisory Control And Data Acquisition (SCADA) data as input to energy conservation-based equations to model the main bearing temperature. These methods analyze the difference between the measured and the modeled temperature, referred to as residual. These residuals are used as health indicators (HIs) for assessing the condition of the component.

Physics-based NBMs utilizing SCADA data have been successfully used for fault detection of the main bearing. However, the application of these methods for degradation trend monitoring have not yet received attention. The primary reason for the premature failure of wind turbine components is attributed to the variability of the wind conditions. However, current NBM methods are based solely on the mean value records and do not consider the variations within the 10-minute time frame. Furthermore, seasonal fluctuations in operating conditions can adversely affect the obtained degradation trend.

The main objective of this thesis is to improve physics-based NBM employing SCADA data to monitor the degradation trend of the main bearing. The proposed approach uses a physics-based NBM available in the literature as the baseline. It aims to increase the monotonicity and reduce the dispersion of the developed HI to enable accurate degradation trend monitoring. To achieve this objective, the proposed method takes into account seasonal variations and variability of operating conditions within the 10-minute SCADA time frame when modeling the main bearing temperature. To mitigate the impact of seasonal changes on the HI, the proposed method develops multiple physics-based NBMs corresponding to monthly time windows. To take into account the variability of the operating conditions, the main bearing temperature is modeled by performing a Monte Carlo simulation using the SCADA data mean and standard deviation values. In this case, the HI is defined by the data density within a threshold region. Two case studies are conducted to demonstrate the advantages of the proposed method compared to the baseline approach. The results show that with the proposed approach, the seasonality effects are reduced by more than 50%, as measured through cross-correlation metric with the ambient temperature, the HI monotonicity increases by 260% as measured by the Mann-Kendall τ monotonicity metric, and the dispersion reduces by 30% and 35%, as evaluated by the Mean Square Error and a noise metric obtained using the Complete Ensemble Empirical Mode Decomposition with Adaptive Noise approach.

Contents

Nomenclature

List of Abbreviations

HI'_{Alt}	Step M density of threshold region, Case Study 2
$HI'_{Res\_Baseline}$	Baseline, Case Study 2
HI'_{Res_M}	Step M, Case Study 2
HI_{Alt}	Step S and Step M density of threshold region, Case Study 1
$HI_{Res\_Baseline}$	Baseline, Case Study 1
$HI_{Res\_S\_M\_B}$	Step S, Step M and Step B, Case Study 1
$HI_{Res\_S\_M}$	Step S and Step M, Case Study 1
HI_{Res_S}	Step S, Case Study 1
ARX	Autoregressive with Exogenous
CBM	Condition-Based Maintenance
CEEMDAN	Complete Ensemble EMD with Adaptive Noise
EMD	Empirical Mode Decomposition
EWMW	Exponentially Weighted Moving Window
FSRC	Full Signal Reconstruction
IMF	Intrinsic Mode Function
LCOE	Levelized Cost of Energy
LSTM	Long short-term memory
MAE	Mean Absolute Error
MAPE	Mean Absolute Percentage Error
MD	Mahalanobis Distance
MK test	Mann-Kendall τ test
MSE	Mean Squared Error
O&M	Operation and Maintenance
ODBN	Optimized Deep Belief Network
RMSE	Root Mean Squared Error
RUL	Remaining Useful Life
SCADA	Supervisory Control and Data Acquisition
SVM	Support Vector Machine
TVF-EMD	Time-Varying Filter-based EMD
WTMB	Wind Turbine Main Bearing

List of Symbols

α	Coefficient of Heating Performance
$\hat{T}_{\text{bear}}$	Modeled Temperature
μ	Friction Coefficient
C^0	Celsius
C_p	Heat Capacity of the Nacelle
K	Kelvin
N	Number of Samples in the Signal
n	Sample Size
$Noise$	Noise of the Signal
$Power$	Power of the Signal
q	Heat Flux
R	Thermal Resistance of the System
R^2	Coefficient of Determination
rad	radian
s	Second
SS_{res}	Sum of Squared Residuals
SS_{tot}	Total Sum of Squares
T_{bear}	Temperature of the Bearing
T_{mes}	Measured Temperature
W	Watt
x_i	Individual Samples of the Signal
y_{pred}	Predicted Value of the Target Variable
y_{true}	Actual Value of the Target Variable

List of Figures

List of Tables

1

Introduction

1.1. Wind energy

Wind energy is a rapidly growing and increasingly important renewable energy source. Nations worldwide are making significant investments in wind energy, substantially increasing installed capacity over the last decade. The global installed capacity for wind power reached 906 GW in 2022, as shown in Figure 1.1, with the highest newly installed capacities in China and the United States, as illustrated in Figure 1.2 [2, 3].

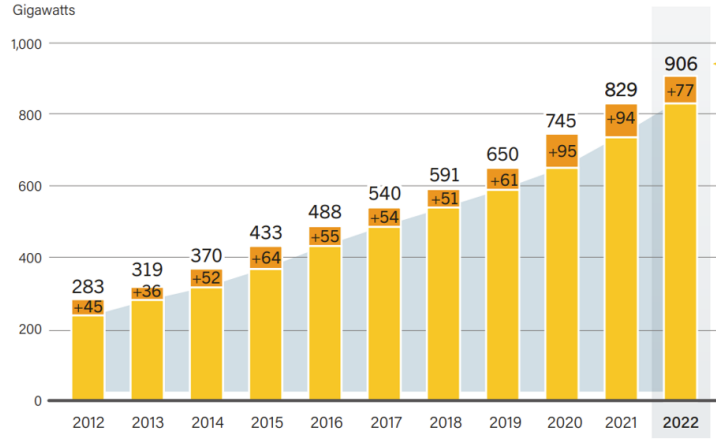

Figure 1.1: Global cumulative wind power installed capacity [4]

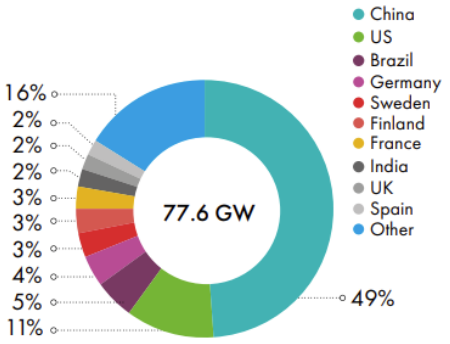

Figure 1.2: Installed wind energy capacity, 2022 [3]

The levelized cost of energy (LCOE) is a metric used to assess the competitiveness of different energy sources. Figure 1.3 shows the global weighted average LCOE for onshore and offshore wind between 2010 and 2022. According to the Renewable Energy Agency report [2], the global weighted average LCOE of onshore wind dropped by 69%, decreasing from USD 0.107/kWh to USD 0.033/kWh. In the same period, for offshore wind farms, it declined from USD 0.197/kWh to USD 0.075/kWh. Learning through employment has been identified as the main factor behind this 50% cost reduction [5].

A positive trend in wind energy cost enables its broader adoption [6]. However, the fraction of global electricity produced by wind energy must drastically increase to reduce the consequences of climate change. According to the International Energy Agency (IEA), an ambitious target of 3100GW of installed wind capacity should be reached to achieve the Net Zero scenario by 2030 [7]. This means that in the next eight years, the installed wind capacity needs to increase 3.4 times. Therefore, to reach the expected targets, further reduction of wind energy's LCOE is essential [8].

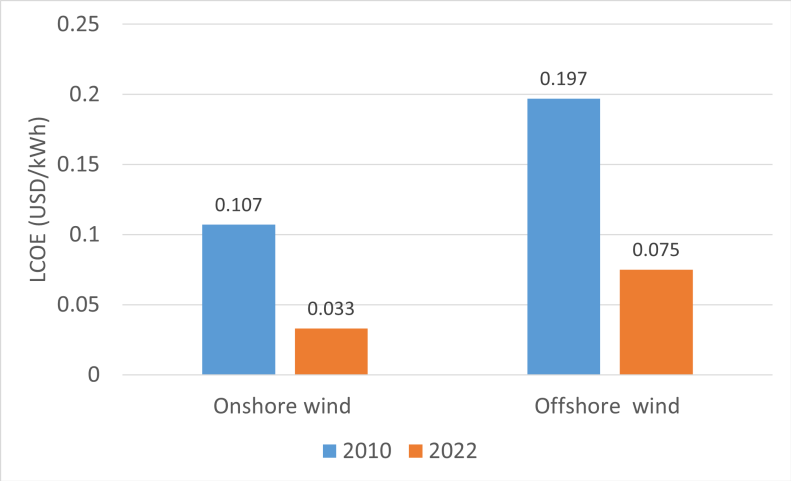

Figure 1.3: Global weighted average LCOE for onshore and offshore wind, adopted from [2]

1.2. Cost of wind energy

When considering wind power as a renewable energy source, understanding its cost is crucial. Wind energy costs include the upfront capital costs such as constructing and installing wind turbines, the ongoing operations and maintenance (O&M), and decommissioning costs [9, 10]. O&M activities, in particular, are a significant cost factor in wind farm projects [6]. Notably, for onshore wind farms, O&M accounts for approximately 25% of the lifetime costs, while for offshore farms, this number reaches up to 35% [11]. O&M costs include labor costs, material costs, transportation costs, fixed costs, and potential revenue losses [12].

O&M costs for wind turbines can vary depending on various factors, such as the size and type of wind turbine, the location, the operating conditions, and the maintenance strategy used. Implementing an effective maintenance strategy can help minimize expenses related to unplanned downtime and repairs while extending the turbine's lifespan [13]. Consequently, this cost reduction contributes to lowering the LCOE of wind energy.

1.3. Maintenance

The three common maintenance strategies are corrective, preventive, and condition-based maintenance [14]. Corrective maintenance, also known as reactive maintenance, is performed after the system's useful life is exhausted. This method may lead to prolonged downtime for wind turbines before they can resume operation, as repairs are undertaken only in response to a fault. Moreover, as no health assessment of the wind turbine is performed, incipient faults may lead to failure of the wind turbine. Considering these factors, corrective maintenance proves to be an unfavorable strategy for wind turbine applications.

Schedule-based preventive maintenance, also known as planned maintenance, involves setting periodic intervals for maintenance to prevent failures regardless of the system's health state [15]. Maintenance intervals are typically determined based on historical field data. A well-known example of preventive maintenance is engine oil replacement, where oil is changed based on the distance driven by the vehicle. However, given the scale of wind turbine components, the difficulty of determining service intervals, and the remote locations of wind farms, this maintenance strategy proves unsuitable for wind turbine applications [16].

Condition-based maintenance (CBM) is a strategy that only repairs or replaces damaged parts, reducing the overall wind turbine maintenance costs [17]. Unlike traditional corrective or scheduled maintenance approaches, CBM is based on the actual condition of the equipment. Various sensors located throughout the wind turbine are monitored to assess the condition of the wind turbine components. For wind turbine applications, the CBM strategy is deemed the most appropriate for enhancing availability and reducing operation and maintenance costs [18, 16, 13].

Figure 1.4 shows how the cost of the operating, maintenance, and total of these three strategies

varies with the number of failures[15]. Maintenance costs represent expenses to prevent failures, while operating costs denote expenditures associated with repairing failures. Figure 1.4 shows that the corrective maintenance strategy leads to the highest operating cost due to failure repair being the main expense. On the other hand, the preventive maintenance approach minimizes operating costs, yet it typically entails the highest maintenance costs. The CBM strategy achieves an optimum between maintenance and operating costs.

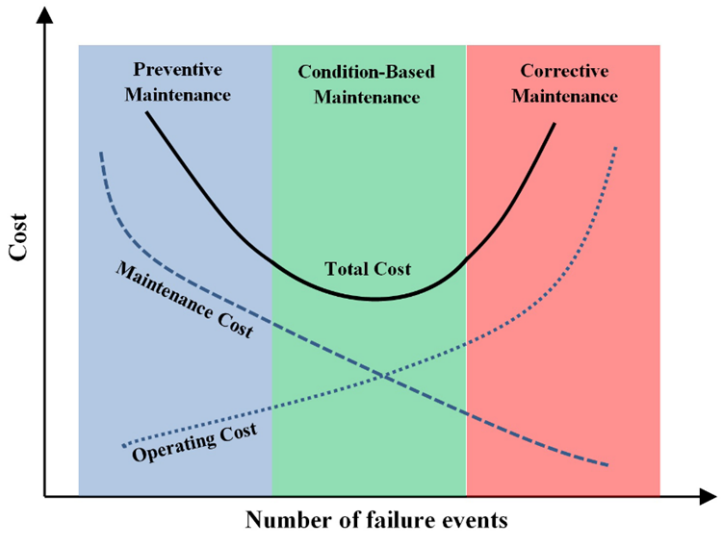

Figure 1.4: The schematic diagram for operating, maintenance, and total costs [15]

1.4. Condition monitoring

To effectively perform CBM, continuous condition monitoring of wind turbine components is essential. Condition monitoring can be divided into two main steps: fault detection and diagnosis and lifetime prognosis [17]. Fault detection involves monitoring the state of a component to detect any indications of faults or potential issues, while diagnosis identifies the nature of the fault and the precise location. Early fault detection prevents wind turbine component failures, thus minimizing operational downtime. Lifetime prognosis predicts the system's remaining useful life (RUL), which is the time period between the current time and the end of the useful life of the asset [19]. The lifetime prognosis step enables maintenance planning, reducing logistics and spare parts provision costs.

1.4.1. Data used for condition monitoring

Condition monitoring methods can be grouped into methods using signals from condition monitoring systems (CMS) or a standard supervisory control and data acquisition (SCADA) system. CMS allows monitoring of various signals such as vibration, strain, torque, temperature, oil debris quality, and acoustic emission. The typical sampling rate for CMS is 20kHz, enabling the effective capture of high-frequency dynamics [20]. One of the main applications of CMS-based condition monitoring methods is analyzing vibrations of the rotating components such as bearings [21]. Methods employ various spectral analysis techniques, such as the Fourier transform, to monitor vibrations of the component in the time and frequency domain. While CMS systems were purpose-built for condition monitoring, they come with drawbacks, such as high costs and the need for extensive resources and expertise to perform analysis [22].

On the other hand, wind turbines are also equipped with a SCADA system. This system is primarily used for performance monitoring of the wind turbine. SCADA signals can be grouped into environmental conditions, electrical, control, and temperature properties. The specific measurements available from a SCADA system vary depending on the supplier. An example of the typical SCADA signals is shown in Table 1.1. SCADA system typically samples data at a rate of 1 Hz, averages signal within 10-minute intervals, and records mean, minimum, maximum, and standard deviation (STD), effectively reducing the amount of transmitted data [17]. However, the limited measurements and low sampling frequency constrain

the fault diagnosis capabilities of SCADA-based condition monitoring methods [22] (Table 1.1). Despite these limitations, many studies focus on utilizing SCADA data for condition monitoring of the different wind turbine components due to its cost-effectiveness and high reliability [23]. Moreover, SCADA-based condition monitoring methods can be widely implemented due to the widespread adoption of performance monitoring systems. Given the factors mentioned above, this thesis focuses on the condition monitoring methods employing SCADA data.

Table 1.1: Typical SCADA Signals for Wind Turbines, adapted from [17]

Environmental Conditions	**Electrical Properties**	**Control Properties**
Ambient temperature	Active power output	Pitch angles of each blade
Wind direction	Reactive power	Yaw angle
Wind speed	Power factor	Rotor speed (low-speed shaft)
	Generator currents	Generator speed (high-speed shaft)
	Generator voltages	Control set points/values
	Transmission-line frequency	Status messages/warnings and operational status code
		Number of starts and stops
	Temperature Properties	
Nacelle temperature	High voltage transformer temperatures	Gearbox bearing temperatures
Hub temperature	Inverter temperatures	Gearbox oil temperature
Generator stator temperatures	Top (turbine) controller temperature	Hydraulic oil temperature
Generator bearing temperatures	Hub (pitch) controller temperature	Converter cooling water temperature
Generator slip ring temperature	Converter controller temperature	Converter choke coil temperature
Main shaft bearing temperature		Grid busbar temperature

1.4.2. Fault detection and diagnosis

Fault detection methods using SCADA data can be divided into three main groups: trending, clustering, and normal behavior modeling (NBM). Trending methods are among the earliest methods developed for wind turbine fault detection. These methods involve the health assessment of turbines through the analysis of a monitored turbine's performance, either by comparing it to the mean performance of other turbines within the wind farm or by monitoring changes in the turbine's performance over time [24, 25, 26]. Trending methods are simple to implement and do not require faulty operation data [17]. However, a key limitation of these methods is their high case-specificity, requiring manual interpretation of results [27].

Researchers have then adopted clustering algorithms to label normal and faulty operations. Clustering algorithms are methods for dividing a set of observations into groups, called clusters so that members of the same group are more alike than members of different groups [28]. The primary drawback of clustering methods is the need for extensive historical fault data for effective training. Furthermore, according to Tautz et al. [27], clustering methods do not offer a notable advantage over trending methods, as interpreting clustering results remains challenging.

NBM methods model the fault-free operation behavior of a system that is expected under the observed operating and environmental conditions. The difference between the model output and measured value, referred to as residual, is analyzed for fault detection [29]. The underlying detection principle relies on deteriorating component health, causing the model relationship to change, thus causing a change in residuals [30]. An extensive amount of data that captures the full range of healthy operations is required to build a representative NBM. Moreover, a robust threshold selection method is essential to perform fault

detection. The main advantage of the NBM methods is that historical failure data and knowledge of the failure type are not necessary for constructing these models [17].

Wind turbine SCADA-based NBM condition monitoring methods mainly focus on data-driven techniques like machine learning and deep learning to build healthy state models and have been widely studied for condition monitoring. Such techniques enable modeling non-linear dynamics and capture complex relationships in the data [31]. However, data-driven NBM methods rely on the black-box nature of AI algorithms, making interpreting results challenging [27]. On the other hand, physics-based NBM methods describe the relationship between the input and output model parameters using equations based on the physics of the component, such as its energy balance. Physics-based NBM offers high interpretability and a deeper understanding of the system's behavior [30, 32, 33]. Unlike data-driven NBM methods, physics-based methods have not been studied extensively. Given the above-mentioned factors, this thesis focuses on the physics-based NBM methods.

1.4.3. Lifetime prognosis

Lifetime prognosis methods can be broadly categorized into two main types: physics-based and data-driven methods [22]. Physics-based methods rely on equations and data to quantitatively describe the growth of the trend of a particular failure mode. These methods are capable of providing highly accurate results and are easy to interpret. However, the complexity of a system and the diversity and uncertainty of its operating conditions make building physical models capturing the degradation difficult [34]. On the other hand, data-driven methods use information from condition monitoring to predict degradation behavior. Data-driven lifetime prognosis methods are widely utilized, as they do not require a deep understanding of the failure type [35].

One of the approaches for performing lifetime prognosis is to introduce health indicators (HIs) to describe the degradation trends [36, 37]. The value of the HI reflects the health condition of a specific system, which is affected by degradation, failures, or operating conditions. After identifying the degradation trend of a component, various methods can be applied to the HI to obtain the RUL [38, 17, 22]. It is essential for the monitored HI to accurately capture the health deterioration of the component. Monitored HI is expected to be monotonic due to the irreversible nature of the degradation process [39]. Additionally, dispersion and seasonal fluctuations of the HI can reduce its accuracy in representing the degradation trend of the component, consequently reducing the reliability of RUL predictions [40, 1].

1.5. Main bearing

A wind turbine can experience a wide range of faults and failures throughout its lifetime. The severity of different faults and failures in wind turbines is shown in Figure 1.5. Less severe faults, such as sensor faults, are not detrimental to wind turbines. However, they can lead to failures in other subsystems, such as control, and affect the turbine's ability to produce power. In contrast, the most severe faults can cause a complete shutdown of the turbine. Figure 1.5 lists the failure of the main shaft bearing among the most severe.

The main shaft bearing, also known as the main bearing, is an essential component that connects the rotor to the drivetrain and transfers torque further down to the generator. It is a large and complex component subjected to significant loads and stresses [41]. Failure of the main bearing causes a turbine shutdown and requires an expensive repair campaign.

Less Severe	Severe	Most Severe
1. Control malfunction due to faults in: • Generator/Rotor speed sensor • Pitch sensor	1. Shaft misalignment 2. Rotor blade misalignment 3. Cracks in rotor blades	1. Rotor blade/hub catastrophic failure 2. Main shaft and coupling failure 3. Main-shaft bearing failure
• Generator power sensor • Wind speed/direction sensor • Measurement cables/connections 2. Hydraulic system fault 3. Mechanical brake fault	4. Ice/Debris built-up on rotor blades 5. Hub spinning on shaft 6. Blade pitch system fault 7. Power converter fault 8. Yaw system fault 9. Power cable twist	4. Gearbox failure 5. Shaft-gearbox coupling failure 6. Generator failure 7. Electrical system failure 8. Premature brake activation 9. Metrological system failure 10. Tower/Foundation failure

Figure 1.5: Major faults and component failures in wind turbines, adopted from [17]

Figure 1.6 shows the frequency and cost of replacing different wind turbine bearings. Even though the main bearing does not fail very often, its failure is among the most expensive to repair [42]. Replacement of a failed main bearing requires the disassembly of the whole nacelle [43]. Moreover, a special vessel for transporting and lifting is required for offshore wind turbine repair. According to Dalgic et al. [12], the cost of lifting operations using a vessel accounts for more than 50% of the total O&M costs. Furthermore, although the main bearing has been identified as one of the most crucial challenges in wind turbine reliability, this component has not received as much attention as other drivetrain components [44]. For these reasons, this thesis focuses on the wind turbine main bearing.

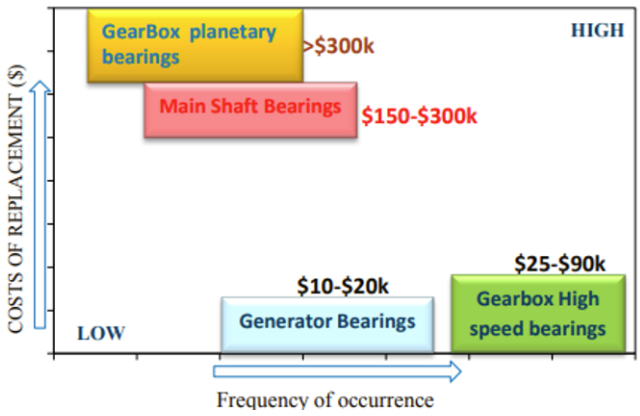

Figure 1.6: Replacement cost of critical wind turbine bearings [42]

1.6. Research motivation

The wind turbine main bearing is one of the major drivetrain components. The high cost of repairing the wind turbine main bearing underscores the importance of minimizing O&M expenses associated with this component [44]. Moreover, in comparison to other drivetrain components, the wind turbine main bearing has received relatively less attention.

Varying loads and different drivetrain issues lead to premature wear of the main bearing. Progressive wear, in turn, leads to an increase in the main bearing temperature [43]. Various condition monitoring methods analyze the temperature changes of the main bearing. Employing an effective condition monitoring method allows the detection of potential failure and planning of maintenance, thus reducing O&M costs.

Physics-based NBM has been successfully employed for fault detection of the main bearing [32, 30]. However, the application of these methods for degradation trend monitoring has not received attention, and this is the objective of this thesis, which can be formulated as follows.

Research Objective

Develop a physics-based NBM employing SCADA data for monitoring the degradation trend of the wind turbine main bearing.

The proposed approach builds on the physics-based NBM available in the literature [32] to extend its application for degradation trend monitoring. It aims to increase the monotonicity and reduce the dispersion of the developed HI using physics-based NBM. To achieve these aims, the proposed method considers the variability of wind field characteristics and takes into account seasonal variations in operating conditions. The variability of wind field characteristics causes significant changes in the loads experienced by the wind turbine components. This has a significant effect on the long-term health of the component. However, current approaches do not consider varying wind field characteristics in their NBM of the main bearing temperature. Additionally, seasonal fluctuations present in the residuals have been noted as one of the limitations of the available method [32].

The thesis sub-questions are defined as follows.

1. How can physics-based NBM be used for the degradation trend monitoring of the wind turbine main bearing?
2. How can the current physics-based NBM's limitations be effectively overcome when using SCADA data?
3. What metrics should be utilized to evaluate the effectiveness of the proposed method?
4. How can seasonal variations be taken into account when developing a physics-based NBM for the degradation trend monitoring of the wind turbine main bearing? And what are the benefits?
5. How can variability of wind field characteristics be taken into account when developing physics-based NBM for the degradation trend monitoring of the wind turbine main bearing? And what are the benefits?

The rest of the report is structured as follows. Chapter 2 provides a literature review and addresses the gap that this thesis aims to fill in. Chapter 3 presents the theoretical background, where terms and metrics related to this thesis project are introduced. Chapter 4 presents a detailed description of the methodology proposed in this thesis. Chapter 5 describes the performed case studies and presents the results. Chapter 6 concludes this research and discusses future work.

2

Literature review

This chapter provides an overview of the literature explored in this thesis. Section 2.1 focuses on the wind turbine main bearing and presents its most common failure modes. Section 2.2 discusses SCADA-based condition monitoring methods of the component. Section 2.3 delves into NBMs used for condition monitoring of the main bearing and presents data-driven (Section 2.3.1) and physics-based (Section 2.3.2) methods. Section 2.4 highlights the gap that this thesis aims to fill in.

2.1. Main bearing as a component

The primary purpose of the main bearing is to support the rotor while effectively handling non-torque loads and preventing the transmission of loads further down the drivetrain [44]. Depending on the configuration, this function can be performed independently or in collaboration with the gearbox and mounts. The selection of a specific type and configuration for wind turbine main bearings depends on various factors, including drivetrain type, expected loading conditions, and economic considerations.

Figure 2.1 illustrates the most common configuration for geared drivetrain wind turbines, referred to as the 'three-point mount', while Figure 2.2 shows a single-main bearing configuration for direct-drive wind turbines [45]. Irrespective of the configuration type, the main bearing consists of four elements: an inner race, an outer race, rolling elements, and a cage around rolling elements, as shown in Figure 2.3.

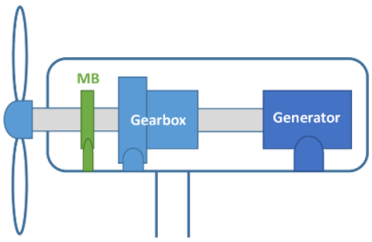

Figure 2.1: Geared drive train wind turbine main bearing (MB) configuration [44]

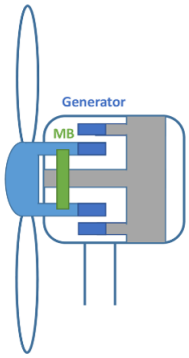

Figure 2.2: Direct drive train wind turbine MB configuration [44]

The main bearing directly interacts with the rotor and the other rotating components located further down the drivetrain. Incident loads are transmitted from the wind turbine rotor to the hub and then passed through the cantilevered low-speed shaft to the main bearing. Various studies investigate the effects of loads on this drivetrain component [46, 45, 47, 41]. Guo et al. [45] use an analytic model to describe the loads experienced by the main bearing and to study its axial displacement. Cardoun et al. [48] focus on the effects of loads experienced by the main bearing due to constant yaw misalignment. Notably, Hart et al. [49] perform a study focusing on the effect of wind field characteristics on the wind turbine main bearing

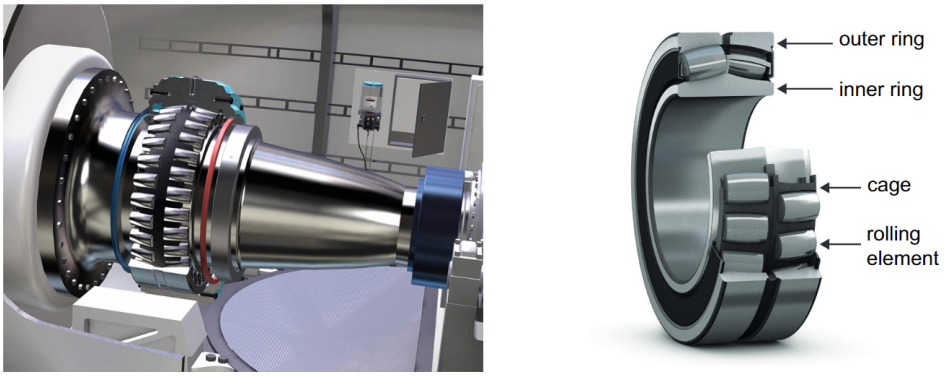

Figure 2.3: Spherical roller bearing [1]

loading. They emphasize the importance of considering this variability during the design phase. The study analyzes loads experienced by the main bearing using the DNV-GL BLADED multi-body simulation tool and considers different wind speed and turbulence intensity (TI) conditions as well as different power law shear exponents. TI represents the intensity of wind velocity fluctuation, while the wind shear exponent is a parameter that represents a change in the vertical wind profile shape. Notably, the stronger TI leads to higher loads experienced by the main bearing. This study demonstrates high variability in the main bearing loads due to variations in wind field characteristics. Additionally, the authors point out the potential of considering wind field variability to enable more reliable maintenance approaches.

While wind turbine main bearings are designed to operate over a 20-years, the rate of failures can be as high as 30%, with some bearings failing in less than six years of operation. Misalignments and high axial-to-radial load ratios experienced by the main bearing during operation contribute to wear mechanisms, ultimately leading to damage and failure [50, 49]. The most prominent types of damage and wear mechanisms experienced by the main bearings are [44]:

- Classical fatigue happens due to the dynamic contact conditions from machine operation generating stress fields and plastic deformation in the contacting materials. Over time, these conditions can lead to fatigue cracks or inclusions within the material structure. When these cracks intersect, pits are created, releasing abrasive particles into the bearing environment. Once this process is initiated, it can self-propagate through the surface, roughening and reducing the contact areas.
- Micro-pitting occurs when the lubricant film thickness in a specific area is inadequate due to excessive loading or operating conditions that deviate from the design parameters. In such cases, the lubrication is not sufficient to fully separate the contacting surfaces of the roller and the race. Consequently, interactions occur between their rough surfaces, leading to the formation of surface asperities.
- Spalling is a type of damage that occurs when material peels or flakes away from the surface of a bearing. It is commonly triggered by various forms of damage or stress, including misalignment, excessive loading, localized stresses from surface dents, or hard particles in the lubricant. Additionally, micro-pitting can serve as a precursor to spalling on the affected surface.
- Smearing is a type of wear that occurs when two surfaces slide against each other, causing material from one surface to transfer onto the other. This commonly occurs in rolling element bearings when there are rapid changes in roller rotational speeds, such as when a roller accelerates as it enters an operating region with higher loads.
- Abrasive wear is a type of damage caused by the intrusion of hard particles into the bearing contacts, resulting in physical damage such as indentations left by rolling particles or surface scratches caused by sliding particles.
- Fretting corrosion is characterized by the development of pits, grooves, and corrosion products in the surrounding areas. The main bearing experiences low-amplitude structural vibration, leading to fretting. Fretting corrosion can be caused by various factors, including moisture content, acid rain, corrosive gases, and lubricant acidification.

2.2. Main bearing condition monitoring

Numerous studies explore the condition monitoring of the wind turbine main bearing to increase the lifespan and reduce its O&M costs. SCADA-based condition monitoring methods focus mainly on temperature analysis, where abnormal temperature increase indicates the degradation of the main bearing. Various methods using SCADA data for main bearing condition monitoring have been proposed in the literature.

Astolfi et al. [25] investigate the trending of temperatures for various components against rated power across different time scales. The application of this method to the main bearing temperature is proven effective in detecting failure that leads to low-speed shaft replacement. The main bearing temperature of the malfunctioning turbine displays a significant increase two weeks prior to the warning generated by the SCADA system, in contrast to the temperatures in other main bearings within the same wind farm. Wilkinson et al. [30] are also able to detect the main bearing damage, comparing the temperature normalized to the wind farm average. However, the authors ultimately dismiss the trending method, citing its low accuracy and reliability.

While various methods have been explored for SCADA-based condition monitoring of wind turbine main bearings, the literature predominantly focuses on NBM approaches. Figure 2.4 provides an overview of the common NBM condition monitoring method. The SCADA data set is divided into historical data for training and real-time data for condition monitoring. First, the preprocessing step is applied to historical data. Next, various techniques, such as regression, machine learning, or deep learning, are employed to obtain the NBM of the component [31]. From a design perspective, the NBM can be established using either the Full Signal Reconstruction (FSRC) concept, which utilizes signals other than the target parameter to predict the target, or AutoRegressive with eXogenous (ARX) input modeling, which incorporates past values of the target as well [29]. Once the NBM model is established, it is deployed to predict expected normal behavior using real-time data (test data). It is important to note that the same preprocessing steps applied to the historical set are also applied to real-time data. Finally, the difference between predicted and observed behavior, referred to as residuals or prediction errors, is analyzed.

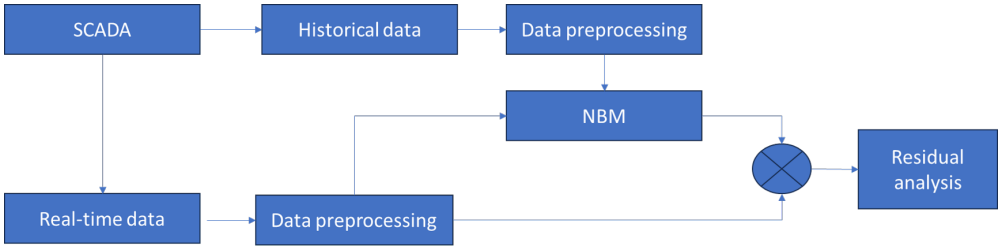

Figure 2.4: Schematic overview of NBM condition monitoring framework using SCADA data, adopted from [51]

The scope of NBM condition monitoring methods can be fault detection and lifetime prognosis. Fault detection involves setting thresholds and performing fault detection when the thresholds are passed. Various frameworks are available in the literature to perform fault detection. They differ based on the type of smoothing used, threshold selection, and the number of instance thresholds passed to perform detection. Exponentially Weighted Moving Average (EWMA) control chart is one of the most common frameworks used for fault detection [32, 52, 29]. It can be divided into two steps: selecting the smoothing factor for residuals and establishing a threshold. Thresholds and smoothing factors are chosen to reduce the number of false alarms while not compromising the sensitivity to detecting actual failures.

Lifetime prognosis using NBMs involves estimating the expected time to NBM residuals reach a given threshold, which is called the predicted RUL of the component. The lifetime prognosis of wind turbine components has received less attention than the fault detection in the literature [53]. Upon reviewing the current state-of-the-art research, it is clear that the primary focus of SCADA-based condition monitoring methods lies in the estimation of RUL of wind turbine generators [54, 55, 56]. Moreover, NBM approaches have not been widely used in the context of lifetime prognosis.

2.3. Wind turbine main bearing condition monitoring using SCADA-based NBM

SCADA-based NBM approaches can be divided into two categories: data-driven and physics-based methods. Section 2.3.1 summarises studies that propose data-driven NBM methods, while Section 2.3.2 delves into studies employing physics-based NBM methods for condition monitoring of the main bearing.

2.3.1. Data-driven NBM

Most of the current research on NBMs relies on purely data-driven methods [31, 57], which are capable of capturing nonlinear relationships among the monitored signals. However, the main disadvantages of these methods are the high computational cost and the black-box nature of the results. Different approaches using various data-driven methods are presented in this section.

Butler et al. [58] propose a Bayesian approach to model the temperature of the main bearing. Inputs to the ARX-type model are:

- Main bearing temperature, at previous timestamp (mean)
- Main shaft rotation speed (mean)
- Hydraulic brake temperature (mean)
- Hydraulic brake pressure (mean)
- Blade pitch position (mean)

This specific set of input parameters is chosen after multiple trials of various combinations of variables. The main bearing temperature is linearly corrected with ambient temperature to remove the effect of ambient conditions from the sensor readings. Residuals corresponding to the low-load operation are selected, and a low-pass filter for smoothing is applied. The main shaft rotational speed between 0.1 and 2 rotations per minute (RPM) is considered a low-load operational range of the wind turbine main bearing. Residuals corresponding to the low-load operational range are analyzed due to their monotonicity and consistency. The RUL of the component is obtained using a bearing degradation model from literature, whose coefficients are obtained using the particle filter approach. The method yields a strong indication of potential failure with a lead time of 30 days. However, degradation model parameters are fine-tuned based on historical failure data to perform the RUL prediction. Due to the limitation of having only two turbines with failures, the paper lacks extensive validation of the approach.

Zhang et al. [59] model the main bearing temperature using an artificial neural network (ANN). Inputs to the ARX-type model are:

- Main bearing temperature, at previous timestamp (mean)
- Main shaft rotation speed (mean)
- Nacelle temperature (mean)
- Power produced (mean)

The authors select these parameters based on physical relevance and prior research on gearbox bearings. The model achieves a Root Mean Square Error (RMSE) of 0.2, which is acceptable for fault detection. Notably, the authors demonstrate that the ANN model for the main bearing, which is trained on SCADA data from one turbine, can be applied for fault detection in other turbines within the same wind farm. The method provides fault detection three months before failure.

Herp et al. [60] also use an ANN model to model the temperature of the main bearing. However, the authors explore the lifetime prognosis aspect of condition monitoring. Inputs to the FSRC-type model are:

- Active power (mean)
- Generator speed (mean)
- Gearbox oil temperature (mean)
- Ambient temperature (mean)
- Nacelle temperature (mean)

Obtained residuals are sampled on an hourly basis. The authors apply the Bayesian inference, which is a stochastic approach, to obtain the RUL of the component. The approach predicts the main bearing failure within a 33-day period.

Wang et al. [61] propose a method that combines clustering and NBM. The method initially applies the K-Means algorithm to SCADA data, dividing it into two clusters. It is important to note that compared to other available data-driven NBM approaches, Wang et al. incorporate two models to consider the variable operating conditions of the wind turbine. Variables are chosen based on correlation coefficients with the main bearing temperature. The inputs for the first cluster model are:

- Hub temperature (mean)
- Generator front bearing temperature (mean)
- Gearbox rear bearing temperature (mean)
- Nacelle temperature (mean)
- Ambient temperature (mean)
- Gearbox inlet oil temperature (mean)
- Gearbox oil temperature (mean)
- Converter ambient temperature (mean)
- Generator rear bearing temperature (mean)

For the second cluster, two additional inputs of blade motor temperatures are used due to the high correlation with the main bearing temperature. The Optimized Deep Belief Network (ODBN) is selected to build the NBM of the main bearing temperature. Additionally, the authors applied the Mahalanobis Distance as a measure of deviation between modeled and measured values. The proposed method is compared with the ODBN framework without clustering. Notably, the proposed method does not significantly improve advanced fault detection. Both frameworks detect failure approximately three and a half days in advance. Furthermore, including the clustering step in the framework increases its computational intensity. However, the method does not have false detections, unlike the ODBN framework without clustering.

Tutiven et al. [52] employ a one-class Support Vector Machine (SVM) classifier for fault detection of the wind turbine main bearing. One-class SVM methods are trained on healthy data to build an NBM. Subsequently, when monitored data (test data) deviates from the learned healthy state, it is labeled as faulty. It is important to note that the one-class SVM methods do not require faulty data for training. Inputs to the FSRC-type model proposed by Tutiven et al. are:

- Main shaft temperature (mean)
- Wind speed (mean)

The authors select the main shaft temperature as it is the variable most closely associated with the examined failure. Notably, the ambient temperature is subtracted from the main shaft temperature to avoid seasonality. Wind speed is chosen as a parameter related to the operation state of the wind turbine. For performing fault detection, outliers given by the SVM classifier are counted weekly, and EWMA smoothing is applied to a weekly number of faults to reduce the number of false detections. The proposed method detects the main bearing failure three months in advance. Additionally, the method detects failures in the wind blades and the gearbox. Blade failure is detected two days before, while gearbox failure is detected a month prior to the actual failures. The authors attribute the detections of blade and gearbox failures to their impact on the operation of the analyzed component, consequently leading to abnormal operation of the main bearing.

Zhang et al. [62] explore deep learning methods to model main bearing temperature. The proposed method applies a one-dimensional convolution neural network (Conv1D) to fuse information of features of previous timestamps simultaneously. Conv1d is used to couple the ten previous time-series timestamps of the input variables to form a new time series of input variables to the temperature model. The Long Short-Term Memory network (LSTM) is used to build the NBM. Inputs to the model are selected based on their correlation with the modeled parameter and their relevance to wind turbine operation. Inputs to the ARX-type model are:

- Main bearing temperature (mean)

- Generator rotational speed (mean)
- Power produced (active power grid side) (mean)
- Wind speed (mean)
- Ambient temperature (mean)

Zhang et al. apply a moving average window length of 30 samples (5 hours) to reduce the influence of the accidental factors on the residuals. The proposed method detects abnormal behavior in the bearing three months before failure. Notably, the study also demonstrates that the proposed prediction model is more accurate in predicting the main bearing temperature than traditional machine learning methods such as XGBoost Regression, Random Forest Regression, and LSTM algorithms.

2.3.2. Physics-based NBM

The physics-based NBMs available in the literature use mainly equations based on heat transfer to describe the relationship between parameters. A physics-based model is usually fitted to historical SCADA data to obtain its parameters, which are then used in a test set to model the target value. Using SCADA data for physics NBM allows to overcome the main limitation of pure physics-based models, which require case-specific knowledge, such as size and material properties, to build the model. Furthermore, the broad availability of SCADA systems enables the widespread application of physics-based NBM methods.

Wilkinson et al. [30] propose a model relying on the energy balance of the components to obtain their temperature. The authors develop higher-order polynomial models to obtain various component temperatures. Model parameters are determined based on healthy state operation. The study showcases the models' effectiveness in detecting 24 major component failures, including the main bearing failure. For the main bearing, the input signals to the FSRC-type model are:

- Main shaft rotational speed (mean)
- Nacelle temperature (mean)
- Power produced (mean)

Wilkinson et al. apply a rolling average window to smooth the obtained residuals. The proposed method detects failure seven months in advance. However, the authors emphasize the importance of carefully determining appropriate parameters and thresholds to ensure the method's reliability and accuracy.

Cambron et al. [32] apply a physics-based model relying on the energy balance of the wind turbine main bearing. Least squares regression fit is applied to the SCADA data to obtain main bearing temperature model coefficients. Inputs to the ARX-type model are:

- Main bearing temperature, at previous timestamp (mean)
- Main shaft rotational speed (mean)
- Nacelle temperature (mean)
- Power produced (mean)

The obtained residuals are averaged daily, and the EWMA control chart is applied for fault detection. The authors conduct two case studies. The proposed method is able to detect the main bearing fault three and ten weeks before SCADA generates a warning. This approach demonstrates significant potential in generating warnings for failure detection. The authors also point out clear seasonal variations present in the residuals, which can potentially lead to false detections.

2.4. Discussion

A lack of research employing NBM approaches for lifetime prognosis becomes apparent when reviewing the SCADA-based condition monitoring methods proposed in the literature. Moreover, existing studies that use NBM for the lifetime prognosis of the main bearing adopt purely data-driven modeling methods. These methods use NBM residuals as a HI to obtain the RUL of the component. To achieve reliable RUL predictions, the monitored HI should accurately capture the degradation trend of the component.

Physics-based NBM methods offer high interpretability and a deeper understanding of the system's behavior, in contrast to the ”black-box” nature of the purely data-driven methods. Moreover, utilizing

SCADA data to build physics-based NBM does not require specification parameters, making this approach widely applicable. However, physics-based NBM using SCADA data for the main bearing has not received as much attention as data-driven approaches [35, 57, 63]. It is essential to highlight that the paper by Cambron et al. [32] represents the most recent available work on physics-based NBM modeling of the main bearing. The study points out the seasonal fluctuations present in the residuals as one of the limitations of the proposed method. Furthermore, available SCADA-based methods do not consider the variability of wind field characteristics in the NBM of the main bearing temperature. The loads experienced by this component are significantly impacted by varying operating conditions [44], and this can have a significant impact on the bearing lifetime. Notably, wind fields with stronger TI contribute to the higher loads experienced by the main bearing [49]. This thesis proposes an approach that considers seasonal fluctuations and the variability of wind field characteristics in physics-based NBM employing SCADA data to build HI for accurate degradation trend monitoring of the wind turbine main bearing.

3

Theoretical Background

This chapter provides the theoretical background for the methods and metrics used in this research. Section 3.1 presents multivariate linear regression as this is applied to obtain the coefficients of the physics-based NBM proposed in this work. Section 3.2 introduces the Monte Carlo method, which is used to predict the main bearing temperature. Section 3.3 delves into statistical metrics employed to assess the performance of the proposed approach.

3.1. Multivariate linear regression

Multivariate linear regression is a statistical method used to analyze the relationship between two or more independent variables and a dependent variable [64]. The model is expressed as:

$$\begin{aligned} y_i &= \beta_0 + \beta_1 x_{i1} + \beta_2 x_{i2} + \cdots + \beta_k x_{ik} + \epsilon_i \\ &= \beta_0 + \sum_{j=1}^{k} \beta_j x_{ij} + \epsilon_i \quad i = 1, 2, \ldots, n \end{aligned} \tag{3.1}$$

Where y_i is the dependent variable, $x_{i,j}$ are the independent variables, β_0 is the intercept, $\beta_1, \beta_2, ...\beta_k$ are the coefficients that represent the impact of each independent variable on the dependent variable, and ϵ is the error term. The least squares method is used to obtain equation coefficients. The least squares function is shown as:

$$L = \sum_{i=1}^{n} \epsilon_i^2 = \sum_{i=1}^{n} \left(y_i - \beta_0 - \sum_{j=1}^{k} \beta_j x_{ij} \right)^2 \tag{3.2}$$

The least squares function minimizes the sum of the squared errors between estimated and actual values, L [64]. To estimate independent variable coefficients, L should be minimized with respect to $\beta_0, \beta_1, \cdots \beta_k$. Where least square estimates $\hat{\beta}_0, \hat{\beta}_1, \cdots \hat{\beta}_k$ must satisfy

$$\left. \frac{\partial L}{\partial \boldsymbol{\beta}_0} \right|_{\hat{\boldsymbol{\beta}}_0, \hat{\boldsymbol{\beta}}_1, \ldots, \hat{\boldsymbol{\beta}}_k} = -2 \sum_{i=1}^{n} \left(y_i - \hat{\boldsymbol{\beta}}_0 - \sum_{j=1}^{k} \hat{\boldsymbol{\beta}}_j x_{ij} \right) = 0 \tag{3.3}$$

and

$$\left. \frac{\partial L}{\partial \beta_j} \right|_{\hat{\boldsymbol{\beta}}_0, \hat{\boldsymbol{\beta}}_1, \ldots, \hat{\boldsymbol{\beta}}_k} = -2 \sum_{i=1}^{n} \left(y_i - \hat{\boldsymbol{\beta}}_0 - \sum_{j=1}^{k} \hat{\boldsymbol{\beta}}_j x_{ij} \right) x_{ij} = 0 \quad j = 1, 2, \ldots, k \tag{3.4}$$

Equation (3.3) is simplified as shown below:

$$\begin{aligned}
\left.\frac{\partial L}{\partial \boldsymbol{\beta}_0}\right|_{\hat{\boldsymbol{\beta}}_0,\hat{\boldsymbol{\beta}}_1,\ldots,\hat{\boldsymbol{\beta}}_k} &= -2\sum_{i=1}^{n}\left(y_i-\hat{\boldsymbol{\beta}}_0-\sum_{j=1}^{k}\hat{\boldsymbol{\beta}}_j x_{ij}\right)=0\\
\sum_{i=1}^{n}\left(\hat{\beta}_0+\sum_{j=1}^{k}\hat{\beta}_j x_{ij}-y_i\right)&=0\\
n\hat{\beta}_0+\sum_{i=1}^{n}\sum_{j=1}^{k}\hat{\beta}_j x_{ij}-\sum_{i=1}^{n}y_i&=0\\
n\hat{\beta}_0+\sum_{j=1}^{k}\left(\sum_{i=1}^{n}\hat{\beta}_j x_{ij}\right)&=\sum_{i=1}^{n}y_i\\
\hat{\beta}_0+\frac{1}{n}\sum_{j=1}^{k}\left(\sum_{i=1}^{n}\hat{\beta}_j x_{ij}\right)&=\frac{1}{n}\sum_{i=1}^{n}y_i\\
\hat{\beta}_0+\frac{1}{n}\sum_{i=1}^{n}\hat{\beta}_1 x_{i1}+\frac{1}{n}\sum_{i=1}^{n}\hat{\beta}_2 x_{i2}+\cdots+\frac{1}{n}\sum_{i=1}^{n}\hat{\beta}_k x_{ik}&=\frac{1}{n}\sum_{i=1}^{n}y_i
\end{aligned} \tag{3.5}$$

Equation (3.4) is simplified the same way:

$$\begin{aligned}
\left.\frac{\partial L}{\partial \beta_j}\right|_{\hat{\boldsymbol{\beta}}_0,\hat{\boldsymbol{\beta}}_1,\ldots,\hat{\boldsymbol{\beta}}_k} &= -2\sum_{i=1}^{n}\left(y_i-\hat{\boldsymbol{\beta}}_0-\sum_{j=1}^{k}\hat{\boldsymbol{\beta}}_j x_{ij}\right)x_{ij}=0 \quad j=1,2,\ldots,k\\
&\sum_{i=1}^{n}(\hat{\boldsymbol{\beta}}_0+\sum_{j=1}^{k}\hat{\boldsymbol{\beta}}_j x_{ij}-y_i)x_{ij}=0\\
&\sum_{i=1}^{n}x_{ij}\hat{\boldsymbol{\beta}}_0+\sum_{i=1}^{n}x_{ij}\sum_{j=1}^{k}\hat{\boldsymbol{\beta}}_j x_{ij}-\sum_{i=1}^{n}x_{ij}y_i=0\\
&\sum_{i=1}^{n}x_{ij}\hat{\boldsymbol{\beta}}_0+\sum_{i=1}^{n}x_{ij}\sum_{j=1}^{k}\hat{\boldsymbol{\beta}}_j x_{ij}=\sum_{i=1}^{n}x_{ij}y_i\\
&\hat{\boldsymbol{\beta}}_0\sum_{i=1}^{n}x_{ij}+\sum_{i=1}^{n}x_{ij}\sum_{j=1}^{k}\hat{\boldsymbol{\beta}}_j x_{ij}=\sum_{i=1}^{n}x_{ij}y_i \Rightarrow\\
&\hat{\beta}_0\sum_{i=1}^{n}x_{i1}+\hat{\beta}_1\sum_{i=1}^{n}x_{i1}^2+\hat{\beta}_2\sum_{i=1}^{n}x_{i1}x_{i2}+\cdots+\hat{\beta}_k\sum_{i=1}^{n}x_{i1}x_{ik}=\sum_{i=1}^{n}x_{i1}y_i\\
&\ldots\ldots\ldots\ldots\ldots\ldots\ldots\ldots\ldots\ldots\ldots\ldots\ldots\ldots\ldots\ldots\ldots\ldots\ldots\ldots\\
&\hat{\beta}_0\sum_{i=1}^{n}x_{ik}+\hat{\beta}_1\sum_{i=1}^{n}x_{ik}x_{i1}+\hat{\beta}_2\sum_{i=1}^{n}x_{ik}x_{i2}+\cdots+\hat{\beta}_k\sum_{i=1}^{n}x_{ik}^2=\sum_{i=1}^{n}x_{ik}y_i
\end{aligned} \tag{3.6}$$

The obtained least squares equations are shown in Equation (3.7). Note that the number of equations and the number of coefficients is the same. A system of linear equations is solved to obtain the least squares estimators of the regression coefficients,$\hat{\beta_0}, \hat{\beta_1}, \cdots \hat{\beta_k}$. Once the coefficients are obtained, Equation (3.1) can be used to model the target variable y_i. This thesis utilizes the ”LinearRegression” function from

the Python ”sklearn.linear_model” library to perform linear regression.

$$\begin{aligned}
&n\hat{\beta}_0 + \hat{\beta}_1 \sum_{i=1}^{n} x_{i1} + \hat{\beta}_2 \sum_{i=1}^{n} x_{i2} + \cdots + \hat{\beta}_k \sum_{i=1}^{n} x_{ik} = \sum_{i=1}^{n} y_i \\
&\hat{\beta}_0 \sum_{i=1}^{n} x_{i1} + \hat{\beta}_1 \sum_{i=1}^{n} x_{i1}^2 + \hat{\beta}_2 \sum_{i=1}^{n} x_{i1}x_{i2} + \cdots + \hat{\beta}_k \sum_{i=1}^{n} x_{i1}x_{ik} = \sum_{i=1}^{n} x_{i1}y_i \\
&\cdots\cdots\cdots\cdots\cdots\cdots\cdots\cdots\cdots\cdots\cdots\cdots\cdots\cdots\cdots\cdots\cdots\cdots\cdots\cdots\cdots\cdots\cdots\cdots\cdots\cdots \\
&\hat{\beta}_0 \sum_{i=1}^{n} x_{ik} + \hat{\beta}_1 \sum_{i=1}^{n} x_{ik}x_{i1} + \hat{\beta}_2 \sum_{i=1}^{n} x_{ik}x_{i2} + \cdots + \hat{\beta}_k \sum_{i=1}^{n} x_{ik}^2 = \sum_{i=1}^{n} x_{ik}y_i
\end{aligned} \tag{3.7}$$

3.2. Monte Carlo method

The Monte Carlo method is a common name given to methods that find solutions to deterministic problems by performing stochastic simulations. Unlike conventional forecasting models that rely on known input values, the Monte Carlo method uses probability distributions of input variables to generate random samples and perform simulations. This process allows for a comprehensive evaluation of various possible scenarios, providing valuable insights into the potential outcomes under uncertain conditions.

The principle of the Monte Carlo method relies on the Law of Large Numbers [65]. If $X_1, X_2, \ldots X_n$ are independent and identically distributed random variables with a common distribution f, and $g : E \to \mathbb{R}$, where g is a function with finite expectation E. The law of large numbers states that as the sample size n approaches infinity, the mean of $g(X_i)$ converges to the true expected value $E(g(X))$:

$$\lim_{n\to\infty} \frac{1}{n} \sum_{i=1}^{\infty} g\left(X_i\right) = E(g(X)) \tag{3.8}$$

Monte Carlo simulations can be used to obtain the probability density function of the variable $E(g(X))$ by iteratively generating random numbers X_i and calculating the corresponding values of $E(g(X_i))$. The Monte Carlo method finds application in sales projections, pricing, etc., enabling the assessment of potential risks [66, 67]. Although frameworks can differ based on the application case, the typical procedure for conducting a Monte Carlo simulation can be described as [68]:

1. **Construct the Model:** Establish the model that describes the system.
2. **Select Simulation Variables:** Identify the variables within the model that exhibit uncertainty and choose a suitable probability distribution for variables.
3. **Generate Iterative Simulations:** Perform iterative simulations by generating random samples. Typically, a common practice is to conduct 1000 iterations.
4. **Aggregate and Analyze Results:** Calculate statistical measures such as the mean, standard deviation, and variance of the simulated results.

3.3. Statistical metrics

This thesis utilizes various metrics to perform a comparative analysis of the HIs and assess the performance of NBM. Section 3.3.1 introduces the Mann-Kendall monotonicity metric. Section 3.3.2 presents various error-quantifying metrics used for assessing the performance of the NBM. Section 3.3.3 introduces the empirical mode decomposition, which can be used to quantify noise in monitored time series.

3.3.1. Mann-Kendall monotonicity test

The Mann-Kendall test, also known as the MK test, is a method used to quantify the monotonicity of the time series [69]. MK test is a non-parametric method and can be applied to data with various distributions without relying on the assumption of normality. This thesis utilizes the MK τ metric to quantify monotonicity in monitored time series. The MK τ metric ranges from -1 to 1, with negative values indicating decreasing monotonicity and positive values indicating increasing monotonicity, while values close to zero show no

significant trend in time series [69]. The method applied to calculate the τ metric is shown in Equation (3.9) [70, 71].

$$S = \sum_{i=1}^{n-1} \sum_{j=i+1}^{n} \text{sgn}(x_j - x_i) \tag{3.9}$$

Where the x_j are the sequential data of the analyzed time series. A score of +1 is assigned if x_i < x_j, a score of -1 is assigned if x_i > x_j, and a score of 0 is assigned if x_i = x_j, as shown in Equation (3.10).

$$\text{sgn}(x_j - x_i) = \begin{cases} 1 & \text{if } \theta > 0 \\ 0 & \text{if } \theta = 0 \\ -1 & \text{if } \theta < 0 \end{cases} \tag{3.10}$$

The statistic S is obtained by summing the products of the scores for a data set and linearly related τ. The value of τ is obtained as $\tau = \frac{S}{D}$, where D is the maximum possible value of S for a given n. When there are no tied values, $D = \frac{n(n-1)}{2}$. The presence of ties decreases D, thereby increasing τ for a given value of S.

It should be noted that other metrics quantifying the monotonicity of the time series are also available in literature [39, 72, 73]. Notably, one of the widely used monotonicity metrics is Mo obtained as shown in Equation (3.11).

$$Mo = \frac{1}{N} \sum_{i=1}^{N} \left(\frac{n_i^+}{n_i - 1} - \frac{n_i^-}{n_i - 1}\right), i = 1, \cdots, N \tag{3.11}$$

Where n_i^+ and n_i^- are the number of positive and negative first derivatives of the times series curve, and n_i is the total number of observations. Compared to the MK τ metric, the Mo metric calculates monotonicity based solely on the difference in values of consecutive points and fails to capture the overall trend in time series [74]. To address this limitation of the Mo metric, the trendability metric is also used. Trendability measures the cross-correlation of monitored time series with time and is calculated as [39]:

$$Trend = \frac{\left| n \left(\sum_{i=1}^{n} x_i t_i\right) - \left(\sum_{i=1}^{n} x_i\right) \left(\sum_{i=1}^{n} t_i\right) \right|}{\sqrt{n \sum_{i=1}^{n} x_i^2 - \left(\sum_{i=1}^{n} x_i\right)^2} \sqrt{n \sum_{i=1}^{n} t_i^2 - \left(\sum_{i=1}^{n} t_i\right)^2}} \tag{3.12}$$

Where x_i represents values of time series, and t_i represents time. Both Mo and $Trend$ are common metrics used to evaluate HIs [39, 72, 73, 75, 37]. However, due to the Mo metric limitations in capturing the overall trend in time series, this thesis utilizes the MK τ metric to perform a comparison of the analyzed approaches.

3.3.2. Error measurements

To perform condition monitoring, it is essential that NBM accurately captures the healthy operation of the component. NBM performance metrics aim to quantify the overall difference between predicted and actual measurements. The higher the difference between predicted and actual measurements, the less accurate the model is. The common model performance metrics are [76, 77, 62, 61]:

- The Mean Absolute Error (MAE) quantifies the average absolute difference between the predicted and actual values of the target variable. The formula for calculating MAE is:

$$MAE = \frac{1}{N} * \sum_{i=1}^{N} |y_{true}(i) - y_{pred}(i)| \tag{3.13}$$

  Where N is the number of samples in the dataset, y_{pred} is the predicted value of the target variable, and y_{true} is the actual value of the target variable.

- Mean Squared Error (MSE) measures the mean of the squared difference between predicted and actual value. MSE is sensitive to outliers due to the square term in the error. The formula for calculating MSE is:

$$MSE = \frac{1}{N} * \sum_{i=1}^{N} (y_{true}(i) - y_{pred}(i))^2 \tag{3.14}$$

- The Root Mean Squared Error (RMSE) is another statistical measure that evaluates the errors made by a predictive model [76]. It is computed as the square root of the average of the squared differences between the predicted and actual values of the target variable. The formula for calculating RMSE is:

$$RMSE = \sqrt{\frac{1}{N} * \sum_{i=1}^{N} (y_{true}(i) - y_{pred}(i))^2} \tag{3.15}$$

- R-squared, also called the coefficient of determination, is a statistical metric utilized to assess the quality of fit of a linear regression model. It quantifies the fraction of the target variable's variance that the model's independent variables can account for [76]. The R-squared values fall between 0 and 1, with higher values signifying a better fit of the model to the data. The formula for calculating R-squared is:

$$R^2 = 1 - \frac{SS_{res}}{SS_{tot}} \tag{3.16}$$

  Where SS_{res} is the sum of the squared differences between the predicted and actual values, and SS_{tot} is the sum of the squared differences between the actual values and the mean of the target variable.

- Mean Absolute Percentage Error (MAPE) measures deviation in relation to the magnitude of the actual value. The formula for calculating MAPE is:

$$MAPE = \frac{1}{N} * \sum_{i=1}^{N} \frac{|y_{true}(i) - y_{pred}(i)|}{y_{true}(i)} * 100\% \tag{3.17}$$

3.3.3. Noise quantification using Empirical Mode Decomposition

Empirical Mode Decomposition (EMD) is a data-driven and unsupervised method used for decomposing signals [78]. The method is based on the assumption that any non-stationary and non-linear time series can be broken down into simple intrinsic oscillation modes. The EMD algorithm is designed to analyze signal oscillations at the localized level and divides the data into distinct, non-overlapping components based on time scales referred to as Intrinsic Mode Functions (IMFs). IMFs adhere to two fundamental properties:

- An IMF has just a single extremum between two consecutive zero crossings.
- An IMF has a mean value of zero.

The process of performing EMD entails an iterative decomposition of a provided signal $x(t)$ into its IMFs, denoted as $c_i(t)$, along with a residual component $r(t)$. This decomposition process is achieved through a procedure known as sifting. EMD algorithm can be described as follows [79, 80, 81].

1. Local maximum values of input signal X(t) are found and connected using cubic spline to obtain upper envelope reference. The same procedure is repeated for local minimum values, and a lower envelope is obtained. Figure 3.1 shows the obtained upper and lower envelope.

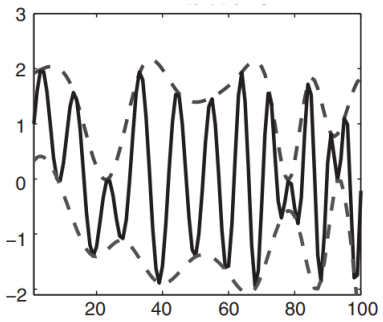

Figure 3.1: Upper envelope and lower envelope [81]

2. Average of upper and lower envelopes are calculated to get the mean envelope.

$$m1 = \frac{X^{1,1}_{max}(t) + X^{1,1}_{min}(t)}{2} \tag{3.18}$$

3. The residue component is calculated as the difference between the original signal and the mean envelope.

$$h_{1,1} = X(t) - m_{1,1} \tag{3.19}$$

4. The original signal X(t) is replaced with $h_{1,1}$, and Steps 1-3 are repeated until the standard deviation from two consecutive sifting is less than the predefined threshold ϵ. Which is typically set between 0.2 and 0.3.

$$\text{SD} = \sum_{t=0}^{T} \left[\frac{\left| \left(h_{1,(k-1)}(t) - h_{1,k}(t) \right) \right|^2}{h^2_{1,(k-1)}(t)} \right] < \epsilon \tag{3.20}$$

Consequently, the first IMF component is decomposed and denoted as:

$$c_1 = h_{1,k} = m_{1,k} - h_{1,k-1} \tag{3.21}$$

5. Previous steps are repeated until the final residual has no more oscillations and can not be decomposed further. The obtained residual indicates the mean trend of the signal. After applying the EMD, the input signal is expressed as the summation of a finite number of IMFs (c_i) and the residual $r_n(t)$, as shown in Equation (3.22).

$$X(t) = \sum_{i=1}^{n} c_i(t) + r_n(t) \tag{3.22}$$

EMD applications

EMD has found its application in various fields [82]. In the context of degradation analysis, EMD is applied to identify degradation trends in systems, such as lithium-ion batteries [83, 84, 85]. Figure 3.2 shows the IMFs of Time-Varying Filter-based EMD (TVF-EMD) to analyze the decreasing trend of original capacity in a lithium-ion battery [83].

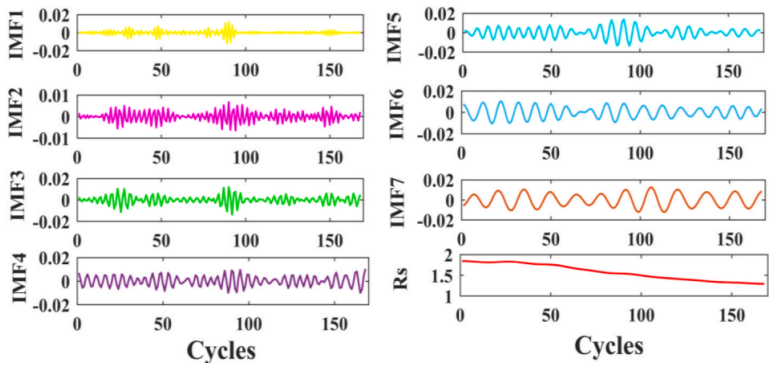

Figure 3.2: The decomposed series of original capacity in the battery using TVF-EMD [83]

Within wind turbine condition monitoring frameworks, EMD is applied for the signal processing of bearing vibrations [21, 86]. Vibration signals are decomposed using EMD, and the Hilbert transform is applied to each IMF to enable analysis in the frequency domain. Obtained spectrum is used to monitor characteristic bearing frequencies to identify defects in the component.

Researchers also employ EMD to quantify and filter noise in various signals [87, 88, 86]. Karaganis et al. [89] apply EMD to decompose the electrocardiogram and calculate the energy density of the obtained IMFs. An electrocardiogram is a heartbeat time series signal commonly used in healthcare to evaluate the heart. Based on the energy density value, the authors perform a statistical significance test to identify

IMFs with high-level noise. Where energy density is calculated as:

$$E_n = \frac{1}{N}\sum_{j=1}^{N}[c_n(j)]^2 \tag{3.23}$$

Where c_n is the nth IMF of EMD decomposition, and N is the length of the IMF.

CEEMDAN

Researchers have developed different types of EMD methods. In this thesis, Complete Ensemble EMD with Adaptive Noise (CEEMDAN) is employed specifically for its applications in cases where signals exhibit seasonal changes [90, 91]. The key difference between CEEMDAN and simple EMD lies in the incorporation of adaptive white noise. The benefit of CEEMDAN is its ability to address the problem of noise residue and efficiently diminish the occurrence of low-frequency components characterized by small amplitudes. Figure 3.3 illustrates the CEEMDAN flowchart. The explanation of the CEEMDAN algorithm is presented below [90]:

1. White noise $\omega^i(t)$ is added to the initial signal sequence $x(t)$.

$$x^i(t) = x(t) + \omega^i(t) \tag{3.24}$$

   The modified signal sequence ($x^i(t)$) is decomposed using EMD to obtain the first IMF.

$$IMF_1^i = E(x^i(t)) \tag{3.25}$$

2. Step 1 is repeated ”I” times so that the first IMF of CEEMDAN is calculated as:

$$IMF_1(t) = \frac{1}{I}\sum_{i=1}^{I} IMF_1^i(t) \tag{3.26}$$

3. kth residue for k=1, .., K, is calculated as:

$$r_k(t) = r_{k-1}(t) - IMF_k(t), \quad r_0(t) = x(t) \tag{3.27}$$

4. White noise is added to the obtained residue:

$$r_k^i(t) = r_k(t) + \omega^i(t) \tag{3.28}$$

   The modified residue (r_k^i) is decomposed using EMD to obtain IMF_k^i.

$$IMF_k^i = E(r_k^i(t)) \tag{3.29}$$

5. Step 4 is repeated ”I” times so that the (k)th CEEMDAN IMF is defined as:

$$IMF_k(t) = \frac{1}{I}\sum_{i=1}^{I} IMF_k^i(t) \tag{3.30}$$

6. Steps 3, 4, and 5 are repeated until the obtained residue can not be decomposed further.

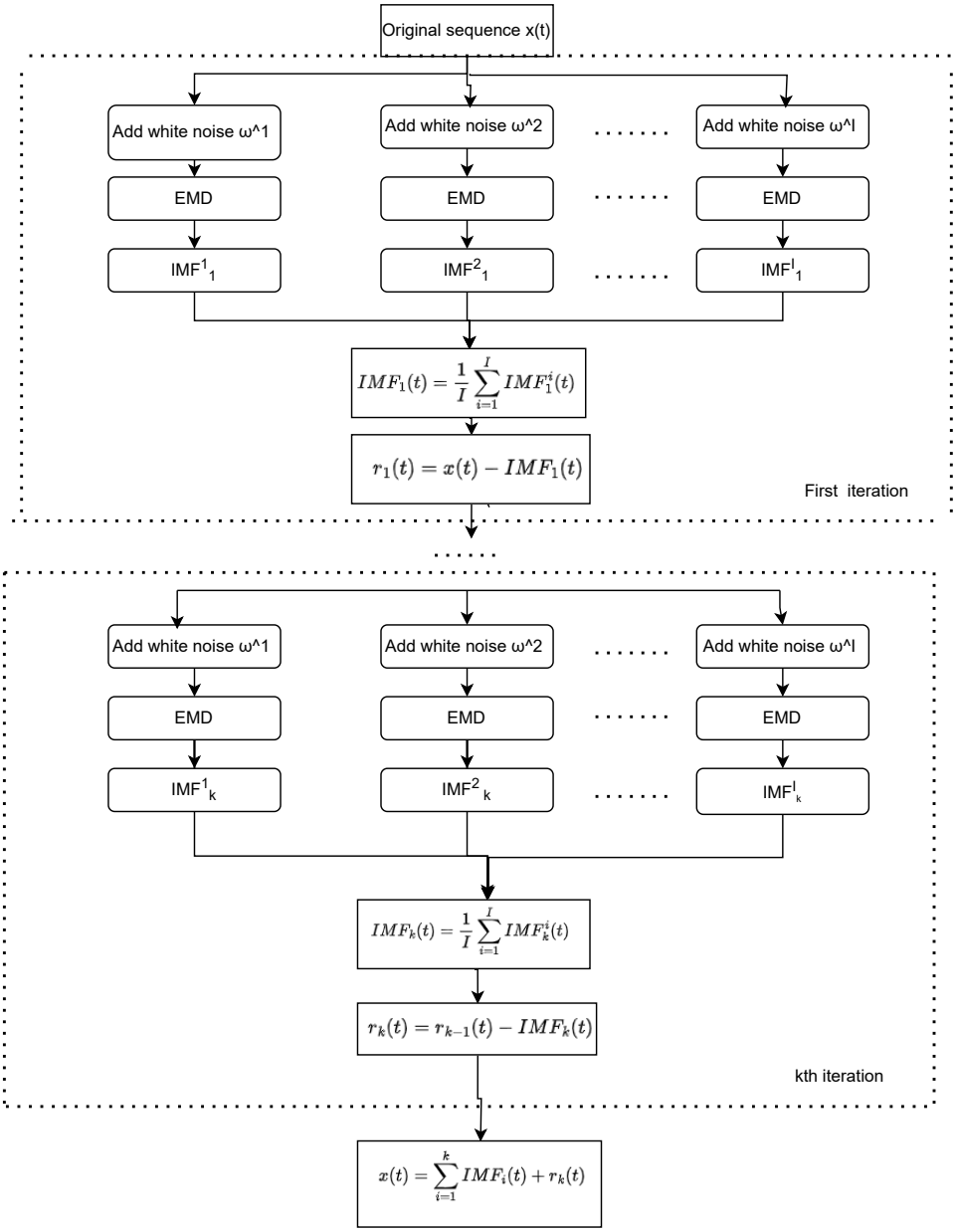

Figure 3.3: CEEMDAN flowchart, adopted from [90]

4

Methodology

This chapter describes the methodology proposed in this thesis for developing a physics-based NBM employing SCADA data to build an HI for accurate monitoring of the degradation trend of wind turbine main bearings. Section 4.1 describes the reference study that serves as the foundation for the proposed method. Section 4.2 outlines the improvements to the reference model proposed in this work for enabling more accurate degradation trend monitoring. Section 4.3 describes how these improvements are implemented in the proposed method. Section 4.4 presents an overview of the method proposed.

4.1. Baseline reference paper

The study by Cambron et al. [32], presented in Section 2.3.2, is the foundation for the proposed approach. The authors adopted a model based on the heat balance of the main bearing component, which, assuming that the main bearing is a closed system, can be described by the following equation [92] :

$$\Delta U = P_{in} - P_{out} \tag{4.1}$$

where the difference between mechanical power input (P_{in}) and power output (P_{out}) to the main bearing corresponds to an increase in its internal energy (ΔU). The authors used Equation (4.2) to represent the change in the main bearing temperature.

$$C_p \frac{dT_{\text{bear}}}{dt} \simeq R^{-1} \left(T_{\text{bear}} - T_{\text{nacelle}}\right) + \mu\omega^2 + \alpha P \tag{4.2}$$

Where T_{bear} is the main bearing temperature [K], $T_{nacelle}$ is the nacelle temperature [K], ω is the main shaft rotational speed [rad/s],P is the electric power generated [W], C_p is the main bearing heat capacity [Ws/K], R is the system thermal resistance [K/W], μ is the friction coefficient in main bearing [Ws^2/rad^2], α is the coefficient of heating performance [K/W]. The first term on the right-hand side of Equation (4.2) refers to the thermal conductivity and represents the heat transfer between the main bearing and the nacelle. The second term of the equation represents the heat generated by the rotational friction. The last term takes into account the Joule effect in the generator. The Joule effect is heat created in the generator due to electric losses of the component. Equation (4.2) can be written in the recursive form and simplified as:

$$\begin{aligned}
C_p \frac{\Delta T_{\text{bear}}}{\Delta t} &= R^{-1}(T_{\text{bear}}(t) - T_{\text{nacelle}}(t)) + \mu\omega^2(t) + \alpha P(t) \\
C_p \frac{T_{\text{bear}}(t) - T_{\text{bear}}(t-1)}{\Delta t} &= R^{-1}(T_{\text{bear}}(t) - T_{\text{nacelle}}(t)) + \mu\omega^2(t) + \alpha P(t) \\
T_{\text{bear}}(t)\frac{C_p}{\Delta t} - T_{\text{bear}}(t-1)\frac{C_p}{\Delta t} &= R^{-1}(T_{\text{bear}}(t) - T_{\text{nacelle}}(t)) + \mu\omega^2(t) + \alpha P(t) \\
T_{\text{bear}}(t)\frac{C_p}{\Delta t} - R^{-1}T_{\text{bear}}(t) &= T_{\text{bear}}(t-1)\frac{C_p}{\Delta t} - R^{-1}T_{\text{nacelle}}(t) + \mu\omega^2(t) + \alpha P(t) \\
T_{\text{bear}}(t)(\frac{C_p}{\Delta t} - R^{-1}) &= T_{\text{bear}}(t-1)\frac{C_p}{\Delta t} - R^{-1}T_{\text{nacelle}}(t) + \mu\omega^2(t) + \alpha P(t) \\
T_{\text{bear}}(t) &= \frac{T_{\text{bear}}(t-1)\frac{C_p}{\Delta t}}{\frac{C_p}{\Delta t} - R^{-1}} + \frac{R^{-1}T_{\text{nacelle}}(t)}{R^{-1} - \frac{C_p}{\Delta t}} + \frac{\mu\omega^2(t)}{\frac{C_p}{\Delta t} - R^{-1}} + \frac{\alpha P(t)}{\frac{C_p}{\Delta t} - R^{-1}} \\
T_{\text{bear}}(t) &= \beta_1 T_{\text{bear}}(t-1) + \beta_2 T_{\text{nacelle}}(t) + \beta_3\omega^2(t) + \beta_4 P(t)
\end{aligned} \tag{4.3}$$

To model the main bearing temperature, Cambron et al. used Equation (4.4).

$$\hat{T}_{\text{bear}}(t) \approx \beta_1 T_{\text{bear}}(t-1) + \beta_2 T_{\text{nacelle}}(t) + \beta_3 \omega^2(t) + \beta_4 P(t) \tag{4.4}$$

Where the coefficients β_1, β_2, β_3, β_4 are estimated using multivariate linear regression described in Section 3.1 by fitting Equation (4.4) to a 1 year of operational SCADA data. The model is then applied to a test set to predict the main bearing temperature. The temperature residual ($Res(t)$) is then defined as the difference between the recorded SCADA mean temperature ($T_{\text{mes}}(t)$) and the modeled temperature ($\hat{T}_{\text{bear}}(t)$).

$$Res(t) = T_{\text{mes}}(t) - \hat{T}_{\text{bear}}(t) \tag{4.5}$$

The obtained residuals are averaged daily, and an EWMA control chart is applied to perform fault detection in the main bearing. The authors use the calculated temperature residual as a main bearing HI and consider the increase in the residual above a defined threshold as an indication of failure. Figure 4.1 summarises the methodology applied by [32].

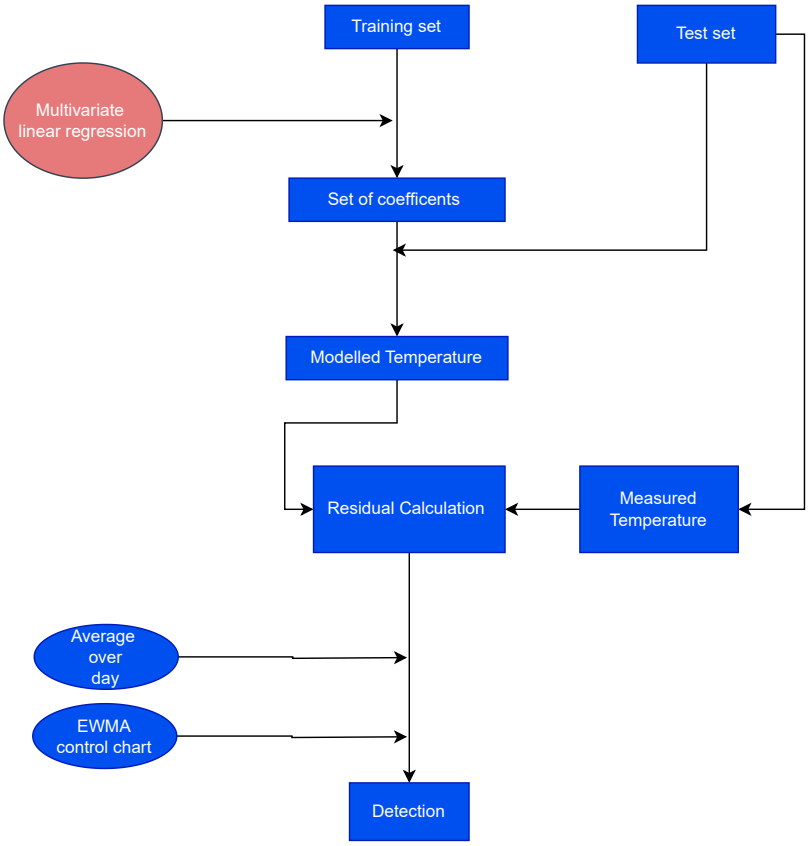

Figure 4.1: Methodology proposed in the baseline work [32]

4.2. Aims of the proposed approach

The proposed approach uses as a basis the NBM developed by [32] and aims at improving its performance for the estimation of the main bearing temperature residuals to obtain a more reliable and accurate indicator of the degradation trend. Lifetime prognosis inherently entails uncertainties as it involves projecting the progression of damage into the future [38]. Constructing HI that accurately captures the degradation trend establishes a solid foundation for subsequent RUL predictions [40]. The proposed approach aims to improve the monotonicity and dispersion of the monitored HI to enable accurate degradation trend monitoring. To achieve these improvements, the proposed method considers seasonality and variability of wind field characteristics.

This section presents the aims of the proposed approach and is structured as follows. Section 4.2.1 highlights the significance of the HI monotonicity, while Section 4.2.2 underscores the importance of the HI dispersion. To address these challenges, Section 4.2.3 discusses the significance of reducing seasonal fluctuations in the HI, while Section 4.2.4 points out the importance of considering the variability of wind field characteristics when applying physics-based NBM.

4.2.1. Monotonicity

The main bearing degradation trend is expected to be monotonic, according to the irreversible nature of the degradation processes [40]. A primary metric for assessing the performance of different HIs is, in fact, monotonicity [39, 93, 72]. The monotonic behavior of the HI facilitates forecasting the progression of the degradation to perform RUL predictions. The proposed approach aims to obtain monotonic HI to enable accurate degradation trend monitoring. In this study, the MK τ metric, described in Section 3.3.1, is used to quantify the monotonicity of the analyzed HI.

4.2.2. Dispersion

Dispersion measures the amount of variability exhibited by data [76, 64]. Stochastic processes, sensor errors, and varying operating conditions introduce fluctuations in HI [94]. Both Figures 4.2 and 4.3 show monotonic HIs. However, those in Figure 4.3 show higher fluctuations due to dispersion. Fluctuating and dispersed HIs behavior reduce the accuracy of fitted degradation models, hindering the precise projection of degradation trends into the future. This, in turn, leads to less accurate RUL predictions [94, 95, 96]. Moreover, dispersion is a particularly relevant issue in the case of temperature-based NBM as high fluctuations in residuals can lead to false detections [57, 53]. Therefore, the proposed approach aims to reduce the dispersion of the HI to enable accurate degradation trend monitoring.

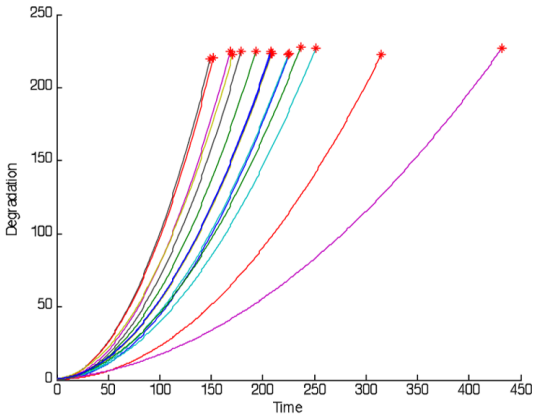

Figure 4.2: An example of monotonic HIs [75]

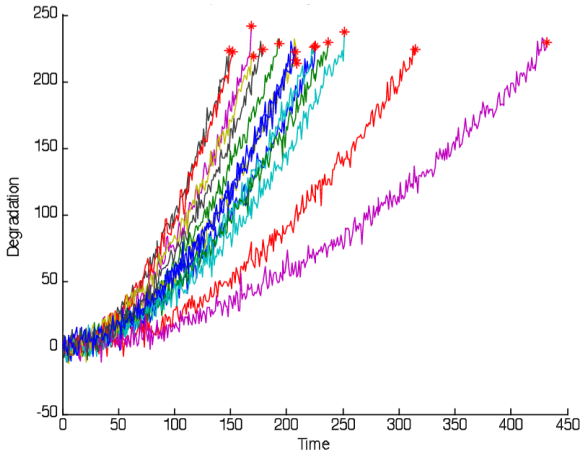

Figure 4.3: An example of monotonic and dispersed HIs [75]

For degradation monitoring, dispersion refers to the extent to which data points deviate from a reference line. A degradation time series with a monotonic irreversible increasing trend is adopted as a reference line. A simple linear fit is applied to the monitored HI to obtain the reference degradation line. Deviation from this fitted reference line is considered as the dispersion of the HI. Figure 4.4 shows an example of a HI time series and their reference degradation trend, given by the green line. The HI dispersion is given by the distance between the HI values and the reference degradation line. To quantify the dispersion of HI, the MSE metric introduced in Section 3.3.2 is used.

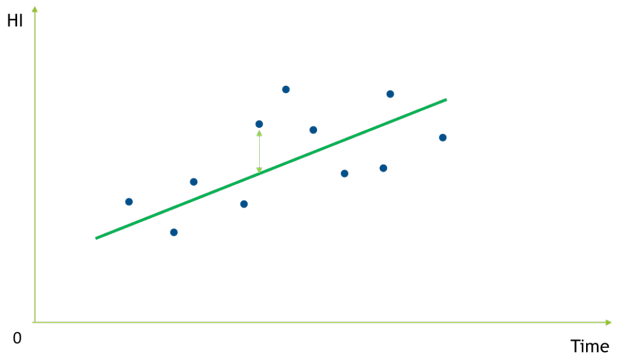

Figure 4.4: Dispersion calculation method with respect to reference degradation line

However, a limitation of this approach is the assumption of the underlying linear trend. Various studies employ different degradation models, such as double exponential, exponential, and linear models [58, 97, 98, 99]. The choice of an appropriate model capturing the degradation process is essential to evaluate the dispersion of the HI, which makes this approach case-specific. To address this limitation, an alternative data-driven dispersion quantification metric based on the measure of the HI noise is proposed in this thesis.

This work adopts CEEMDAN, described in Section 3.3.3.2, to quantify dispersion based on the measure of the HI noise. The underlying concept is that a HI with a more consistent and less dispersed pattern is expected to demonstrate a lower level of noise. The adopted method can be described as follows. CEEMDAN is applied to the monitored HI. Subsequently, the residual trend obtained from CEEMDAN is used as the reference degradation trend, while all the IMFs are considered noise. To quantify the noise level in the monitored HI, the signal power of each IMF is calculated using [100, 89]:

$$\text{Power}_{IMF_l} = \frac{1}{N}\sum_{i=0}^{N-1}|x_i|^2 \tag{4.6}$$

where $Power_{IMF_l}$ represents the power of each IMF signal, IMF_l, N is the number of samples in the IMF signal, and x_i denotes the individual samples of the IMF signal. The power values of the IMFs are then averaged to obtain the overall noise level of HI:

$$\text{Noise} = \frac{1}{k}\sum_{l=1}^{k} Power_{IMF_l} \tag{4.7}$$

where k represents the number of IMFs obtained as a result of CEEMDAN decomposition. Figure 4.5 shows an example of the time series decomposed IMFs using CEEMDAN [84]. The figure illustrates the battery capacity time series during 170 cycles decomposed into five IMFs.

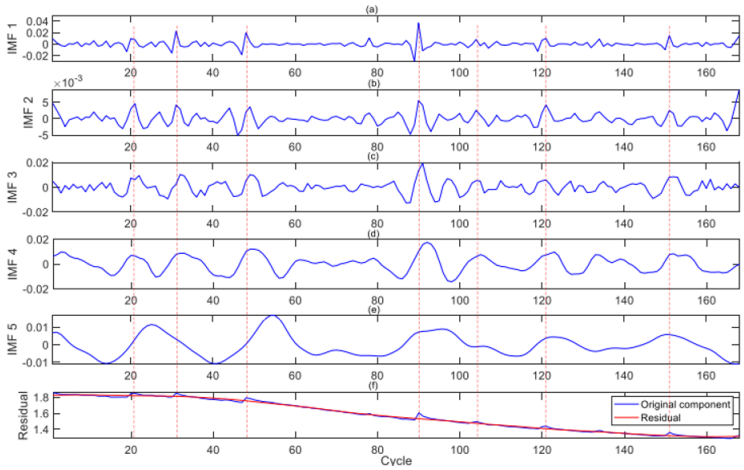

Figure 4.5: CEEMDAN decomposed time series [84]

According to the proposed approach, the noise of the time series is then obtained by calculating the average power of the five IMFs:

$$\text{Noise} = \frac{1}{k}\sum_{l=1}^{k} Power_{IMF_i} = \frac{1}{k}\sum_{l=1}^{k}\frac{1}{N}\sum_{i=0}^{N-1}|x_{i,l}|^2 = \frac{1}{5}\sum_{l=1}^{5}\frac{1}{170}\sum_{i=0}^{169}|x_{i,l}|^2 \tag{4.8}$$

Karaganis et al. [89] use noise quantification in their study, focusing on the heartbeat time series signal known as an electrocardiogram (Section 3.3.3.1). The authors calculated the power of each of the obtained IMFs to determine its significance for further analysis. However, as this study focuses on degradation trend monitoring, all the signals except the residual trend derived from CEEMDAN decomposition are considered noise.

4.2.3. Seasonality

Seasonal changes in wind turbine operating conditions might lead to corresponding oscillations in the HI trend. These seasonal HI fluctuations could be wrongly interpreted as degradation trends [1, 32]. Moreover, they increase the dispersion and reduce the monotonicity of the monitored degradation trend, which can lead to a less accurate lifetime prognosis [40, 94]. Therefore, the proposed method aims to consider seasonal variations when applying physics-based NBM to enable more accurate degradation trend monitoring. This thesis quantifies seasonality by calculating the cross-correlation between the HI and the ambient temperature using the Pearson correlation coefficient:

$$r = \frac{\sum (x_i - \bar{x})(y_i - \bar{y})}{\sqrt{\sum (x_i - \bar{x})^2 \sum (y_i - \bar{y})^2}} \tag{4.9}$$

where r is the correlation coefficient, x_i are the values of the ambient temperature in a sample, $\bar{x}$ is the mean of the values of the ambient temperature, y_i are the values of the HI in a sample, and $\bar{y}$ is the mean of the values of the HI.

When the NBM is adequately built, seasonality should not be evident in the residuals. Ideally, NBM residuals are expected to consist of noise and trend components. However, the periodic oscillations in the residuals are an indication of seasonality. This emphasizes the importance of considering seasonal variations for establishing adequate physics-based NBM.

4.2.4. Variability of wind field characteristics

The primary reason for the premature failure of wind turbine components is attributed to the variability of the wind conditions [17]. Varying loads experienced by the main bearing significantly impact the lifespan of the component [56, 43]. The main bearing is located between the rotor and the drivetrain, which makes it more susceptible to varying loads than components further down the drivetrain [44].

Various model parameters are used in NBM to capture varying operating conditions of the wind turbine main bearing, as described in Section 2.3. Signals such as wind speed, rotational speed, and power produced either implicitly or explicitly capture the operation of wind turbine components. However, current NBM methods are based solely on the mean value of these signals, which do not consider the variations of operating conditions within the 10-minute averaged time frame commonly applied by the SCADA system. These variations impact monitored HI. This thesis aims to take into account the variability of operating conditions within a 10-minute time to reduce the dispersion and increase the monotonicity of the obtained HI, enabling more accurate degradation trend monitoring.

4.3. Proposed approach

The method proposed in this work builds an HI of the main bearing using its temperature residuals estimated with a physics-based NBM. The proposed approach builds upon the method introduced in Section 4.1 to achieve the aims discussed in Section 4.2. This thesis proposes two main steps to achieve these aims. The first (Step S), described in Section 4.3.1, applies multiple NBMs to mitigate seasonal fluctuations of the HI. The second (Step M), described in Section 4.3.2, employs the Monte Carlo method to take into account the variability of operating conditions within 10-minute intervals and introduces data density within

a threshold region as novel HI for degradation trend monitoring. The proposed method also applies two further steps, averaging over a selected interval and EWMA smoothing described in Section 4.3.3, to increase the signal-to-noise ratio and smooth a main bearing HI.

4.3.1. Step S - Seasonality

Various methods are available to mitigate the seasonal effects observed in the residuals. Butler et al. [58] and Tutiven et al. [52] use relative temperature as input to the NBM models. Encalada et al. [1] emphasize the importance of providing at least one year of training data to ensure the NBM training set captures various operating conditions. Zhang et al. [62] use ambient temperature as input to their model to avoid seasonality effects. Antico et al. [91] use CEEMDAN decomposition to retrieve seasonal trends of the time series.

Wang et al. [61] apply two models to take into account variable operating conditions of the main bearing (Section 2.3.1). NBM models are built for two clusters obtained as a result of the K- Means labeling. It should be noted that wind direction is a partitioning parameter between the two clusters. According to the authors, partitioning is based on wind direction due to the purely data-driven nature of the K-means algorithm. To mitigate the impact of seasonal changes on the residuals, this thesis develops separate physics-based NBMs corresponding to the time period of the year. In the Northern Hemisphere, wind turbines produce more energy during winter due to the stronger available wind field. The proposed solution is based on the significant difference between wind turbine operating conditions during winter and summer months.

The proposed step applies multivariate regression to derive distinct sets of coefficients of Equation (4.4) corresponding to different time periods of the year instead of one set of coefficients applied for the entire period, as done in the reference paper [32]. Figure 4.6 shows the procedure adopted for considering the effects of seasonality.

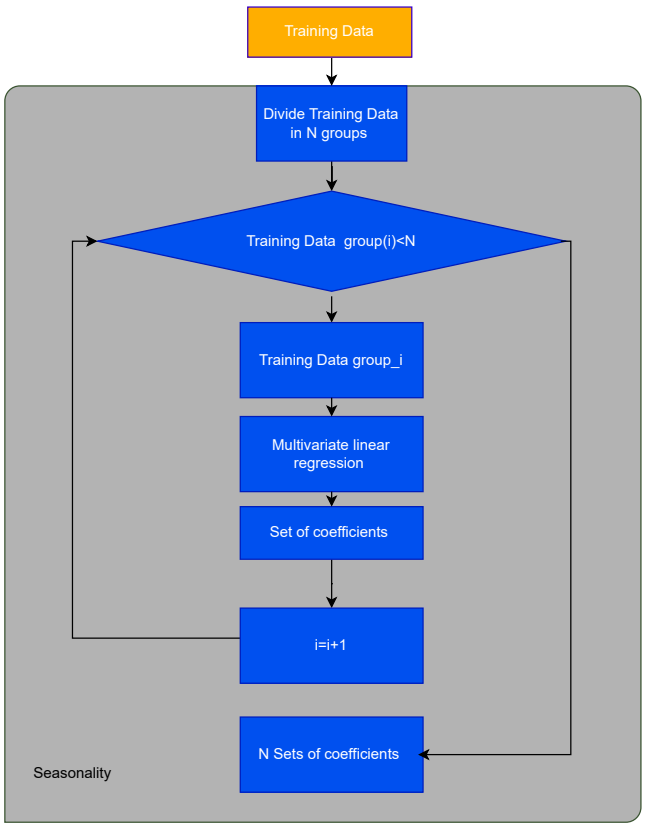

Figure 4.6: Seasonality step (Step S)

Initially, the training data is divided into N distinct groups based on the time of the year. Where the

number of group divisions is tuned based on the effect of decreasing seasonality on the accuracy of the obtained model. Various data group divisions can be applied, such as two groups (colder months, September-February/hotter months, March-August), four groups(Winter/Spring/Summer/Fall seasons), and 12 groups (each month has a corresponding set of coefficients). Subsequently, multivariate linear regression is applied to each specific group within the SCADA training data, and this process is repeated for every group. This yields N sets of coefficients for the reference Equation (4.4).

4.3.2. Step M - Variability of wind field characteristics

To consider variations in wind field characteristics within each 10-minute interval, this thesis uses the STD records from the SCADA data. Ideally, for each of the signals used in the equation and for each timestamp, the SCADA data provide the average, min, max, and STD values. The STD is the metric that shows how the measurements vary within each 10-minute averaged interval. This is directly related to the variable conditions under which the main bearing operates.

To consider the variability in the main bearing operation within each 10-minute time frame, this thesis proposes to apply the Monte Carlo method. The proposed method performs an iterative simulation using random values of the input variables of Equation (4.4) to simulate the distribution of the predicted main bearing temperatures in a 10-minute time frame. These modeled temperatures simulate the variability of the actual bearing temperatures within the averaged interval. The schematic in Figure 4.7 illustrates the procedure proposed for applying the Monte Carlo method.

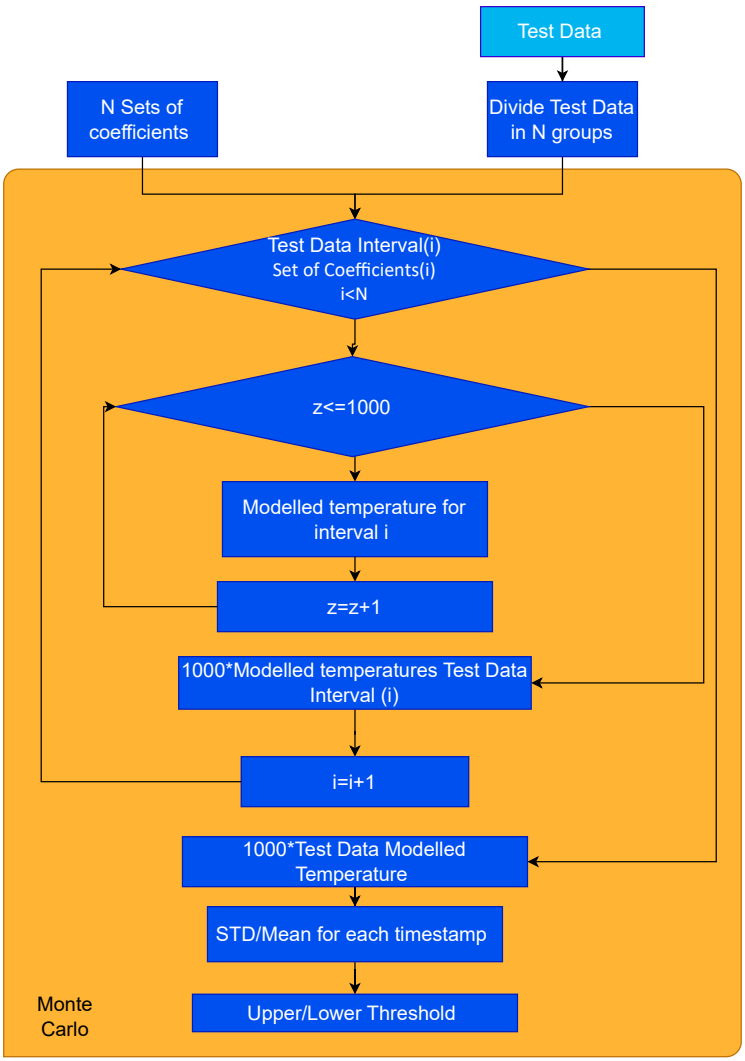

Figure 4.7: Monte Carlo step (Step M)

First, following the previous seasonality step, N data groups and their respective sets of coefficients are identified. For each group in the test data, 1000 random values are generated for each signal in Equation (4.2). The random values are generated based on the mean and STD values obtained from the SCADA records of the test set. This results in 1000 modeled main bearing temperatures for each timestamp. The selection of 1000 iterations is based on its common use as a standard number for Monte Carlo simulations [101]. The process is repeated for every group in the test data, yielding 1000 modeled main bearing temperatures for each timestamp for the entire data set. The mean, $AVG(t)$, and standard deviation, $STD(t)$, of these values are then calculated for each timestamp of the test data. Finally, these metrics are used to calculate the upper,$Up_{threshold}(t)$, and lower, $Low_{threshold}(t)$, thresholds for each timestamp as:

$$Up_{threshold}(t) = AVG(t) + k * STD(t) \tag{4.10}$$

$$Low_{threshold}(t) = AVG(t) - k * STD(t) \tag{4.11}$$

Where k is a tuning parameter that determines the width of the threshold region. The distance between $Low_{threshold}(t)$ and $Up_{threshold}(t)$ is referred to as the threshold region and represents the range of possible main bearing temperatures during each 10-minute time frame. It is recommended to use a failed case study to tune k to enable the highest monotonicity and lowest dispersion of HI while not compromising fault detection. Then, the tuned k parameter is applied to another case study to monitor the degradation trend.

In this study, the value $k = 1$ was chosen to define the range of model results that represent the healthy operation of the wind turbine main bearing. Figure 4.8 shows the probability density function of a normal distribution with its mean, μ, and STD, σ. According to the 3σ rule, 68.2% of the data is located one STD away from μ. In contrast, two and three STD values are used as fault detection thresholds representing the unhealthy behavior of the component [102]. The defined k=1 corresponding 1 STD threshold region is chosen to represent a healthy operating region. Thus, when the measured mean main bearing temperature falls into the modeled threshold region, it is assumed to represent a healthy operation of the component. Monte Carlo simulation's generated $Low_{threshold}(t)$ and $Up_{threshold}(t)$ for each timestamp allows to introduce a new approach for residual calculation, as discussed in the next section.

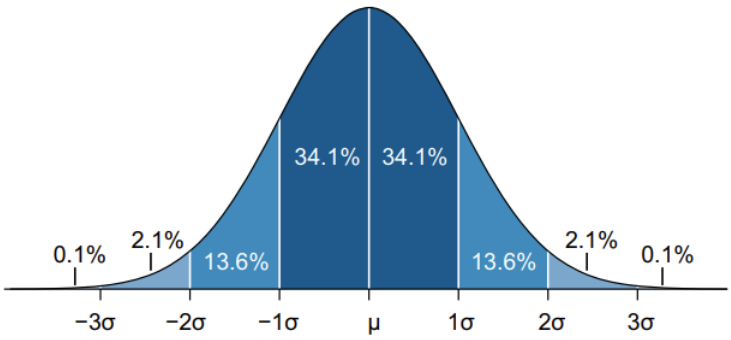

Figure 4.8: Probability density function of normal distribution with mean (μ) and STD (σ) [103]

Residual calculation

The Monte Carlo simulation transforms the punctual main bearing temperature values obtained from Equation (4.4) into a range of possible values for each considered timestamp. The mean main bearing temperature is then used to calculate the residuals as follows.

1. Residuals associated with measured mean SCADA temperatures falling within the healthy operating region are assumed equal to 0:

$$T_{mes}(t) < Up_{threshold}(t) \quad \& \quad T_{mes}(t) > Low_{threshold}(t) \quad \Rightarrow \quad Res(t) = 0 \tag{4.12}$$

2. For measurements falling outside this healthy operating range, the residuals are calculated as the difference between the measured main bearing mean temperature and the closest threshold. If the

measured main bearing mean temperature is higher than the $Up_{threhsold}(t)$, the residual is calculated as:

$$T_{mes}(t) > Up_{threshold}(t) \quad \Rightarrow \quad Res(t) = T_{mes}(t) - Up_{threshold}(t) \tag{4.13}$$

3. If the measured main bearing mean temperature is lower than the $Low_{threhsold}(t)$, the residual is calculated as:

$$T_{mes}(t) < Low_{threshold}(t) \quad \Rightarrow \quad Res(t) = T_{mes}(t) - Low_{threshold}(t) \tag{4.14}$$

Figure 4.9 illustrates the proposed residual calculation method. The data points represent measurements, and the range between the threshold region between $Up_{threhsold}(t)$ and $Low_{threhsold}(t)$ shows the threshold region. The figure illustrates the residual calculation depending on the value of the measured temperature.

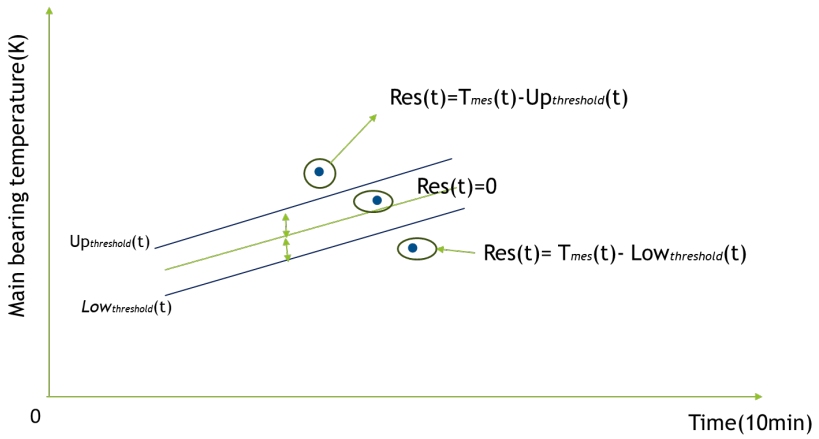

Figure 4.9: Proposed residual calculation method

Density of threshold region

This thesis proposes the construction of a novel HI based on the assumption that the threshold region represents the healthy-bearing state. As the component approaches a failure, the number of points within this region is expected to decrease, indicating a deterioration of its health. The density of the threshold region is proposed as HI to monitor the amount of measurements falling within the threshold region. Consequently, the density of the threshold region should reach its lowest value just before a failure. The density of the threshold region is calculated as:

$$\rho_{threshold\_region}(\Delta t) = \frac{N_{threshol\_region}(\Delta t)}{N_{total}(\Delta t)} \tag{4.15}$$

where for each time frame Δt, $N_{threshol\_region}$ is the number of measurements falling within the threshold region, and N_{total} is the total number of available measurements. To simplify the calculation of the density of the threshold region, the residuals are classified according to the binary value of an indicator L:

$$\begin{aligned} T_{mes}(t) < Up_{threshold}(t) \quad \& \quad T_{mes}(t) > Low_{threshold}(t) \quad \Leftrightarrow Res(t) = 0 \Rightarrow \quad L(t) = 1 \\ T_{mes}(t) > Up_{threshold}(t) \quad || \quad T_{mes}(t) < Low_{threshold}(t) \quad \Leftrightarrow Res(t) \neq 0 \Rightarrow \quad L(t) = 0 \end{aligned} \tag{4.16}$$

For measurements that fall in the threshold region $L(t) = 1$, while for measurements falling outside the threshold region $L(t) = 0$. Then Equation (4.15) for a given time frame t can be written as the mean of the indicator values:

$$\rho_{threshold\_region}(\Delta t) = \frac{1}{Length(\Delta t)} \sum_{i=0}^{Length(\Delta t)} L(t_i) \tag{4.17}$$

Tautz-Weinert [104] analysed multiple case studies where various NBM techniques were applied to model the gearbox temperature. Figure 4.10 illustrates identified patterns in the NBM residuals before failure, where the red line is the moving average of the residuals.Typical identified patterns were:

1. 'Rise'- Slow increase in the temperature trend. Figure 4.10(a) shows this upward trend in the residuals.
2. 'Spread'- Increase in dispersion of the residuals before failure. In Figure 4.10(b) the region between the two orange lines demonstrates high fluctuation of the residuals.
3. 'Spike' - Fast increase in residuals in the scale of hours. In Figure 4.10(c), the arrow indicates a spike in temperature residuals.

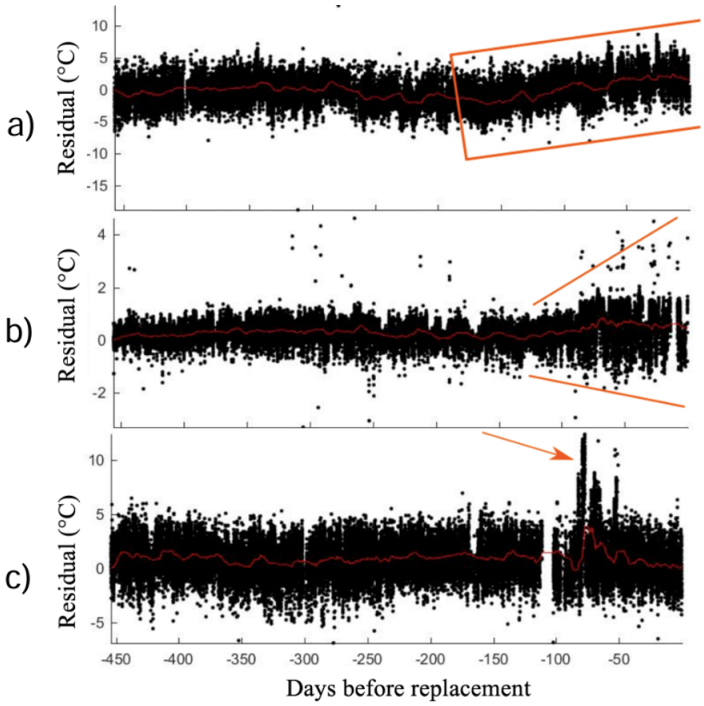

Figure 4.10: Residual patterns associated with the abnormal behavior of a turbine component [53].

According to Murgia et al. [53], if none of the known NBM residual patterns shown in Figure 4.10 are present in the test set, the validation of the SCADA-based condition monitoring method is not possible. Compared to conventional NBM residuals, the proposed approach based on the density of the threshold region is expected to remain consistent across different failures, as the proposed HI does not depend on the magnitude of the deviation.

It is important to note that this thesis compares the performance of the residuals obtained using the baseline NBM proposed by Cambron et al. with the proposed novel HI. While the unit of the residual-based HI is Kelvin (K), the density of the threshold region is adimensional. Thus, normalization is necessary to enable the comparison of these HIs. This thesis uses 'StandardScaler' from the Scikit Learn library in Python, where normalization can be described as:

$$HI'(t) = \frac{HI(t) - \bar{HI}}{\sigma_{HI}} \tag{4.18}$$

Where HI' is the normalized HI, $\bar{HI}$ is the mean, and σ is the STD of the HI.

The density of the threshold region represents a novel approach to obtaining an HI using NBM, and this is made possible thanks to the introduction of Step M. The proposed HI takes into account the variability of the main bearing operating conditions within each 10-minute time frame and aims to enable accurate monitoring of the degradation trend.

4.3.3. Average over-interval and EWMA steps

The average over-interval step and EWMA step serve two primary purposes: data reduction and smoothing. This makes the identification of anomalies in the HI easier. The average over-interval step reduces the number of analyzed data points by calculating their average over a specific time interval. This is a common

post-processing method applied in condition monitoring. Various averaging windows are implemented in the literature. Herp et al. [60] analyze hourly resampled residuals obtained from an ANN model, while Cambron et al.[32] use daily averaged residuals. Enclada et al. [1] define HI as the number of times temperature residual exceeded the threshold throughout one week. Similar to Encalda et al., Tutiven et al. [52] use weekly averaged classifications from 1-class SVM as HI. The aim of using averaged HI is to increase the signal-to-noise ratio and reduce the amount of false detections.

Although the choice of the averaging window can be determined through trial and error, this study focuses on comparing the proposed method with the baseline method. Therefore, the specific choice of the averaging interval becomes less critical as long as it remains consistent for both compared methods. However, it is important to note that the chosen averaging intervals should still be reasonable and appropriate for condition monitoring. The ”resample” function in the Pandas library is used to perform the averaging over-interval step.

An EWMA is then applied to smooth the obtained HI [52, 32]. This thesis uses EWMA as this was used in the baseline paper [32]. The ”ewm” function from the Pandas library is employed to perform smoothing and is described as:

$$Z(t) = \lambda HI(t) + (1 - \lambda)HI(t - 1) \tag{4.19}$$

where Z is the smoothed values of the HI and λ is the smoothing factor. Higher λ values mean less smoothing, while lower λ values mean stronger smoothing. Cambron et al. [32] select the value of λ using the lookup tables provided in [105]. The choice of λ is based on how early the designed framework is expected to perform detection. The primary focus of this study is to demonstrate the advantages of the proposed approach compared to the baseline framework proposed in [32] and described in Figure 4.1. As in the case of the average over-interval step, the specific choice of the λ becomes less critical as long as it remains consistent for both the baseline and proposed methods.

4.4. Overview

The proposed method is summarised by the flowchart shown in Figure 4.11. Initially, the method applies Step S, described in Section 4.3.1, to obtain N sets of coefficients of Equation (4.4). Next, Step M is applied to estimate the Lower and Upper thresholds for each timestamp of the test set, as described in Section 4.3.2. Residuals are calculated according to what is shown in Figure 4.9. To build the proposed HI, the residuals are then classified according to Equation (4.16). The average over-interval step of classified values is calculated to obtain the density of the threshold region, followed by the EWMA smoothing step to obtain HI for the degradation trend monitoring.

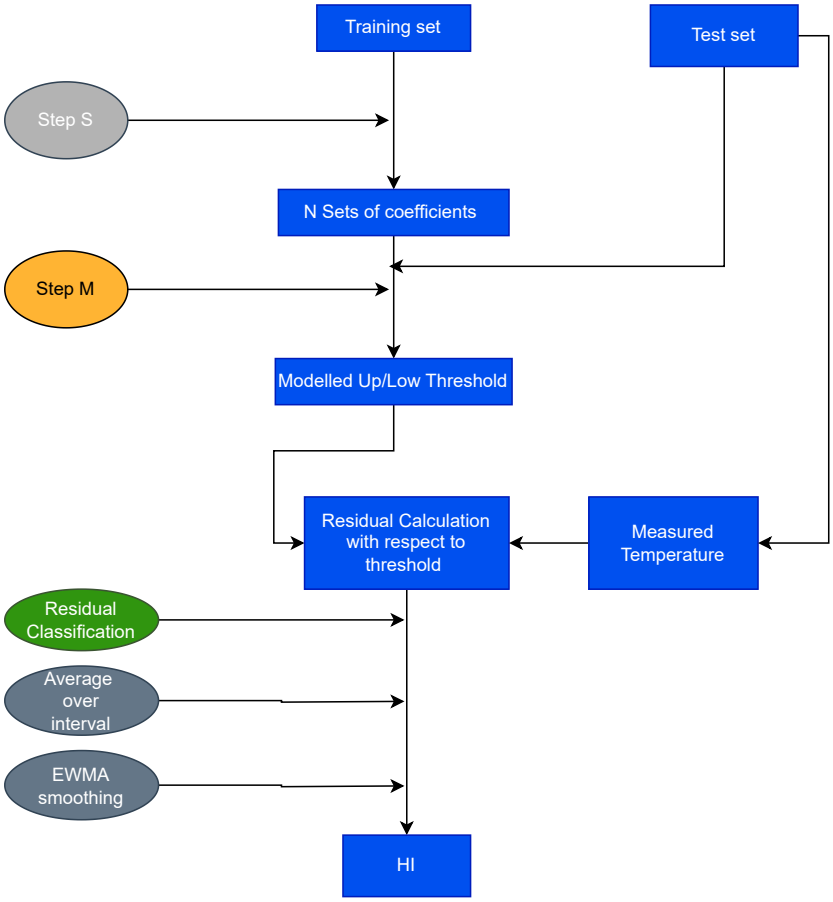

Figure 4.11: Overview of the proposed approach

5

Results

This chapter presents the results of two case studies conducted using the approach proposed in Chapter 4. The first case study refers to a wind farm that did not experience any failure, while the second case refers to a wind turbine experiencing a failure of the main bearing. This chapter aims to perform a comparison between the baseline HI described in Cambron et al. [32] and the HI obtained using the methodology proposed in this thesis.

Each case study is described according to the following structure: first, the dataset is introduced. Next, a description of how the general methodology proposed in Chapter 4 has been adapted to each case study is given. Subsequently, dataset prepossessing is shown, and the results are presented and discussed.

5.1. Case Study 1: Vaudeville-le-Haut wind farm

The Vaudeville-le-Haut wind farm is located in France and consists of four REpower MM82 onshore turbines, each with a rated capacity of 2 MW and a diameter of 82 meters. The available SCADA dataset covers the period from 2013 to 2018 and includes a range of sensor measurements. The dataset includes records of the temperature of various components and the nacelle, the ambient temperature; environmental condition records such as wind speed and wind direction; power production-related records such as power produced, grid frequency, and generator rotational speed. For each SCADA measurement, the mean, STD, min, and max values are provided. The SCADA measurements available for the Vaudeville-le-Haut wind farm are provided in Table A.1 in Appendix A. This SCADA dataset lacks the turbines' status codes and maintenance records.

5.1.1. Adapted methodology

Since the Case Study 1 dataset does not include run-into-failure data, the post-processing steps have been slightly modified compared to what is presented in Chapter 4. A schematic representation of the adopted baseline approach to obtain $HI_{Res\_Baseline}$ is shown in Figure 5.1, while the method proposed to obtain the density of the threshold region HI referred to HI_{Alt} is illustrated in Figure 5.2. Moreover, Case Study 1 compares the HIs obtained after implementing each step of the proposed approach shown in Figure 5.2 against the HI obtained using the baseline method illustrated in Figure 5.1. Table 5.1 summarises the nomenclature used to define the HIs. Thus, apart from comparing $HI_{Res\_Baseline}$ and HI_{Alt}, this case study also analyzes the effects of the intermediate steps HI_{Res_S} and $HI_{Res\_S\_M}$. Figure 5.3 illustrates the method utilizing Step S to obtain HI_{Res_S}, while Figure 5.4 shows the approach applying Step S and Step M to obtain residual-based HI ($HI_{Res\_S\_M}$).

Table 5.1: Case Study 1 - Nomenclature of the HIs is calculated with the baseline approach and after the implementation of each step of the proposed methodology

Method	HI	Flowchart
Baseline	$HI_{Res\_Baseline}$	Figure 5.1
Step S	HI_{Res_S}	Figure 5.3
Step S and Step M	$HI_{Res\_S\_M}$	Figure 5.4
Step S and Step M density of threshold region	HI_{Alt}	Figure 5.2

Compared to the general method presented in Section 4.4, in this case study, the EWMA smoothing step is not performed, as shown in Figures 5.1 and 5.2. This adaptation is made because the reference study uses EWMA as part of the fault detection framework [32]. However, due to the lack of relevant data, in this case study the aim is only to analyze and compare the performance of the HIs. Consequently, the final step for compared methods in this case study is averaging the over-interval step. Notably, these methods use separate turbines as testing and training data sets, which is consistent with the approach adopted by Cambron et al. [32]. Moreover, the average over one-day period is adopted for consistency with the daily averaged interval employed by Cambron et al. (Chapter 4.1).

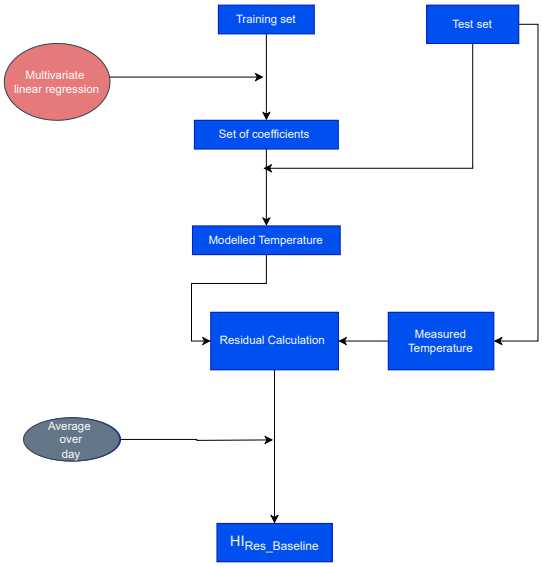

Figure 5.1: Case Study 1 - Baseline method to calculate $HI_{Res\_Baseline}$

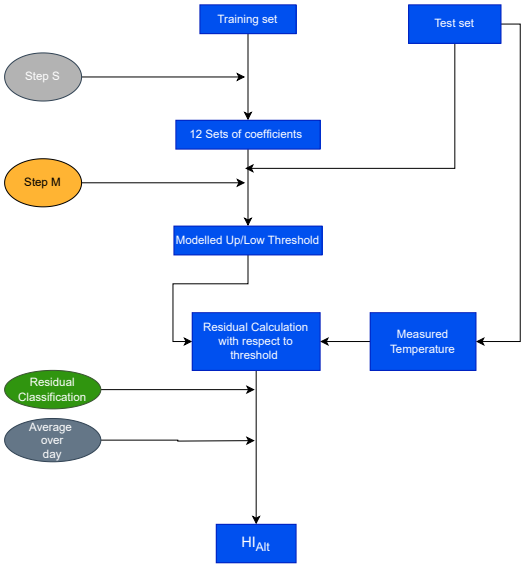

Figure 5.2: Case Study 1 - Proposed method, implementation of Step S and Step M density of threshold region to calculate HI_{Alt}

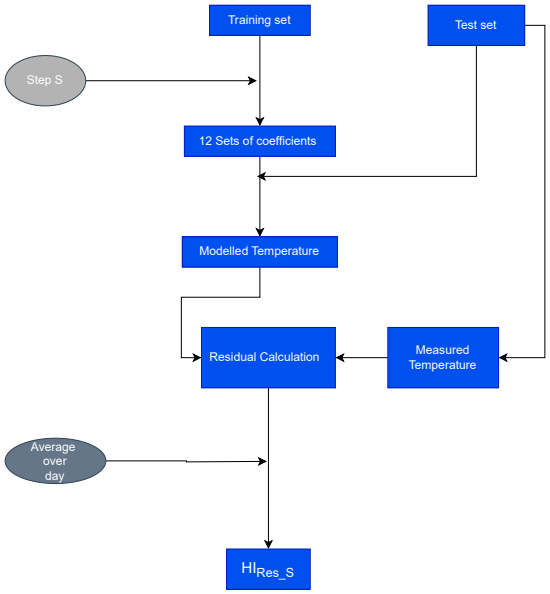

Figure 5.3: Case Study 1 - Implementation of Step S to calculate HI_{Res_S}

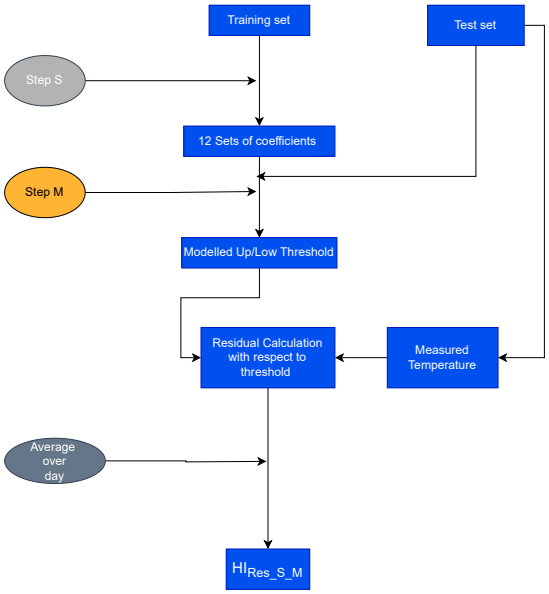

Figure 5.4: Case Study 1 - Implementation of Step S and Step M to calculate $HI_{Res\_S\_M}$

For Case Study 1, the remainder of this Section is structured as follows. Section 5.1.2 presents the wind turbines chosen for the model training and testing. Section 5.1.3 describes the pre-processing steps applied to the training and testing datasets. Section 5.1.4 shows $HI_{Res\_Baseline}$ obtained using baseline approach. Section 5.1.5 presents HI_{Res_S} obtained employing Step S. Section 5.1.6.1 explores $HI_{Res\_S\_M}$ based on the residuals obtained using Step S and Step M. Section 5.1.6.2 outlines HI_{Alt} based on the density of the threshold region obtained using Step S and Step M.

5.1.2. Wind turbine selection

Status codes and maintenance records usually help to define training and testing sets. When records indicate maintenance activities on the monitored component, employing the dataset corresponding to this period for training should be avoided, as for building reliable NBMs, it is crucial to use datasets representing healthy operation. On the other hand, as this study focuses on degradation trend monitoring, having status codes and maintenance records would enable an easily defined testing set to perform a comparative analysis of the HIs. However, status codes and maintenance records from the wind farm under investigation are not available. To address this limitation, the choice of testing and training turbine is based on the assumption that a gradual increase in the main bearing temperature indicates the evolution of the components' degradation process. Numerous studies correlate a gradual increase in the main bearing temperature with health deterioration of the component [43, 25, 56, 24, 30].

A rolling average window of one year was applied to the main bearing temperature signals of the four turbines to determine which main bearings temperature indicates components undergoing a degradation process. Figures 5.5 and 5.6 show the yearly rolling average of Turbine A and Turbine C during 5 years of operation. The data from these two turbines have been selected as the testing and training sets, respectively. A gradual increase from 25.3 C^0 to 28.3 C^0 of the rolling main bearing temperature can be observed in Figure 5.5. This can be seen as an indicator of the bearing health deterioration. Thus, Turbine A is regarded as a reasonable candidate for degradation trend monitoring, and its dataset is selected as the test set. In contrast, Figure 5.6 shows an almost stable rolling average main bearing temperature of around 27 C^0 for Turbine C. Thus, based on the assumption that a stable main bearing temperature over the analyzed period indicates a healthy component, the turbine C dataset was selected as the training set for building the NBM. The other two turbines, Turbines B and D, were disregarded due to drastic fluctuations and unexpected temperature signal behavior, as shown in Appendix A.2.

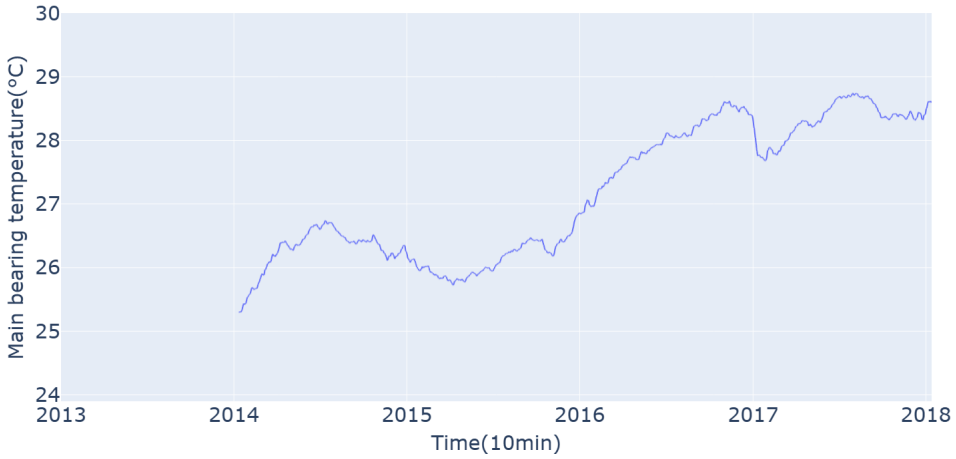

Figure 5.5: Case Study 1 - Yearly rolling average of the Turbine A main bearing temperature

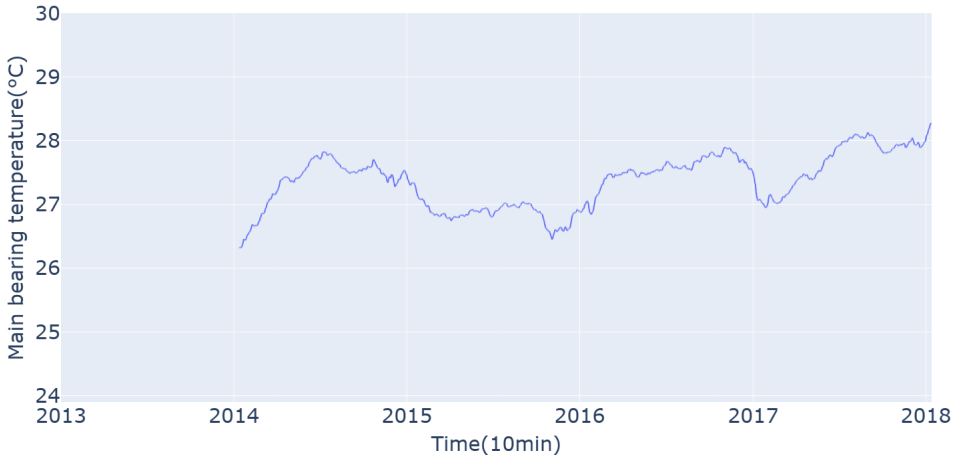

Figure 5.6: Case Study 1 - Yearly rolling average of the Turbine C main bearing temperature

5.1.3. Data cleaning

Data cleaning is an essential step in data analysis. Throughout the operation, sensors and the SCADA system may experience a malfunction, which leads to abnormal recordings and gaps in the records. Abnormal records in the training set can compromise the construction of a reliable NBM that accurately captures the healthy behavior of the component. Furthermore, within the test set, these records can reduce the accuracy of the NBM and can potentially undermine the analysis of the obtained results.

The data cleaning process adopted in this work is outlined in Table 5.2, which shows the number of samples dropped for both the training and test turbine datasets after each cleaning step. First, duplicate timestamps were removed to ensure data integrity. Additionally, negative power values were replaced by zero values, as these values do not have a physical meaning with regard to the main bearing temperature model (Equation (4.4)). Moreover, a basic filtering process was implemented to remove outliers. Main bearing temperatures above 70 C^0 and below -20 C^0 were dropped. These thresholds were determined empirically by analyzing the mean main bearing temperature SCADA records. Moreover, records containing ”Nan” values were dropped. Notably, after applying the cleaning steps, approximately 95% of the data was usable for further analysis.

Table 5.2: Case Study 1 - Data cleaning process

	Number of Training Data (Turbine C)	Number of Test Data (Turbine A)
Original available data points	264528	264528
Duplicate timestamps dropped	76	77
Outliers dropped	1653	2074
Nan values dropped	7053	5950
Data used	255745	256427

5.1.4. Baseline approach

Following the baseline method presented in Figure 5.1, the coefficients of Equation (4.4) have been obtained by applying multivariate linear regression to the whole training set. The values of the obtained coefficients are shown in Table 5.3. Notably, β_1 indicates that the main bearing temperature is highly auto-correlated and is the most significant contributor to the main bearing temperature model.

Table 5.3: Case Study 1 - Main bearing temperature model coefficients of Equation (4.4)

Coefficients	Case Study 1
β_1	0.984
β_2	0.0151
$\beta_3(K * s^2/rad^2)$	0.0662
$\beta_4(K/kW)$	0.000021

Using coefficients in Table 5.3, the main bearing temperature was modeled for the test dataset (Figure 5.1). Figure 5.7 shows the modeled and measured main bearing temperatures for the test wind turbine. Additionally, Figure 5.8 presents a zoomed-in section between the 7th and 10th of May 2014, allowing both measured and modeled temperatures to be shown clearly.

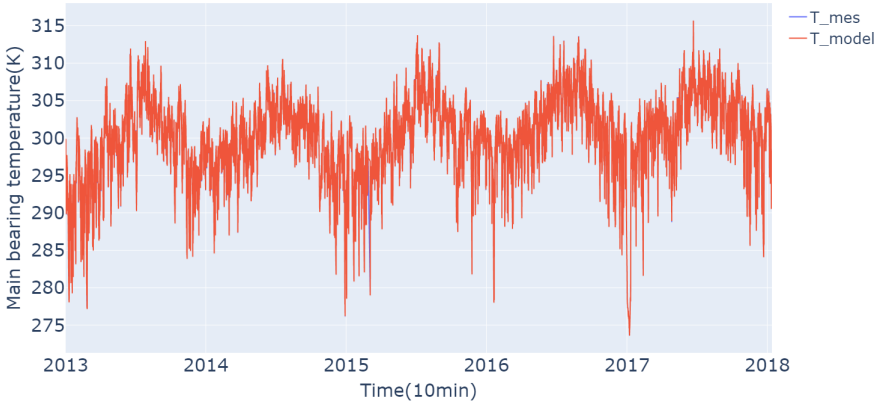

Figure 5.7: Case Study 1, Test set - Modelled and measured main bearing temperature

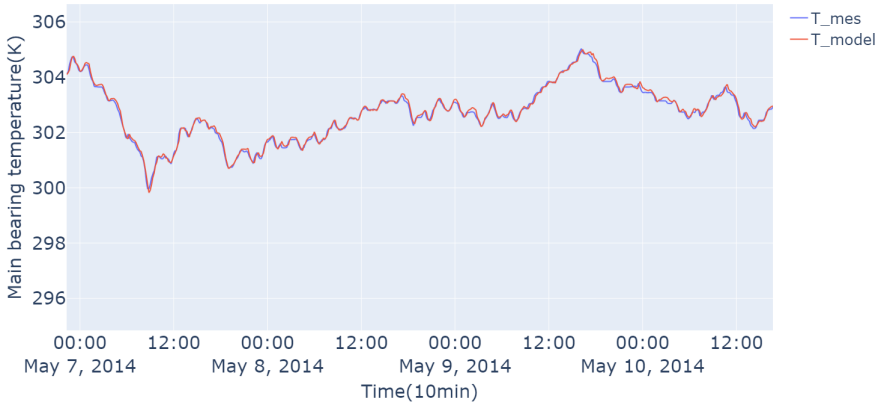

Figure 5.8: Case Study 1, Test set - Modelled and measured main bearing temperature, zoom-in view in the period between May 7 and May 10 of 2014

High seasonal fluctuation in the main bearing temperature can be observed in Figure 5.7, with lows in the winter and peaks in the summer. Figure 5.9 illustrates the measured main bearing and ambient temperatures between 2013 and 2018 of the test turbine. Seasonal fluctuations present in the main bearing temperature could be a consequence of no cooling system present in the nacelle, which leads to a high correlation between the main bearing temperature and ambient temperature, which has been calculated to be equal to 0.78. Moreover, it should be added that there were no records of the cooling system in the SCADA dataset (Appendix A.1).

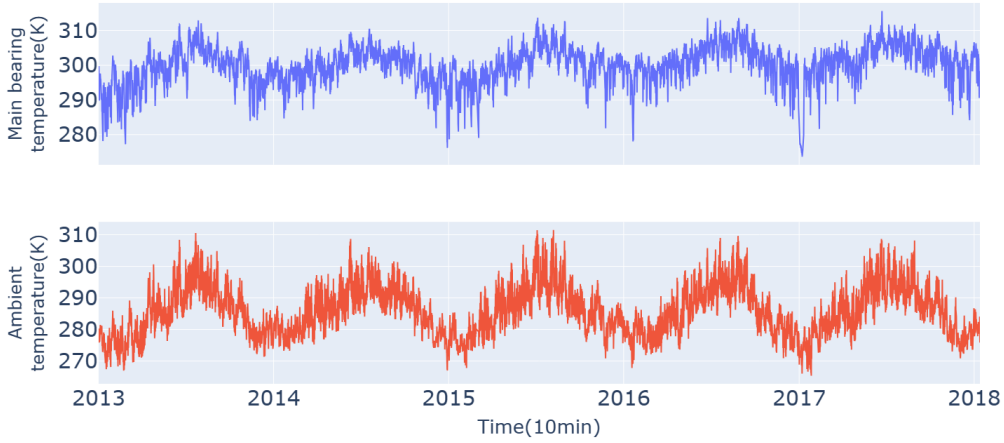

Figure 5.9: Case Study 1, Test set - Measured main bearing and ambient temperatures

The baseline $HI_{Res\_Baseline}$ for the test set for the period 2013-2018 is calculated according to the approach shown in Figure 5.1 as the daily average of the difference between the modeled and measured main bearing temperatures shown in Figure 5.7. The obtained $HI_{Res\_Baseline}$ for the whole test set is presented in Figure 5.10.

The gradual increase in $HI_{Res\_Baseline}$ observed in Figure 5.10 is attributed to the progressive degradation of the main bearing. The degradation of the component's health changes the model relationship, consequently resulting in a deviation from the established NBM. This shift can be observed by a gradual increase in HI. Seasonal fluctuations in $HI_{Res\_Baseline}$, with positive and negative peaks occurring during summer and winter, respectively, can be observed in Figure 5.10. They are an indication of the limitations in describing the main bearing temperature with a single set of coefficients.

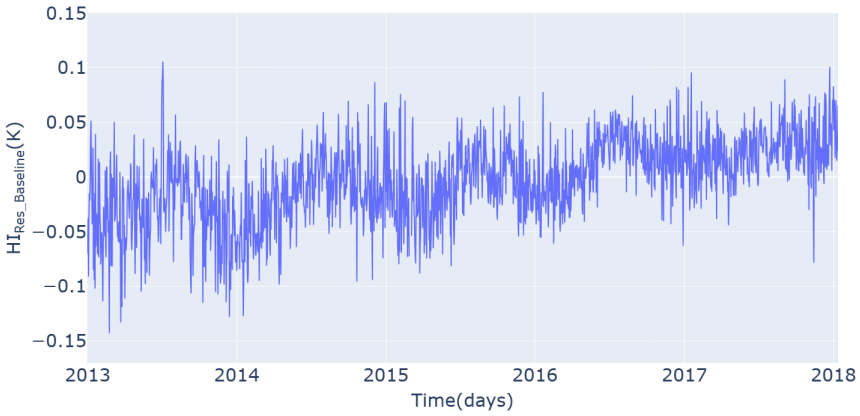

Figure 5.10: Case Study 1, Test set - Baseline approach HI, $HI_{Res\_Baseline}$

5.1.5. Step S

To take into account the seasonality effects, Step S described in Section 4.3.1 has been implemented. HI (HI_{Res_S}) for the test set is calculated according to the flowchart shown in Figure 5.3. The training set, which includes data from 5 different years, has been divided into twelve groups, each corresponding to the data from the same month. Twelve sets of coefficients of Equation (4.4) have been obtained by applying multivariate linear regression to the monthly grouped training sets. In this way, it is possible to model independently the behavior of the main bearing temperature in each month of the year.

Different data divisions, such as grouping the data according to two seasons (colder months, September-February/hotter months, March-August) or quarterly periods (four seasons), have also been explored. These data divisions are presented and discussed in Appendix A.3. The decision to adopt a twelve-month division was motivated by the fact that this approach results in the lowest RMSE, calculated for the modeled main bearing temperature and cross-correlation with ambient temperature when fitting the equation to the test set. The twelve sets of coefficients are shown in Table A.3.

The monthly coefficients obtained from the approach depicted in Figure 5.3 were used to model the main bearing temperature in the test set. The same residual calculations and daily averaging steps as in the case of $HI_{Res\_Baseline}$ were applied to calculate HI_{Res_S}. The resulting HI_{Res_S} for the test set is shown in Figure 5.11.

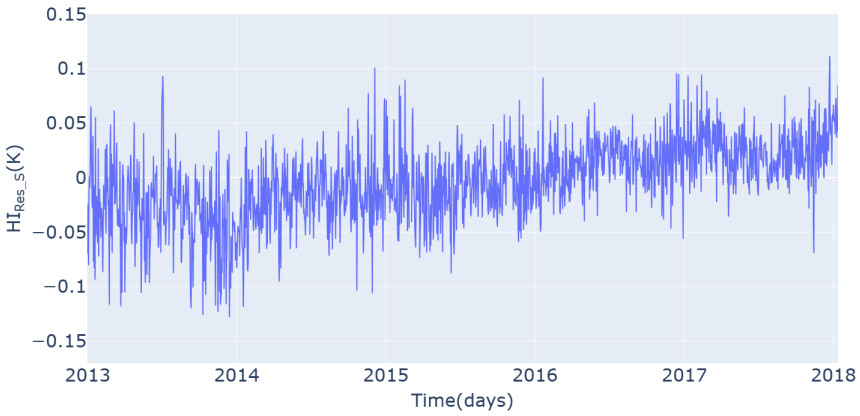

Figure 5.11: Case Study 1, Test set - Step S HI, HI_{Res_S}

Compared to the $HI_{Res\_Baseline}$ shown in Figure 5.10, HI_{Res_S} shows lower seasonal variations. This reduction is also confirmed by the values of the cross-correlation of those HIs with ambient temperature presented in Table 5.4.

Table 5.4: Case Study 1 - Cross-correlation of $HI_{Res\_Baseline}$ and HI_{Res_S} with the ambient temperature

Series	$HI_{Res\_Baseline}$	HI_{Res_S}
Ambient temperature	0.369	0.159

Table 5.5 presents the performance metrics, as discussed in Section 3.3.2, for the baseline model ($Model_{Baseline}$) and the seasonality model ($Model_S$). There are no noticeable changes in the model performance metrics, suggesting that the proposed seasonality step successfully mitigates the impact of seasonality on the monitored HI without compromising the model's fit to the test data.

Table 5.5: Case Study 1 - Baseline and Seasonality model performance metrics

Metric	$Model_{Baseline}$	$Model_S$
RMSE (K)	0.1244	0.1237
R^2	0.9995	0.9995
MAE (K)	0.0777	0.0772
MAPE (%)	0.32	0.32

5.1.6. Step M

In order to consider the variability of operating conditions within a 10-minute timeframe, Step M, as explained in Section 4.3.2, is implemented. With the monthly coefficients obtained from Step S, the main bearing temperature for each timestamp in the test set is modeled using the Monte Carlo method. This yields upper and lower thresholds for each timestamp as an outcome of Step M. In this section, the residual-based HI ($HI_{Res\_S\_M}$) is presented. Additionally, the HI based on the density of the threshold region (HI_{Alt}) is introduced.

Step M, HI based on residual

HI ($HI_{Res\_S\_M}$) has been obtained using the method presented in Figure 5.4. The upper and lower thresholds obtained for each timestamp are used to calculate the residuals, as described in Section 4.3.2.1. According to this approach, 35.4% of the measured mean bearing temperature fell within the inner threshold region where the residuals are assumed to be equal to 0, as described in Equation (4.12). Similarly to the previous steps, the calculated residuals were averaged daily to obtain $HI_{Res\_S\_M}$, which is shown in Figure 5.12.

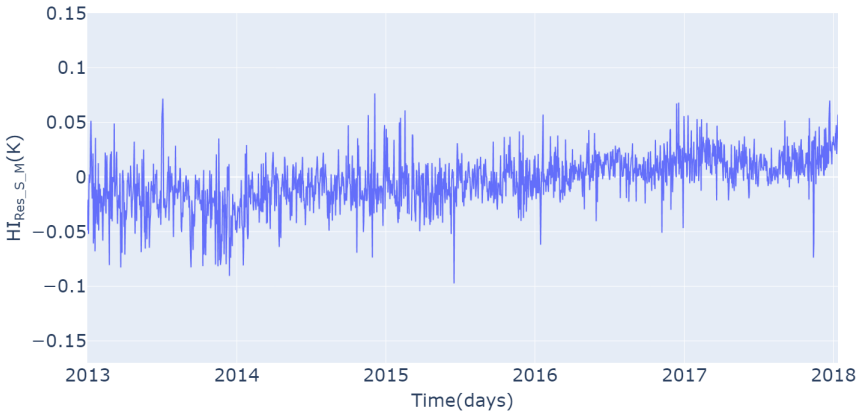

Figure 5.12: Case Study 1, Test set - Step S and Step M HI, $HI_{Res\_S\_M}$

Similarly to $HI_{Res\_Baseline}$ and HI_{Res_S}, $HI_{Res\_S\_M}$ illustrates an upward trend throughout the 5 years of operation. Moreover, no significant seasonal fluctuations can be observed, and the cross-correlation of $HI_{Res\_S\_M}$ with ambient temperature is 0.137.

The performance of the three HIs is compared in terms of monotonicity and dispersion in Figures 5.13, 5.14, and 5.15. The monotonicity of the HIs, shown in Figure 5.13, is calculated with the MK τ monotonicity metric described in Section 3.3.1. Their dispersion is quantified using the MSE and Noise metrics described in Section 4.2.2 and is shown in Figure 5.14 and Figure 5.15, respectively.

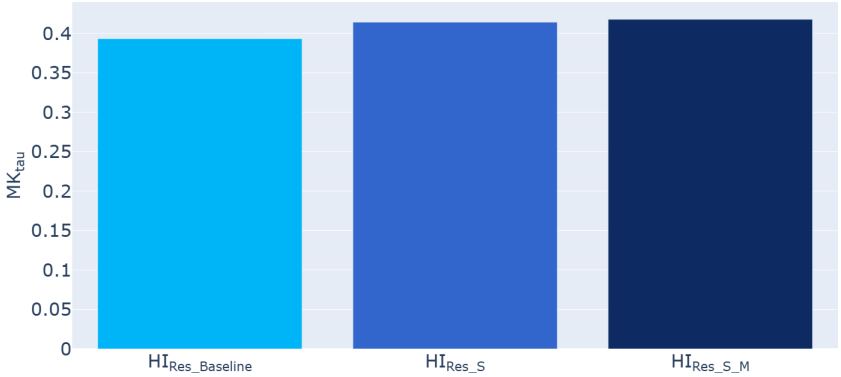

Figure 5.13: Case Study 1 - $HI_{Res\_Baseline}$, HI_{Res_S} and $HI_{Res\_S\_M}$ monotonicity comparison using MK τ

Figure 5.13 shows that $HI_{Res\_S\_M}$ has the highest degree of monotonicity, with a value of MK τ equal to 0.417, against values of 0.39 and 0.414 for $HI_{Res\_Baseline}$ and HI_{Res_S}, respectively. However, this improvement in monotonicity is only 7% with respect to the baseline approach. This minor improvement observed for $HI_{Res\_S\_M}$ may be attributed to the weak upward trend of the main bearing temperature shown in Figure 5.5 due to no run-into failure data available. In contrast, a run-into-failure test set is expected to have a more evident upward trend since deviation from the healthy condition is expected to increase as the component approaches failure.

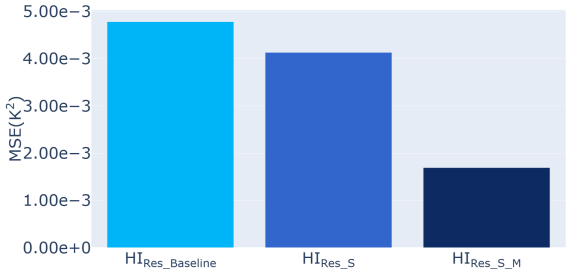

Figure 5.14: Case Study 1 - $HI_{Res\_Baseline}$, HI_{Res_S} and $HI_{Res\_S\_M}$ dispersion comparison using MSE

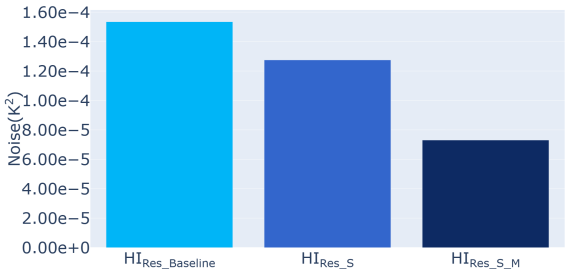

Figure 5.15: Case Study 1- $HI_{Res\_Baseline}$, HI_{Res_S} and $HI_{Res\_S\_M}$ dispersion comparison using Noise

Figure 5.14 shows that $HI_{Res\_S\_M}$ is characterized by the lowest dispersion in terms of MSE (1.7e-3K^2) when compared to that of $HI_{Res\_Baseline}$ (4.7e-3K^2) and HI_{Res_S} (4.1e-3K^2). Similarly, Figure 5.15 illustrates that $HI_{Res\_S\_M}$ exhibits the lowest level of Noise (7.3 e-5K^2) in comparison to $HI_{Res\_Baseline}$ (1.53e-4K^2) and HI_{Res_S} (1.27e-4K^2). The CEEMDAN decomposition of the three HIs done to obtain the Noise values is illustrated in Appendix A.4.1.1.

When comparing two different methods for measuring the HI dispersion, it can be seen that in relative terms, both the MSE and the Noise metrics show that $HI_{Res\_Baseline}$ is the most dispersed, while $HI_{Res\_S\_M}$ is the least dispersed. The significant reduction in the dispersion of the $HI_{Res\_S\_M}$ is directly related to the method proposed for the calculation of the NBM residuals. As residuals are calculated with respect to threshold values, the magnitude of the $HI_{Res\_S\_M}$ is lower compared to $HI_{Res\_Baseline}$ and HI_{Res_S}.

Reducing the magnitude of NBM residuals leads to a reduction in the dispersion of the obtained HI. Notably, even though $HI_{Res\_S\_M}$ displays the lowest dispersion and highest monotonicity, to assess the superiority of the degradation trend monitoring using $HI_{Res\_S\_M}$, it is recommended to apply this approach to alternative case studies with available run-into-failure data.

Step M, HI based on the density of the threshold region

HI_{Alt} is calculated according to the method described in Figure 5.2. Similarly to the case of $HI_{Res\_S\_M}$, the residuals are calculated with respect to upper and lower thresholds for each timestamp of the test set. Subsequently, the calculated residuals are classified according to Equation (4.16) and averaged over a day to obtain the daily density of the threshold region (HI_{Alt}), according to Equation (4.17). Figure 5.16 shows HI_{Alt} for the test dataset.

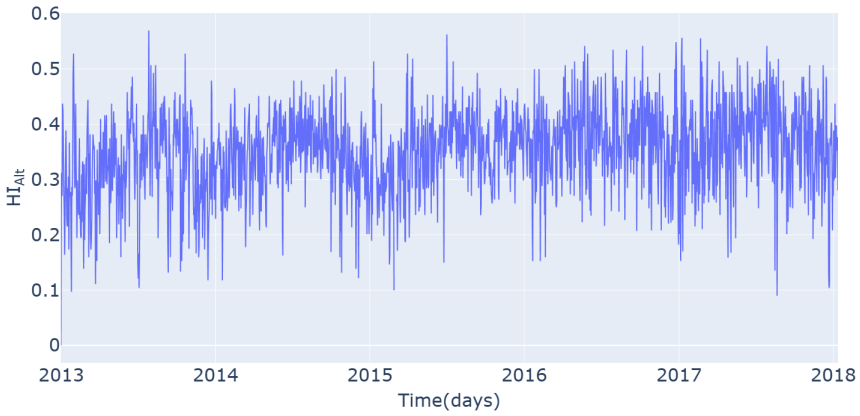

Figure 5.16: Case Study 1, Test set - Step S and Step M density of threshold region HI, HI_{Alt}

Compared to the $HI_{Res\_Baseline}$, shown in Figure 5.10, no significant upward trend can be observed in the HI_{Alt}. Moreover, seasonal fluctuations are evident in the HI_{Alt}. Notably, the cross-correlation between HI_{Alt} and the ambient temperature is 0.298, which is 19% less than the Baseline HI. Moreover, the reason for this metric to be higher than HI_{Res_S} (0.159) is attributed to the lower trend present in the HI_{Alt}.

$HI_{Res\_Baseline}$ and HI_{Alt} are compared using MK τ, MSE, and Noise metrics as shown in Figures 5.17, 5.18, 5.19, respectively. Since the unit of $HI_{Res\_Baseline}$ is Kelvin (K) while HI_{Alt} is adimensional, they are first normalized using Equation (4.18) to enable their comparison.

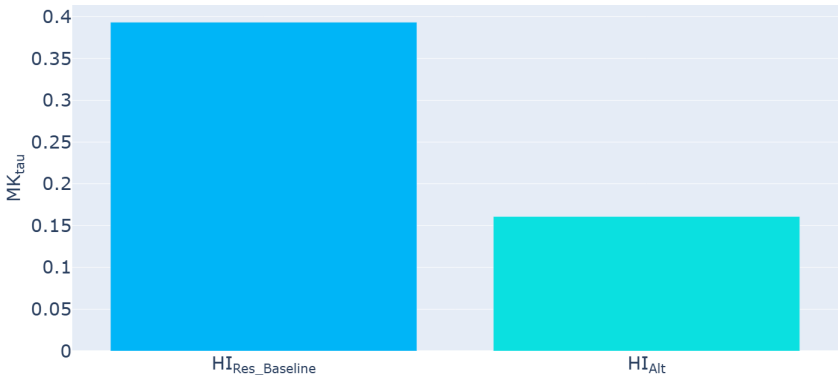

Figure 5.17: Case Study 1 - $HI_{Res\_Baseline}$ and HI_{Alt} monotonicity comparison using MK τ

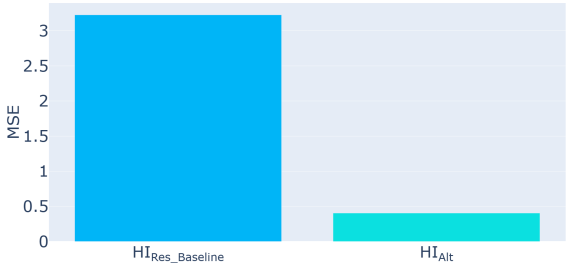

Figure 5.18: Case Study 1 - $HI_{Res\_Baseline}$ and HI_{Alt} dispersion comparison using MSE

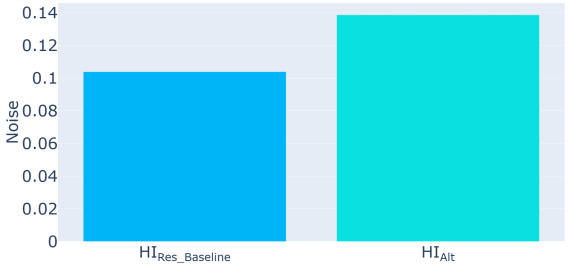

Figure 5.19: Case Study 1 - $HI_{Res\_Baseline}$ and HI_{Alt} dispersion comparison using Noise

Figure 5.17 shows that the lower monotonicity of HI_{Alt} compared to $HI_{Res\_Baseline}$, further confirming what was observed when comparing their behavior over time in Figures 5.16 and 5.10, respectively. The absence of a significant trend in HI_{Alt} is attributed to the lack of a main bearing failure event in the analyzed dataset. When looking at the MSE dispersion metric, Figure 5.18 shows the lower value for HI_{Alt} (0.4) compared to $HI_{Res\_Baseline}$ (3.2). On the other hand, the comparison in terms of the Noise metric in Figure 5.19 shows that HI_{Alt} has a higher value of Noise (0.13) than $HI_{Res\_Baseline}$ (0.1). The CEEMDAN decomposition to obtain the Noise values of the compared HIs is shown in Appendix A.4.1.2.

The MSE metric indicates greater dispersion for $HI_{Res\_Baseline}$, whereas according to the Noise metric, HI_{Alt} exhibits a higher level of dispersion. The discrepancy in dispersion metrics is attributed to the linear reference degradation trend assumption made when obtaining MSE, as described in Section 4.2.2. As HI_{Alt} represents a more linear trend than $HI_{Res\_Baseline}$, MSE shows lower values for HI_{Alt}. Thus, the dispersion MSE metric is significantly affected by how well the assumed reference degradation trend fits the data. In the case of the MSE metric, the dispersion of the HI is artificially increased due to linear assumption. On the other hand, the Noise metric indication of the $HI_{Res\_Baseline}$ being less dispersed is attributed to its higher monotonicity compared to the HI_{Alt}. As HI_{Alt} has a less evident trend according to MK τ (Figure 5.17), it is more dispersed than $HI_{Res\_Baseline}$, which can also be observed in Figure 5.16

The daily density of the threshold region was proposed as a novel approach for the analysis of the NBM residuals. However, in this case study, the adoption of this approach does not bring substantial improvements compared to the baseline case. This lack of improvement can be associated with the absence of component failure in the dataset over the analyzed period. As mentioned before, the run-into failure test is anticipated to exhibit a significant trend in HI_{Alt} as the deviation from the healthy state is expected to increase as the component is closer to the failure date. The analysis of at least one case study containing run-into failure is essential to demonstrate the advantages of adopting the density of the threshold region as HI.

5.2. Case Study 2: Wind turbine with main bearing failure

The second case study analyzes the performance of a 2.3 MW wind turbine using the SCADA data provided by the University of Strathclyde. The data spans from July 2019 to November 2020 and covers the turbine's operation until the occurrence of a failure of the main bearing [106]. Due to the features of this particular SCADA dataset, a few adjustments were made to the methodology proposed in Chapter 4. This section first describes the dataset. Next, it discusses the modifications implemented to the proposed methodology. Finally, the HIs are obtained using the adapted proposed approach and compared with the baseline results, following a procedure based on sequential steps similar to Case Study 1.

5.2.1. SCADA dataset

The date of the failure is needed to filter the subsequent records, as they are irrelevant to the analysis. From the previous work using the same dataset [106], it is known that the main bearing failure occurred at the end of November 2020. However, due to a lack of status codes and maintenance records, the exact date of the occurrence of the main bearing failure is unknown. Moreover, the dataset does not include the mean wind speed records, which makes differentiating between wind turbine not producing power due to lack of available wind speed or due to failure of the component not straightforward. SCADA records of the main bearing temperature, the produced power, and the rotational speed of the rotor are analyzed to determine the date of the failure. Figure 5.20 shows them in the period corresponding to the last two weeks of November 2020.

Rated power production and the high main bearing temperature can be observed on the evening of the 24th. This is followed by the power production cut and cooling down of the main bearing and drop in the rotational speed, indicated by the vertical black line. Figure 5.20 shows that the turbine is back in operation, generating electricity on 30th November (vertical purple line). Based on this analysis, November 24th was selected as the date of the occurrence of the main bearing failure.

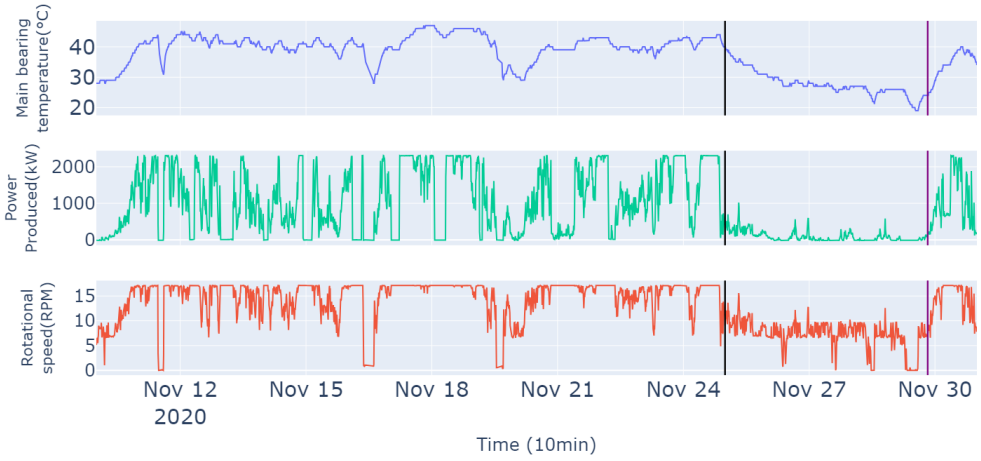

Figure 5.20: Case Study 2- Main bearing temperature, power produced, rotational speed of the rotor, SCADA records between 11th and 30th November

In this case study, the SCADA dataset was split as follows: the first nine months were used for training, the following three months for validation, and the remaining four months for testing, as shown in Figure 5.21. In contrast to Case Study 1, Case Study 2 utilizes a separate time period before the failure for validation, where the performance of the NBM is assessed. The reason for distinguishing the validation and test sets is run into failure data in Case Study 2. Assessing NBM performance using a test set describes model performance during unhealthy behavior of the component and can not be used to assess the adequacy of the established NBM. On the other hand, utilizing a separate validation set allows the accuracy of the build NBM to be assessed during healthy operation.

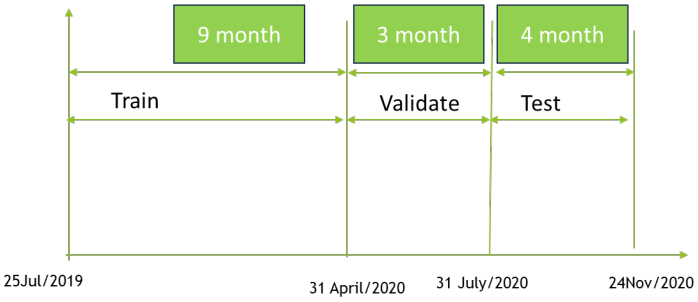

Figure 5.21: Case Study 2 - Data splitting

Monotonicity metric of the degradation trend

The value of the MK τ monotonicity metric changes significantly depending on the period considered for the analysis. The failed component is expected to exhibit a degradation trend from the beginning of the unhealthy behavior until failure. Thus, it is essential to analyze the monotonicity of the HIs when anomalous behavior is observed in the component. However, the dataset does not have status codes or maintenance warnings, making it difficult to determine when the unhealthy behavior of the main bearing began.

To determine the appropriate period for performing the monotonicity calculation, the main bearing temperature measurements were analyzed. Figure 5.22 illustrates the probability density function of the main bearing temperature for each month of the test set. The comparison of these distributions shows a shift towards higher temperature values from August to September. This shift is taken as an indication of the start of abnormal behavior. Figure 5.22 shows a gradual increase in the monthly main bearing temperature from September to November. An increase in the mean value of the main bearing temperature indicates the progression in the degradation of the component. The month of November is characterized by a shift of the temperature distribution towards higher values, which is attributed to the incipient failure. Thus, the MK τ for the compared HIs is calculated for the period between September and November.

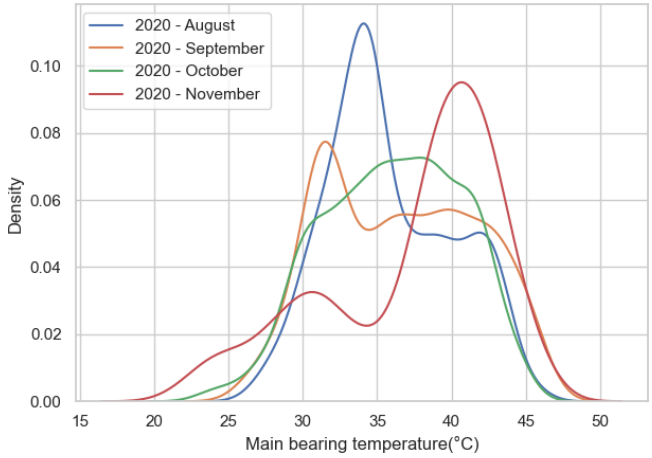

Figure 5.22: Case Study 2, Test set - Monthly probability density distributions of the main bearing temperature

Data cleaning

The steps followed for data cleaning are similar to those described in Case Study 1. Table 5.6 shows the number of data points in the original dataset and how many are dropped after each step of the cleaning process. Duplicate timestamps were dropped, and outliers were filtered, as done in Case Study 1. Records till the failure date (24th November) were selected.

Table 5.6: Case study 2 - Data cleaning process

	Number of data points
Data available	144719
Duplicate timestamps dropped	73568
Outliers dropped	36
Data cleaned	71115
Data till failure	70250

The records that were available after data cleaning were divided into training, validation, and testing, as illustrated in Figure 5.21. The amount of data available for training, validation, and testing is shown in Table 5.7. Notably, even though 16158 samples are available in the test set, a significant reduction in the number of samples can be observed (1866). This reduction is due to the lack of STD values for the input variables used in the main bearing temperature model (Equation (4.4)), which are essential to perform Monte Carlo simulation. To ensure a fair comparison of the methods, only 11.4% of the test set is used to perform the comparison of the HIs.

Table 5.7: Case study 2 - Data splitting

Data till failure	70250
Data used for training	40320
Data used for validation	13772
Data available for testing	16158
Data used for testing due to lack of STD values	1866

To prove the feasibility of only using 11.4% of the testing set, it is essential to show that the selected samples capture the main bearing temperature behavior. Figure 5.23 shows the daily amount of samples throughout the test set. The blue line shows the amount of data available each day in the test set, whereas the red line represents the daily amount of data after the samples lacking STD values were filtered.

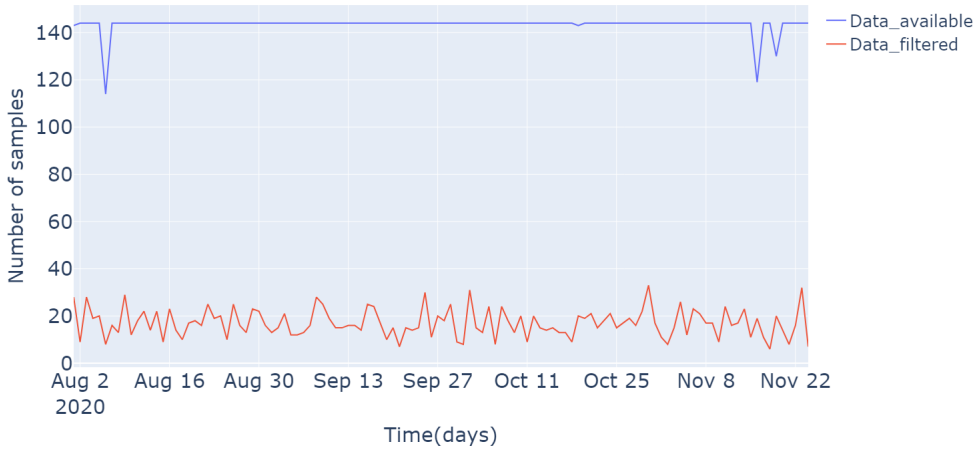

Figure 5.23: Case Study 2, Test set - Daily amount of available samples vs filtered samples

The blue graph illustrates around 144 records, with minor fluctuations. The SCADA system's 10-minute averaging interval generates six records per hour and a total of 144 data points per day. In contrast, the amount of records after applying filtering (red line) is significantly lower and fluctuates, averaging around 14 samples per day, which corresponds to about 2 hours of records per day.

Figure 5.24 illustrates the daily average of the generated power. The blue line represents the average power obtained, whereas the red line shows the average power calculated using only the data remaining after filtering.

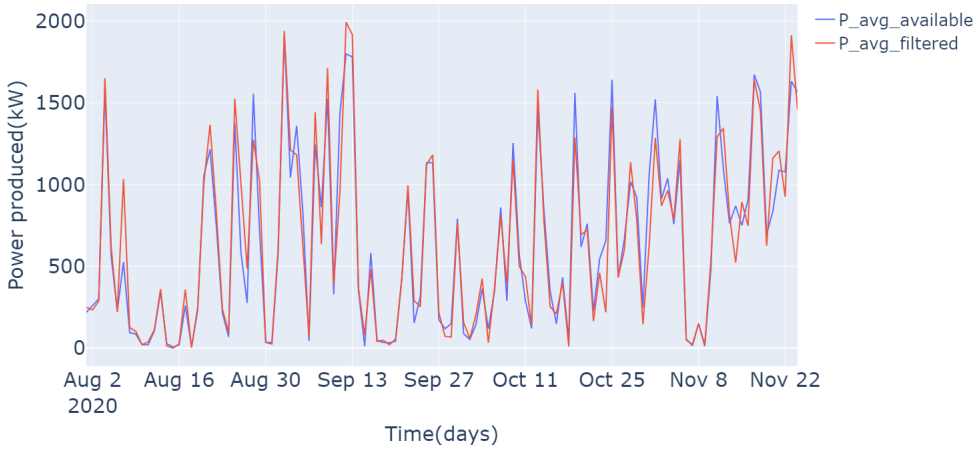

Figure 5.24: Case Study 2, Test set - Daily average power of available samples vs filtered samples

From Figure 5.24, it is possible to observe that, even though the amount of samples remaining after filtering is significantly lower, they still capture the behavior of the daily average power produced by the turbine. Thus, it is concluded that since the filtered samples capture the behavior of the main bearing power, the assumption that they represent the behavior of the main bearing temperature is valid. Finally, the filtered data (11.4%) can be used to perform the analysis in this case study.

Additionally, a lower accuracy in the temperature records of the SCADA data for Case Study 2 should be pointed out when comparing them to Case Study 1. In fact, in Case Study 1, the temperature records were recorded every 10 minutes. In contrast, in Case Study 2, the actual temperature was recorded in irregular patterns, and the gaps in records were filled in with the rounded-up number of the last measured record. This is true only for temperature records. All other measurements, such as power and rotational speed, have been recorded every 10 minutes, as in Case Study 1.

Nacelle temperature

The nacelle temperature is one of the inputs for modeling the main bearing temperature in Equation (4.4). However, the dataset used in Case Study 2 does not include these temperature records. Consequently, an alternative substitution for the nacelle temperature needs to be defined.

The main bearing and ambient temperatures for the entire dataset are shown in Figure 5.25, which shows a low cross-correlation between the two signals. For instance, the main bearing temperature cross-correlation with ambient temperature is 0.2 in Case Study 2, while in Case Study 1, the value is 0.78. This low cross-correlation could be a consequence of the cooling system present in the nacelle. The potential presence of the cooling system in the nacelle does not allow a linear correlation assumption of the relationship between the nacelle temperature and the ambient temperature. Therefore, Equation (5.1) with the exponential term was chosen as a substitution for the nacelle temperature in Equation (4.4) instead of replacing the nacelle temperature by ambient temperature.

$$\hat{T}_{\text{nacelle}}(t) = \beta_2 T_{\text{ambient}}^{\beta_5}(t) + \beta_6 \tag{5.1}$$

The equation used to model the main bearing temperature for Case Study 2 can be obtained by substituting Equation (5.1) into Equation (4.4), shown as:

$$\hat{T}_{\text{bear}}(t) \approx \beta_1 T_{\text{bear}}(t-1) + \beta_2 T_{\text{ambient}}^{\beta_5}(t) + \beta_3 \omega^2(t) + \beta_4 P(t) + \beta_6 \tag{5.2}$$

Notably, due to the exponential term in the adjusted main bearing temperature model, Case Study 2 utilizes multivariate regression using non-linear least squares described in Appendix A.5, to obtain coefficients of Equation (5.2).

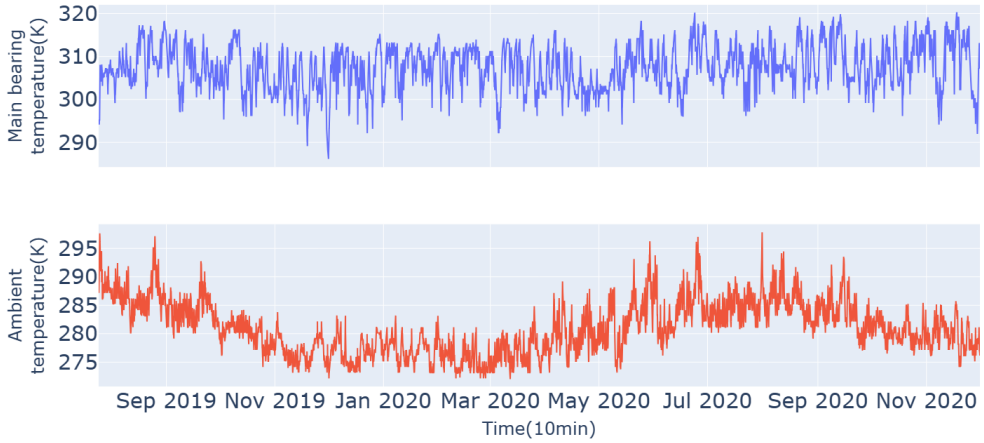

Figure 5.25: Case Study 2 - Measured main bearing and ambient temperatures

5.2.2. Adapted methodology

In this section, the adjustments made in the methodology will be discussed. The adopted baseline approach is shown in Figure 5.26, and the methodology used to obtain the proposed HI is illustrated in Figure 5.27. Notably, due to the failure of the main bearing in this case study, the EWMA smoothing step is implemented, as shown in Section 4.11. Moreover, the proposed method does not include step S due to the shorter time span of the available data compared to Case Study 1. Table 5.8 presents the nomenclature of the compared HIs. Similar to Case Study 1, the residual-based HI calculated using Step M is also analyzed in the results section and obtained according to the flowchart shown in Figure 5.28.

Table 5.8: Case Study 2 - Nomenclature of the HIs calculated with the baseline approach and after the implementation of each step of the proposed methodology

Method	HI	Flowchart
Baseline	$HI'_{Res\_Baseline}$	Figure (5.26)
Step M	HI'_{Res_M}	Figure (5.28)
Step M density of threshold region	HI'_{Alt}	Figure (5.27)

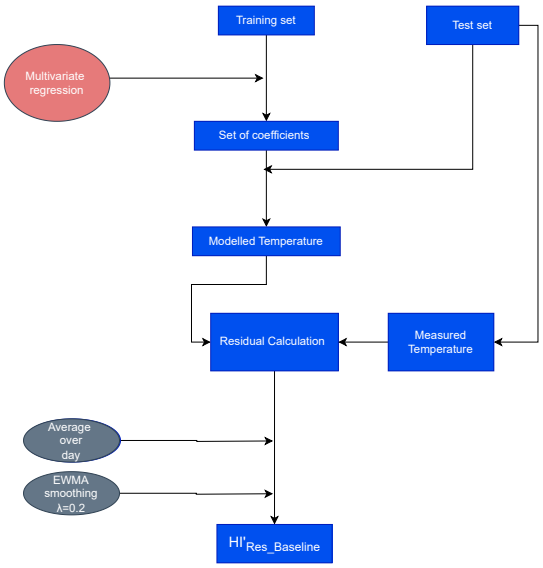

Figure 5.26: Case Study 2 - Baseline method to calculate $HI'_{Res\_Baseline}$

According to the flowchart shown in Figure 5.26, Equation (5.2) is fitted to the training set to obtain the coefficients of the main bearing temperature model. These coefficients are used to model the main bearing temperature in the test set, and the residuals are calculated and averaged daily. In contrast to Case Study 1, the additional step of the EWMA step is applied to smooth the obtained HI, as described in Section 4.3.3, to obtain $HI'_{Res\_Baseline}$.

For Case Study 2, EWMA smoothing with a factor λ=0.2 is the final post-processing step to obtain all the HIs shown in Table 5.8, 5.28). It is important to remember that any λ factor can be chosen as long as it is the same for the compared HIs. Various smoothing factors λ applied to obtain HIs presented in Table 5.8 are shown in Appendix A.6. In this case study, a strong smoothing coefficient (λ=0.2) was chosen due to the significant fluctuations observed in the HIs. High fluctuations in HIs are primarily attributed to the limited amount of data left after the cleaning process.

The method proposed in this work is shown in Figure 5.27. Notably, compared to the methodology proposed in Case Study 1, it does not include Step S. Case Study 2 dataset covers only 16 months, with each season represented only once. This limits the possibility of drawing conclusions on the possible seasonal behavior of the HI. In contrast, in Case Study 1, five years of data for each season were available. For example, to develop a separate main bearing temperature model for July, the training dataset spanning from 2013 up to 2018 had 5 months of July available. The amount of data available in Case Study 1 can be considered sufficient to capture the normal behavior of the main bearing temperature for the specific month (Chapter 5.1.5).

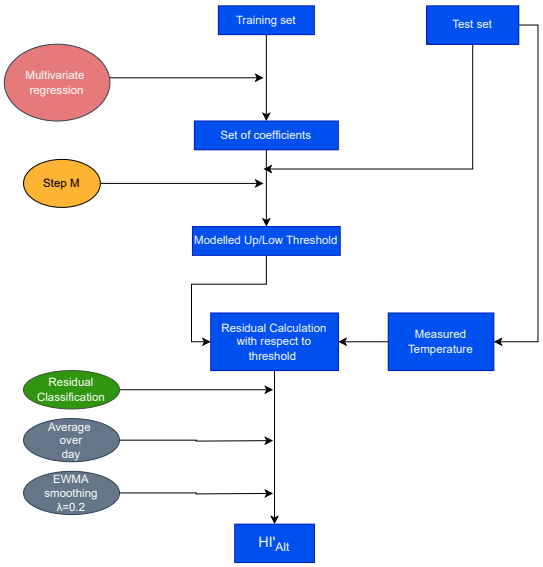

Figure 5.27: Case Study 2 - Proposed method, implementation of step M density of threshold region to calculate HI'_{Alt}

According to the flowchart shown in Figure 5.27, the proposed method implements step M. As in Case Study 1, the coefficients are used to apply Step M and obtain the upper and lower temperature thresholds of each timestamp in the test set. Next, the residuals are calculated as described in Section 4.3.2.1 and classified as shown in Equation (4.16). Subsequently, the average over a day step is applied to obtain the daily density of the threshold region. Finally, EWMA smoothing with λ=0.2 factor is applied to obtain HI'_{Alt}. The results section also analyses the intermediate steps of the proposed method shown in Figure 5.27. To obtain residual-based HI (HI'_{Res_M}) using Step M, the method shown in Figure 5.28 applies the same steps as in Figure 5.27 except for the residual classification.

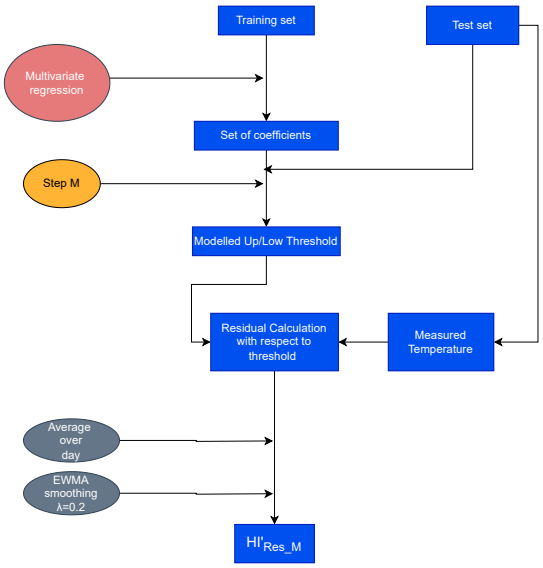

Figure 5.28: Case Study 2 - Implementation of Step M to calculate HI'_{Res_M}

For Case Study 2, the remainder of this Section is structured as follows. Section 5.2.3 focuses on $HI'_{Res\_Baseline}$ obtained using the adopted baseline approach. Section 5.2.4.1 presents HI'_{Res_M} obtained using Step M. Section 5.2.4.2 explores HI'_{Alt} based on the density of the threshold region obtained using Step M.

5.2.3. Baseline approach

This section first presents the main bearing temperature baseline model coefficients for Equation (5.2). Then, these coefficients are used to assess the performance of the NBM in the validation set. Finally, $HI'_{Res\_Baseline}$ obtained as shown in Figure 5.26 is presented.

Multivariate regression is applied to the training set to obtain the model coefficients shown in Table 5.9. As in Case Study 1, the coefficient β_1 associated with the main bearing temperature at the previous timestamp is the most significant compared to the other coefficients. In Case Study 2, the coefficient β_4, corresponding to the term associated with the power signal, is negligible (5.584e-37≈0). According to Cambron et al. [32], this coefficient represents the heating of the main bearing due to the Joule effect of the generator. The low precision in temperature records can be the reason for the insignificant effect of the power term on the main bearing temperature for this case study.

Table 5.9: Case Study 2 - Main bearing temperature model coefficients of Equation (5.2)

Coefficients	Case Study 2
β_1	0.967
β_2	0.679
$\beta_3(K * s^2/rad^2)$	0.178
$\beta_4(K/kW)$	5.584e-37
β_5	0.471
$\beta_6(K)$	0.21

These coefficients are then used to model the main bearing temperature for the validation set. Figure 5.29 shows the modeled and measured main bearing temperature for the validation set. A zoom-in view between the 5th and 9th of June 2020 is provided in Figure 5.30 to clearly illustrate the two temperatures. Notably, the time series of the temperature records resemble a step function. This is due to the lower accuracy of the data recording observed in Case Study 2 compared to Case Study 1, as discussed earlier.

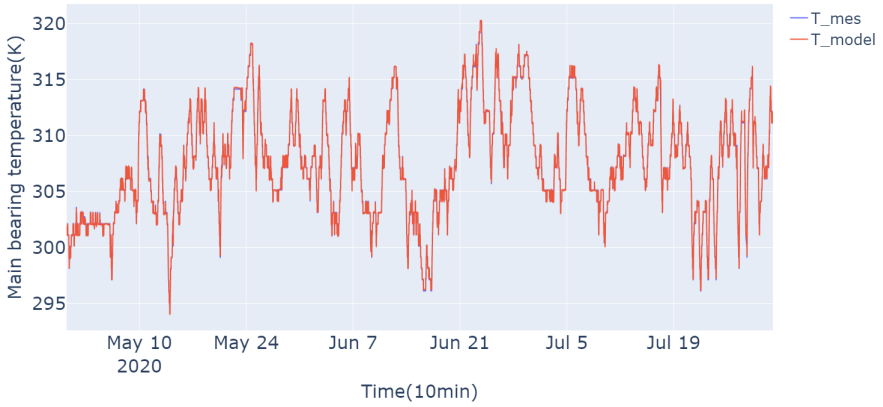

Figure 5.29: Case Study 2, Validation set - Modelled and measured main bearing temperature

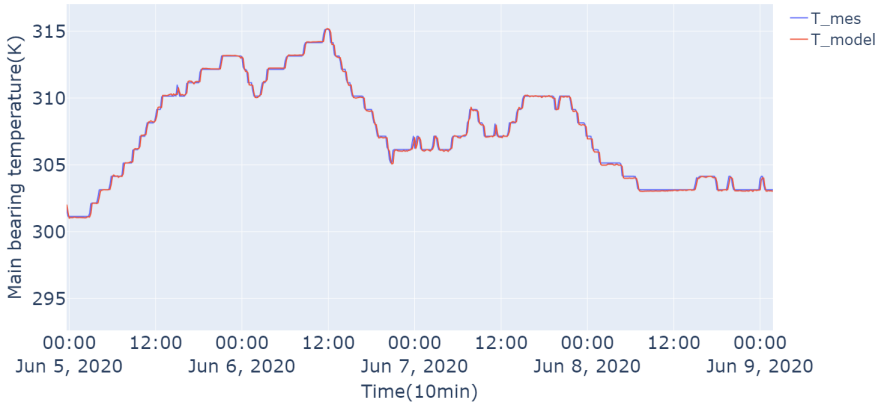

Figure 5.30: Case Study 2, Validation set - Modelled and measured main bearing temperature, zoom-in view in the period between June 5 and June 9, 2020

Table 5.10 shows the performance metrics of the baseline NBM for the validation set and its comparison with the previous case study. The baseline model is characterized by significantly lower performance than in Case Study 1. The lower performance of fit is attributed to the lower precision of the temperature records shown in Figure 5.30. Although the performance of the baseline NBM is lower than in the previous case study, according to Zhang et al. [59], the obtained RMSE value of 0.234 is still considered acceptable for condition monitoring purposes.

Table 5.10: Case Study 2 and Case Study 1 performance metrics of the baseline models

Metric	**Case Study 2** $Model_{Baseline}$	**Case Study 1** $Model_{Baseline}$
RMSE (K)	0.234	0.124
R^2	0.997	0.9995
MAE (K)	0.151	0.0777
MAPE (%)	0.44	0.32

Figure 5.31 shows the behavior of $HI'_{Res\_Baseline}$ for the test set calculated using the approach described in Figure 5.26. Significant fluctuations of $HI'_{Res\_Baseline}$ can be observed in Figure 5.31. Moreover, from the 27th of September till the failure date, a significant upward trend is evident, with $HI'_{Res\_Baseline}$ reaching a value of 0.153K at the 24th of November.

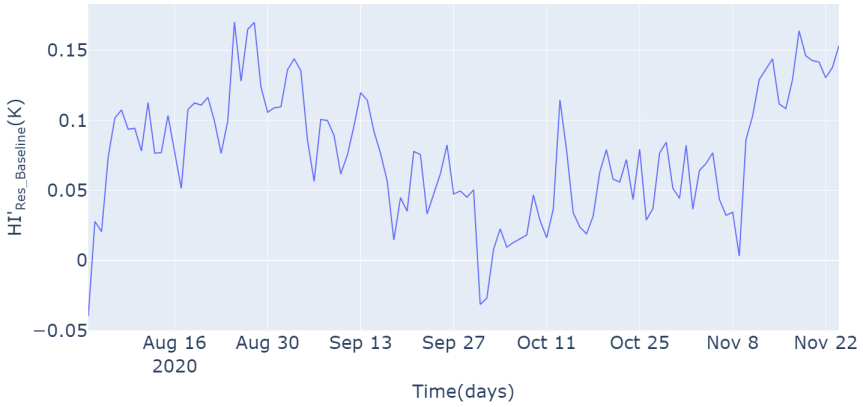

Figure 5.31: Case Study 2, Test set - Baseline approach HI, $HI'_{Res\_Baseline}$

5.2.4. Step M

The regression coefficients shown in Table 5.9 are used to apply Step M for the test set and yield upper and lower thresholds for each timestamp. Residuals are calculated with respect to the thresholds obtained as described in Section 4.3.2.1. Notably, 32.3% of the measured mean bearing temperature fell within the upper and lower threshold region where the residuals are assumed to be equal to 0 (Equation (4.12)). This section first presents the results for the residual-based HI (HI'_{Res_M}), and next, it focuses on the HI based on the density of the threshold region (HI'_{Alt}).

Step M, HI based on residual

HI'_{Res_M} has been obtained according to the method shown in Figure 5.28. Figure 5.32 illustrates HI'_{Res_M} for the test set. The y-axis shows that the magnitude of HI'_{Res_M} fluctuations is less than $HI'_{Res\_Baseline}$. HI'_{Res_M} also illustrates a strong upward trend from the 27th of September, with HI reaching a value of 0.088K on the 24th of November. As in Case Study 1, the HIs are compared in terms of monotonicity and dispersion. Figures 5.33, 5.34, and 5.35 compare $HI'_{Res\_Baseline}$ and HI'_{Res_M} using MK τ, MSE, and the Noise metrics, respectively.

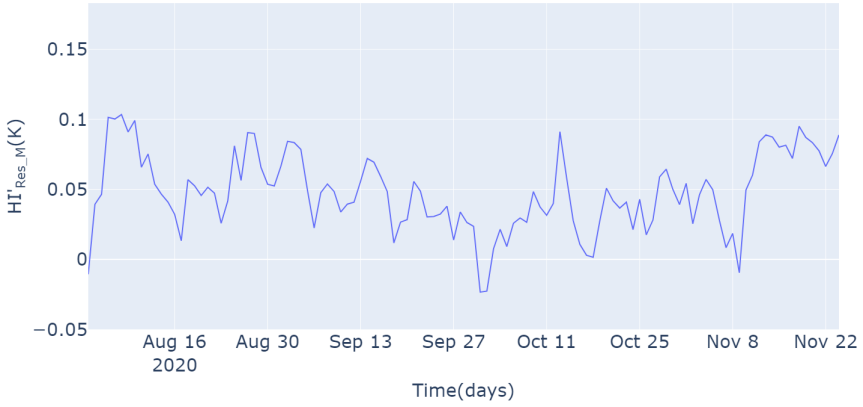

Figure 5.32: Case Study 2, Test set - Step M HI, HI'_{Res_M}

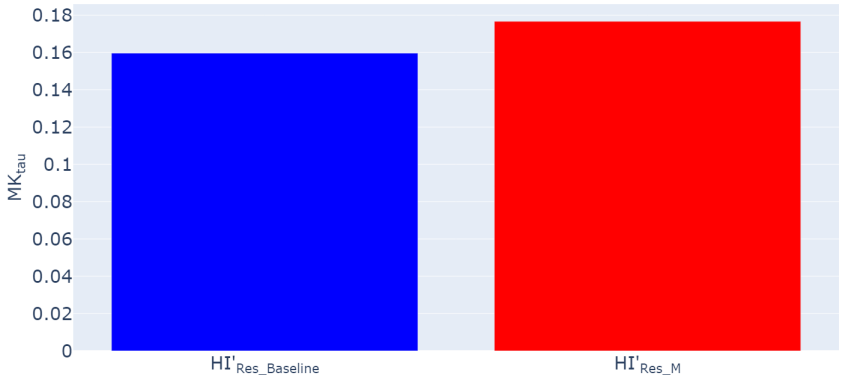

Figure 5.33: Case Study 2 - $HI'_{Res\_Baseline}$ and HI'_{Res_M} monotonicity comparison using MK τ

Figure 5.33 shows that with MK τ =0.17 HI'_{Res_M} is more monotonic than $HI'_{Res\_Baseline}$ with MK τ =0.15. The improvement in monotonicity is about 13%. The low magnitude of the monotonicity metric for both HIs is attributed to fluctuations of the HIs and the apparent strong upward trend present in both HI'_{Res_M} and $HI'_{Res\_Baseline}$ only after the 27th of September as shown in Figures 5.31 and 5.32.

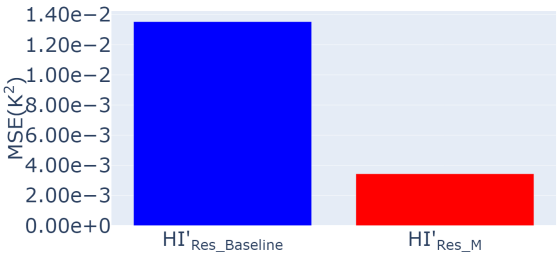

Figure 5.34: Case Study 2 - $HI'_{Res\_Baseline}$ and HI'_{Res_M} dispersion comparison using MSE

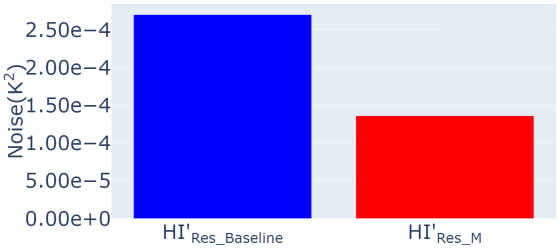

Figure 5.35: Case Study 2 - $HI'_{Res\_Baseline}$ and HI'_{Res_M} dispersion comparison using Noise

Figure 5.34 shows that HI'_{Res_M} has a lower MSE (3.43e-3K^2) than $HI'_{Res\_Baseline}$ (1.35e-2K^2). A similar trend is observed when looking at the dispersion of the HIs using the Noise metric. Figure 5.35 illustrates that HI'_{Res_M} has a lower value of Noise compared to $HI'_{Res\_Baseline}$ ((1.36e-4K^2 vs. 2.70e-4K^2). The CEEMDAN decomposition to calculate the Noise values of the compared HIs is shown in Appendix A.4.2.1.

From the comparison of these metrics, it can be concluded that while the introduction of HI'_{Res_M} does not provide substantial improvements in monotonicity compared to $HI'_{Res\_Baseline}$, it contributes significantly to the reduction in dispersion. Improvements in dispersion metrics were also observed in the same step when analyzing Case Study 1 in Section 5.1.6.1. Thus, it can be concluded that the residual calculation with respect to thresholds effectively reduces the dispersion of the HI.

Step M, HI based on the density of the threshold region

Following the method illustrated in Figure 5.27, HI'_{Alt} based on the density of the threshold region was calculated for the test set, and it is shown in Figure 5.36. Notably, Figure 5.36 illustrates a clear monotonic downward trend from the end of August. As the component approaches the failure, the daily density of the threshold region gradually reduces, indicating the health deterioration of the component. Moreover, HI'_{Alt} reached its lowest value of 0.19 on the 22nd of November, just before the occurrence of the failure.

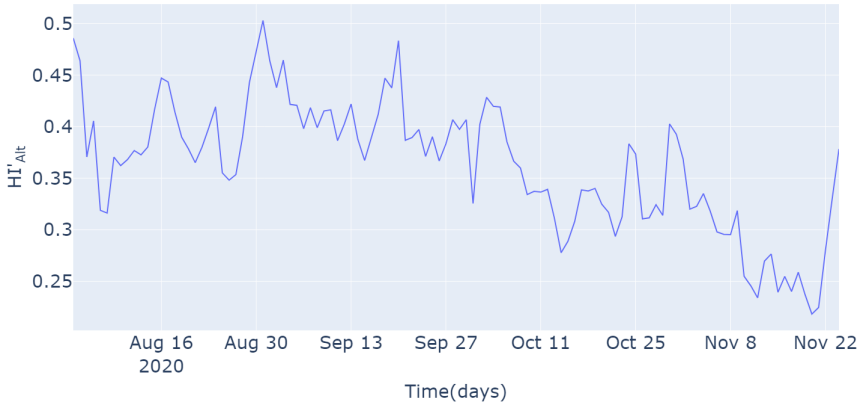

Figure 5.36: Case Study 2, Test set - Step M density of threshold region HI, HI'_{Alt}

Similar to the previous section, HI'_{Alt} and $HI'_{Res\_Baseline}$ are compared using MK τ, MSE, Noise metrics as shown in Figures 5.37, 5.38, and 5.39, respectively. Since the unit of $HI'_{Res\_Baseline}$ is K and the density of the threshold region is adimensional, $HI'_{Res\_Baseline}$ and HI'_{Alt} are first normalized using Equation (4.18).

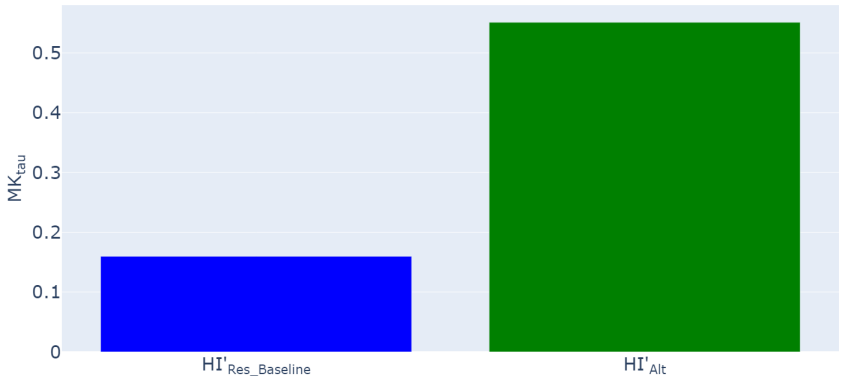

Figure 5.37: Case Study 2 - $HI'_{Res\_Baseline}$ and HI'_{Alt} monotonicity comparison using MK τ

Figure 5.37 shows that with MK τ= 0.55 HI'_{Alt} is significantly more monotonic than $HI'_{Res\_Baseline}$ with MK τ=0.15. Figure 5.38 shows that HI'_{Alt} is less dispersed compared to $HI'_{Res\_Baseline}$ (4.40 vs 6.72). Similarly, Figure 5.39 illustrates HI'_{Alt} (0.093) has a lower value of Noise compared to $HI'_{Res\_Baseline}$ (0.136). The CEEMDAN decomposition to obtain the Noise values of the compared HIs is shown in Appendix A.4.2.2.

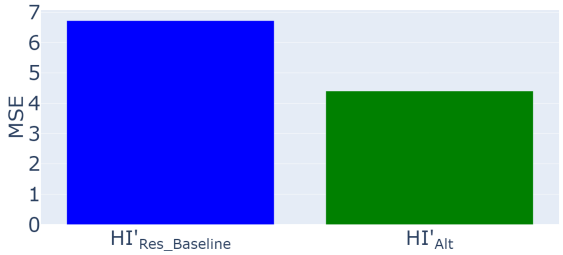

Figure 5.38: Case Study 2 - $HI'_{Res\_Baseline}$ and HI'_{Alt} dispersion comparison using MSE

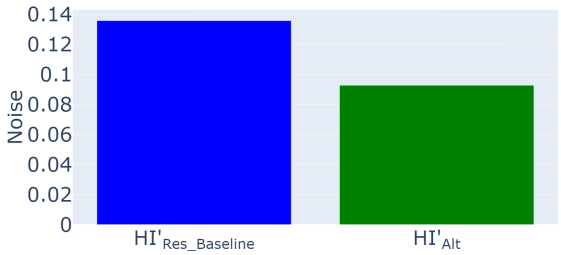

Figure 5.39: Case Study 2 - $HI'_{Res\_Baseline}$ and HI'_{Alt} dispersion comparison using Noise

The results of Case Study 2 show that the HI'_{Alt} is significantly more monotonic and less dispersed compared to what is achieved with $HI'_{Res\_Baseline}$. According to improved monotonicity and dispersion metrics, HI'_{Alt} enables more accurate monitoring of the degradation trend compared to $HI'_{Res\_Baseline}$. Furthermore, the proposed HI'_{Alt} exhibits an evident downward trend starting almost 1 month before what is shown by $HI'_{Res\_Baseline}$ in the baseline approach.

6

Conclusions & Recommendations

This thesis proposed a physics-based NBM using SCADA data to build an HI for wind turbine main bearing degradation trend monitoring. The proposed approach aimed at increasing the monotonicity and reducing the dispersion of the developed HI to enable more accurate degradation trend monitoring. To achieve this aim, seasonal variations and variability of the wind field characteristics were considered in physics-based NBM of the main bearing temperature (Section 4.3). The results of the proposed approach were compared against those of a baseline method adopted from Cambron et al. [32]. Two case studies were conducted. In Case Study 1, the absence of available failure data for the main bearing component was identified as a limiting factor, resulting in the lack of significant improvements in HI obtained using the proposed approach. However, the results for Case Study 2, where failure data was available, demonstrated the ability of the proposed approach to build an HI with higher monotonicity and reduced dispersion in the degradation trend compared to the baseline approach. This chapter first answers the research questions introduced in Chapter 1. Next, it outlines recommendations for future work based on the challenges encountered throughout the analysis.

6.1. Research question discussion

Research question

How can physics-based NBM be used for the degradation trend monitoring of the wind turbine main bearing?

SCADA-based NBM methods analyze the difference between the modeled and measured main bearing temperatures to perform fault detection. The underlying detection principle is based on the progressive health deterioration of the component, causing the field measurements to deviate from the NBM outputs. Available methods consider the increase in the residuals above a defined threshold as an indication of failure. This thesis utilizes physics-based NBM residuals to build HI to monitor the health deterioration of the component. The gradual change in the HI is analyzed to assess the progress of the degradation in the main bearing component, where the trend in the HI is expected to become more evident as the component health deteriorates.

Research question

How can the current physics-based NBM's limitations be effectively overcome when using SCADA data?

Physics-based NBM methods require case-specific knowledge, such as size and material properties, to employ equations capturing the healthy behavior of the component. Using SCADA data allows to overcome these limitations. Historical SCADA data is used to fit a physics-based model and determine its parameters. These obtained parameters are subsequently applied to the test set to model the main bearing temperature. Moreover, the widespread adoption of SCADA systems enables the extensive application of physics-based NBM methods.

Research question

What metrics should be utilized to evaluate the effectiveness of the proposed method?

Monotonicity and dispersion metrics were used to evaluate the effectiveness of the method proposed to monitor degradation trends. The degradation trend is expected to be monotonic due to the irreversible nature of the health deterioration process (Section 4.2.1). This thesis applied the MK τ metric to measure the monotonicity of the HI (Section 3.3.1). Dispersed HI behavior reduces the accuracy of fitted degradation models, leading to less accurate RUL predictions. The dispersion of the HIs was measured using MSE and Noise metrics (Section 4.2.2).

Research question

How can seasonal variations be taken into account when developing a physics-based NBM for the degradation trend monitoring of the wind turbine main bearing? And what are the benefits?

The proposed method introduced step S to consider seasonal variations when applying the physics-based NBM (Section 4.3.1). Step S is proposed to prevent the misinterpretation of seasonal patterns as degradation trends, ensuring more accurate degradation trend monitoring (Section 4.2.3). The proposed step applies multivariate regression to derive distinct sets of coefficients of Equation (4.4) corresponding to the time periods of the year. In Case Study 1, 12 sets of equation coefficients were used to model independently the behavior of the main bearing temperature during each month of the year. The effectiveness of the proposed step was measured using cross-correlation of the obtained HI with the ambient temperature. The proposed step effectively reduced seasonality by more than 50% without compromising the model's fit to the test data (Section 5.1.5).

Research question

How can variability of wind field characteristics be taken into account when developing physics-based NBM for the degradation trend monitoring of the wind turbine main bearing? And what are the benefits?

The primary reason for the premature failure of wind turbine components is attributed to the variability of the wind conditions. However, current NBM methods are based solely on the mean value records and do not consider the variations within the 10-minute time frame. The proposed method introduced step M, which applies the Monte Carlo simulation using SCADA data mean and STD records to consider variability in the main bearing operation within the 10-minute interval. Step M models the main bearing temperature during 10 minutes as a range of possible values, introducing upper and lower thresholds for each modeled timestamp. A defined threshold region is assumed to represent the healthy operating region during a 10-minute time frame. The proposed approach of calculating residuals with respect to the obtained threshold values successfully reduces the dispersion of the HI (Sections 5.1.6.1, 5.2.4.1).

The threshold region obtained from the Monte Carlo simulation allows the introduction of the density of the threshold region as a novel HI to monitor the degradation trend of the component. The density of the threshold region represents the amount of points in the threshold region during a specified time frame. Gradual reduction of the density of the threshold region indicates health deterioration of the component. In Case Study 1, the proposed HI did not improve dispersion and monotonicity metrics due to the fault-free dataset (Section 5.1.6.2). However, in Case Study 2, containing failure data of the main bearing, the proposed HI showed significantly higher monotonicity and lower dispersion than the baseline HI (Section 5.2.4.2). Notably, the proposed HI demonstrated an evident degradation trend one month in advance than the baseline HI. An early indication of health deterioration can be used to trigger the lifetime prognosis of the main bearing and plan the maintenance of the component.

6.2. Recommendations

This section outlines recommendations for future research. Firstly, this section discusses the essential factors required for the implementation of the proposed approach. Subsequently, this section presents some recommendations for further investigation.

A limitation of the proposed method, when compared to the baseline, is its requirement for twice as many parameters, as for each parameter of the main bearing temperature model (Equation (4.4)), both mean and STD values are needed. Consequently, the quality of data becomes even more significant since step M cannot be executed unless the dataset includes STD values. For instance, in the second case study, there was a notable reduction in the data available for analysis due to the lack of STD records (Table 5.7).

Similar to any data analysis method, incorporating more case studies would be advantageous in demonstrating the benefits of the proposed method. Nonetheless, there are specific aspects that are recommended for investigation, provided that more than one failure case is available.

- Building upon the findings of this thesis, the next step should involve extending the proposed methodology to incorporate the lifetime prognosis step. The suggested framework would involve projecting the obtained degradation trend into the future to estimate the RUL of the component.
- Increasing the number of case studies with failures could help refine model parameters, like seasonality divisions, k threshold value for the width of the threshold region, averaging over interval value, and EWMA λ value.
- While this thesis primarily focused on enhancing the quality of the HI for degradation trend monitoring, the inclusion of additional case studies would facilitate an assessment of the capabilities of the proposed method to perform fault detection. For instance, implementing a framework where residual-based HIs are used for fault detection while the density of threshold region is used for subsequent RUL prediction.
- It also would be interesting to explore binning to consider variable operating conditions when performing the post-processing. The binning of NBM residuals based on rotational speed was explored in Section A.22.

Bibliography

[1] Ángel Encalada-Dávila et al. “Wind turbine main bearing fault prognosis based solely on scada data”. In: *Sensors* 21.6 (Mar. 2021). DOI: 10.3390/s21062228.

[2] International Renewable Energy Agency. *RENEWABLE POWER GENERATION COSTS IN 2022 2 R E N E WAB LE P OWE R G E N E R ATI O N COS TS I N 202 2*. 2023. URL: www.irena.org.

[3] “GWEC-2023_interactive”. In: ().

[4] Roman Zaiets. *RENEWABLES 2023 GLOBAL STATUS REPORT ENERGY SUPPLY COLLECTION*. Tech. rep. 2023.

[5] A. Elia et al. “Wind turbine cost reduction: A detailed bottom-up analysis of innovation drivers”. In: *Energy Policy* 147 (Dec. 2020). DOI: 10.1016/j.enpol.2020.111912.

[6] Jan Helsen. *Review of Research on Condition Monitoring for Improved O&M of Offshore Wind Turbine Drivetrains*. June 2021. DOI: 10.1007/s40857-021-00237-2.

[7] *Wind power capacity in the Net Zero Scenario, 2010-2030 –Charts – Data & Statistics - IEA*. URL: https://www.iea.org/data-and-statistics/charts/wind-power-capacity-in-the-net-zero-scenario-2010-2030.

[8] Wenxian Yang et al. “Wind turbine condition monitoring by the approach of SCADA data analysis”. In: *Renewable Energy* 53 (May 2013), pp. 365–376. DOI: 10.1016/j.renene.2012.11.030.

[9] Søren Krohn et al. *The Economics of Wind Energy A report by the European Wind Energy Association*. Tech. rep. URL: www.inextremis.be.

[10] Eva Topham et al. “Recycling offshore wind farms at decommissioning stage”. In: *Energy Policy* 129 (June 2019), pp. 698–709. DOI: 10.1016/j.enpol.2019.01.072.

[11] Estefania Artigao et al. *Wind turbine reliability: A comprehensive review towards effective condition monitoring development*. Oct. 2018. DOI: 10.1016/j.apenergy.2018.07.037.

[12] Yalcin Dalgic et al. “Advanced logistics planning for offshore wind farm operation and maintenance activities”. In: *Ocean Engineering* 101 (June 2015), pp. 211–226. DOI: 10.1016/j.oceaneng.2015.04.040.

[13] M. El-Naggar et al. “Optimal maintenance strategy of wind turbine subassemblies to improve the overall availability”. In: *Ain Shams Engineering Journal* 14.10 (Oct. 2023). DOI: 10.1016/j.asej.2023.102177.

[14] Nam-Ho Kim Dawn An Joo-Ho Choi. *Prognostics and Health Management of Engineering Systems*. Tech. rep.

[15] Ehsan Taheri et al. “Survey of prognostics methods for condition-based maintenance in engineering systems”. In: (Dec. 2019). URL: http://arxiv.org/abs/1912.02708.

[16] Gustavo de Novaes Pires Leite et al. *Prognostic techniques applied to maintenance of wind turbines: a concise and specific review*. Jan. 2018. DOI: 10.1016/j.rser.2017.06.002.

[17] Hamed Badihi et al. “A Comprehensive Review on Signal-Based and Model-Based Condition Monitoring of Wind Turbines: Fault Diagnosis and Lifetime Prognosis”. In: *Proceedings of the IEEE* 110.6 (June 2022), pp. 754–806. DOI: 10.1109/JPROC.2022.3171691.

[18] Ravi Pandit et al. *SCADA data for wind turbine data-driven condition/performance monitoring: A review on state-of-art, challenges and future trends*. Apr. 2022. DOI: 10.1177/0309524X221124031.

[19] Xiao Sheng Si et al. *Remaining useful life estimation - A review on the statistical data driven approaches*. Aug. 2011. DOI: 10.1016/j.ejor.2010.11.018.

[20] Yanhui Feng et al. *Use of SCADA and CMS signals for failure detection & diagnosis of a wind turbine gearbox USE OF SCADA AND CMS SIGNALS FOR FAILURE DETECTION AND DIAGNOSIS OF A WIND TURBINE GEARBOX*. Tech. rep. URL: https://www.researchgate.net/publication/267787845.

[21] Prashant H. Jain et al. "A Review on Vibration Signal Analysis Techniques Used for Detection of Rolling Element Bearing Defects". In: *International Journal of Mechanical Engineering* 8.1 (Jan. 2021), pp. 14–29. DOI: 10.14445/23488360/ijme-v8i1p103.

[22] Milad Rezamand et al. *Critical Wind Turbine Components Prognostics: A Comprehensive Review*. Dec. 2020. DOI: 10.1109/TIM.2020.3030165.

[23] Basheer Wasef Shaheen et al. "Performance Monitoring of Wind Turbines Gearbox Utilising Artificial Neural Networks — Steps toward Successful Implementation of Predictive Maintenance Strategy". In: *Processes* 11.1 (Jan. 2023). DOI: 10.3390/pr11010269.

[24] Alexis Lebranchu et al. "Using SCADA data for fault detection in wind turbines: Local internal model versus distance to a wind farm reference". In: *Applied Condition Monitoring*. Vol. 4. Springer, 2016, pp. 225–236. DOI: 10.1007/978-3-319-20463-5{_}17.

[25] Davide Astolfi et al. *FAULT PREVENTION AND DIAGNOSIS THROUGH SCADA TEMPERATURE DATA ANALYSIS OF AN ONSHORE WIND FARM*. Tech. rep. 2. 2014.

[26] Wenxian Yang et al. "Wind turbine condition monitoring: Technical and commercial challenges". In: *Wind Energy* 17.5 (2014), pp. 673–693. DOI: 10.1002/we.1508.

[27] Jannis Tautz-Weinert et al. *Using SCADA data for wind turbine condition monitoring - A review*. Mar. 2017. DOI: 10.1049/iet-rpg.2016.0248.

[28] K Kim et al. *Use of SCADA Data for Failure Detection in Wind Turbines*. Tech. rep. 2011. URL: http://www.osti.gov/bridge.

[29] Conor McKinnon et al. "Effect of time history on normal behaviour modelling using SCADA data to predict wind turbine failures". In: *Energies* 13.18 (Sept. 2020). DOI: 10.3390/en13184745.

[30] Michael Wilkinson et al. "Comparison of methods for wind turbine condition monitoring with SCADA data". In: *IET Renewable Power Generation* 8.4 (2014), pp. 390–397. DOI: 10.1049/iet-rpg.2013.0318.

[31] Xavier Chesterman et al. "Overview of normal behavior modeling approaches for SCADA-based wind turbine condition monitoring demonstrated on data from operational wind farms". In: *Wind Energy Science* 8.6 (June 2023), pp. 893–924. DOI: 10.5194/wes-8-893-2023.

[32] Philippe Cambron et al. "Bearing temperature monitoring of a Wind Turbine using physics-based model". In: *Journal of Quality in Maintenance Engineering* 23.4 (2017), pp. 479–488. DOI: 10.1108/JQME-06-2016-0028.

[33] A. B. Borchersen et al. "Model-based fault detection for generator cooling system in wind turbines using SCADA data". In: *Wind Energy* 19.4 (Apr. 2016), pp. 593–606. DOI: 10.1002/we.1852.

[34] Xiao-Sheng Si et al. *Springer Series in Reliability Engineering Stochastic Models, Methods and Applications Data-Driven Remaining Useful Life Prognosis Techniques*. Tech. rep. URL: http://www.springer.com/series/6917.

[35] Wanwan Zhang et al. "A review of failure prognostics for predictive maintenance of offshore wind turbines". In: *Journal of Physics: Conference Series* 2362.1 (Nov. 2022), p. 012043. DOI: 10.1088/1742-6596/2362/1/012043.

[36] *2020 Global Reliability and Prognostics and Health Management (PHM-Shanghai)*. IEEE, 2020.

[37] Yanan Chen et al. "Degradation-trend-dependent Remaining Useful Life Prediction for Bearing with BiLSTM and Attention Mechanism". In: *Proceedings of 2021 IEEE 10th Data Driven Control and*

Learning Systems Conference, DDCLS 2021. Institute of Electrical and Electronics Engineers Inc., May 2021, pp. 1177–1182. DOI: 10.1109/DDCLS52934.2021.9455600.

[38] Hatem M. Elattar et al. “Prognostics: a literature review”. In: *Complex & Intelligent Systems* 2.2 (June 2016), pp. 125–154. DOI: 10.1007/s40747-016-0019-3.

[39] Koceila Abid et al. “Adaptive data-driven approach for fault prognostics based on normal conditions-application to shaft bearings of wind turbine”. In: *Proceedings of the Annual Conference of the Prognostics and Health Management Society, PHM*. Vol. 11. 1. Prognostics and Health Management Society, Sept. 2019. DOI: 10.36001/phmconf.2019.v11i1.838.

[40] Shengwen Zhou et al. *Constructing a health indicator based on long short-term memory and using an extreme inflection point with a slope model to enhance monotonicity*. Mar. 2023. DOI: 10.1007/s40430-022-03968-z.

[41] Edward Hart. “Developing a systematic approach to the analysis of time-varying main bearing loads for wind turbines”. In: *Wind Energy* 23.12 (Dec. 2020), pp. 2150–2165. DOI: 10.1002/we.2549.

[42] Latha Sethuraman et al. “Main Bearing Dynamics in Three-Point Suspension Drivetrains for Wind Turbines; National Wind Technology Center (NWTC), NREL (National Renewable Energy Laboratory)”. In: (May 2015). URL: https://www.osti.gov/biblio/1215288.

[43] Mattia Beretta et al. “An ensemble learning solution for predicitive manintenance of wind turbines main bearing”. In: *Sensors* 21.4 (Feb. 2021), pp. 1–19. DOI: 10.3390/s21041512.

[44] Edward Hart et al. *A review of wind turbine main bearings: Design, operation, modelling, damage mechanisms and fault detection*. Jan. 2020. DOI: 10.5194/wes-5-105-2020.

[45] Yi Guo et al. “Investigation of main bearing operating conditions in a three-Point mount wind turbine drivetrain”. In: *Forschung im Ingenieurwesen/Engineering Research* 85.2 (June 2021), pp. 405–415. DOI: 10.1007/s10010-021-00477-8.

[46] Roger Bergua Archeli et al. *Up-Tower Investigation of Main Bearing Cage Slip and Loads*. Tech. rep. 2021. URL: www.nrel.gov/publications..

[47] Yunfeng Li et al. “Internal load distribution of single-row tapered roller bearings doubly supporting main shaft of wind turbine”. In: *Advances in Mechanical Engineering* 14.5 (May 2022). DOI: 10.1177/16878132221098895.

[48] Martin Cardaun et al. “Analysis of wind-turbine main bearing loads due to constant yaw misalignments over a 20 years timespan”. In: *Energies* 12.9 (May 2019). DOI: 10.3390/en12091768.

[49] Edward Hart et al. “Wind turbine main-bearing loading and wind field characteristics”. In: *Wind Energy* 22.11 (Nov. 2019), pp. 1534–1547. DOI: 10.1002/we.2386.

[50] Anil Dhanola et al. *Tribological challenges and advancements in wind turbine bearings: A review*. Dec. 2020. DOI: 10.1016/j.engfailanal.2020.104885.

[51] Junyan Ma et al. *Application of SCADA data in wind turbine fault detection – a review*. Jan. 2023. DOI: 10.1108/SR-06-2022-0255.

[52] Christian Tutivén et al. “Early Fault Diagnosis Strategy for WT Main Bearings Based on SCADA Data and One-Class SVM”. In: *Energies* 15.12 (June 2022). DOI: 10.3390/en15124381.

[53] Alessandro Murgia et al. “Discussion on the Suitability of SCADA-Based Condition Monitoring for Wind Turbine Fault Diagnosis through Temperature Data Analysis”. In: *Energies* 16.2 (Jan. 2023). DOI: 10.3390/en16020620.

[54] R. Peter et al. “Wind turbine generator prognostics using field SCADA data”. In: vol. 2265. 3. cited By 4. 2022. DOI: 10.1088/1742-6596/2265/3/032111. URL: https://www.scopus.com/inward/record.uri?eid=2-s2.0-85131824413&doi=10.1088%2f1742-6596%2f2265%2f3%2f032111&partnerID=40&md5=f91a9f75d20dc15e7c072a56a28af0d7.

[55] S. Wang et al. “Fault Diagnosis of Wind Turbine Generator with Stacked Noise Reduction Autoencoder Based on Group Normalization”. In: *Energy Engineering: Journal of the Association of Energy*

Engineering 119.6 (2022). cited By 0, pp. 2431–2445. DOI: 10.32604/ee.2022.020779. URL: https://www.scopus.com/inward/record.uri?eid=2-s2.0-85138269946&doi=10.32604%2fee.2022.020779&partnerID=40&md5=9fdb610b70dfcb6c54d48acce414f533.

[56] Yaogang Hu et al. “A prediction method for the real-time remaining useful life of wind turbine bearings based on the Wiener process”. In: *Renewable Energy* 127 (Nov. 2018), pp. 452–460. DOI: 10.1016/j.renene.2018.04.033.

[57] Samuel M. Gbashi et al. “Wind Turbine Main Bearing: A Mini Review of Its Failure Modes and Condition Monitoring Techniques”. In: *2022 IEEE 13th International Conference on Mechanical and Intelligent Manufacturing Technologies, ICMIMT 2022*. Institute of Electrical and Electronics Engineers Inc., 2022, pp. 127–134. DOI: 10.1109/ICMIMT55556.2022.9845317.

[58] Shane Butler et al. “A feasibility study into prognostics for the main bearing of a wind turbine”. In: *Proceedings of the IEEE International Conference on Control Applications*. 2012, pp. 1092–1097. DOI: 10.1109/CCA.2012.6402684.

[59] Zhen You Zhang et al. “Wind turbine fault detection based on SCADA data analysis using ANN”. In: *Advances in Manufacturing* 2.1 (Mar. 2014), pp. 70–78. DOI: 10.1007/s40436-014-0061-6.

[60] Jürgen Herp et al. “Bayesian state prediction of wind turbine bearing failure”. In: *Renewable Energy* 116 (Feb. 2018), pp. 164–172. DOI: 10.1016/j.renene.2017.02.069.

[61] Hong Wang et al. “Early fault detection of wind turbines based on operational condition clustering and optimized deep belief network modeling”. In: *Energies* 12.6 (2019). DOI: 10.3390/en12060984.

[62] Shihui Zhang et al. “Early Warning Model of Wind Turbine Front Bearing Based on Conv1D and LSTM”. In: *2021 IEEE International Conference on Industrial Engineering and Engineering Management, IEEM 2021*. Institute of Electrical and Electronics Engineers Inc., 2021, pp. 1029–1034. DOI: 10.1109/IEEM50564.2021.9672830.

[63] Davide Astolfi. *Wind Turbine Drivetrain Condition Monitoring through SCADA-Collected Temperature Data: Discussion of Selected Recent Papers*. May 2023. DOI: 10.3390/en16093614.

[64] Douglas C. Montgomery et al. *Applied statistics and probability for engineers*. Wiley, 2003, p. 706.

[65] Adam M Johansen et al. “Monte carlo methods”. In: *International encyclopedia of education* (2010), pp. 296–303.

[66] *What is Monte Carlo Simulation? | IBM*. URL: https://www.ibm.com/topics/monte-carlo-simulation.

[67] Nicholas Metropolis et al. “The Monte Carlo Method”. In: *Journal of the American Statistical Association* 44.247 (1949), pp. 335–341. DOI: 10.1080/01621459.1949.10483310.

[68] Ben Lutkevich. “Monte Carlo simulation”. In: *Cloud Computing* (Mar. 2023). URL: https://www.techtarget.com/searchcloudcomputing/definition/Monte-Carlo-simulation.

[69] *APPENDIX D MANN-KENDALL ANALYSIS*. Tech. rep.

[70] Alfred L Brophy. *An algorithm and program for calculation of Kendall’s rank correlation coefficient*. Tech. rep. I. 1986, pp. 45–46.

[71] Sheng Yue et al. *Power of the Mann±Kendall and Spearman’s rho tests for detecting monotonic trends in hydrological series*. Tech. rep. URL: www.elsevier.com/locate/jhydrol.

[72] Fan Xu et al. “Extracting degradation trends for roller bearings by using a moving-average stacked auto-encoder and a novel exponential function”. In: *Measurement: Journal of the International Measurement Confederation* 152 (Feb. 2020). DOI: 10.1016/j.measurement.2019.107371.

[73] Liang Guo et al. “A recurrent neural network based health indicator for remaining useful life prediction of bearings”. In: *Neurocomputing* 240 (May 2017), pp. 98–109. DOI: 10.1016/j.neucom.2017.02.045.

[74] Morteza Moradi et al. “Intelligent health indicator construction for prognostics of composite structures utilizing a semi-supervised deep neural network and SHM data”. In: *Engineering Applications of Artificial Intelligence* 117 (Jan. 2023). DOI: 10.1016/j.engappai.2022.105502.

[75] Jamie Coble et al. *Identifying Optimal Prognostic Parameters from Data: A Genetic Algorithms Approach*. Tech. rep.

[76] Gareth James et al. *An Introduction to Statistical Learning*. Vol. 103. Springer Texts in Statistics. New York, NY: Springer New York, 2013. DOI: 10.1007/978-1-4614-7138-7. URL: http://link.springer.com/10.1007/978-1-4614-7138-7.

[77] *Regression Model Accuracy (MAE, MSE, RMSE, R-squared) Check in R*. Feb. 2019. URL: https://www.datatechnotes.com/2019/02/regression-model-accuracy-mae-mse-rmse.html.

[78] A. Zeiler et al. “Empirical mode decomposition - An introduction”. In: *Proceedings of the International Joint Conference on Neural Networks*. 2010. DOI: 10.1109/IJCNN.2010.5596829.

[79] Yuqing Li. *VITAL SIGNS MONITORING USING DOPPLER SIGNAL DECOMPOSITION*. Tech. rep.

[80] Steven R L et al. *The empirical mode decomposition and the Hilbert spectrum for nonlinear and non-stationary time series analysis*. Tech. rep. 1998, pp. 903–995. URL: https://royalsocietypublishing.org/.

[81] Boualem Boashash et al. “Advanced time-frequency signal and system analysis”. In: *Time-Frequency Signal Analysis and Processing: A Comprehensive Reference*. Elsevier Inc., Dec. 2016, pp. 141–236. DOI: 10.1016/B978-0-12-398499-9.00004-2.

[82] Donghoh Kim et al. *EMD: A Package for Empirical Mode Decomposition and Hilbert Spectrum*. Tech. rep.

[83] Ting Zhu et al. “A novel hybrid scheme for remaining useful life prognostic based on secondary decomposition, BiGRU and error correction”. In: *Energy* 276 (2023), p. 127565. DOI: https://doi.org/10.1016/j.energy.2023.127565. URL: https://www.sciencedirect.com/science/article/pii/S0360544223009593.

[84] Huixing Meng et al. “A hybrid method for prognostics of lithium-ion batteries capacity considering regeneration phenomena”. In: *Energy* 261 (Aug. 2022), p. 125278. DOI: 10.1016/j.energy.2022.125278. URL: https://doi.org/10.1016/j.energy.2022.125278.

[85] Fei Xia et al. “State-of-Health Prediction for Lithium-Ion Batteries Based on Complete Ensemble Empirical Mode Decomposition with Adaptive Noise-Gate Recurrent Unit Fusion Model”. In: *Energy Technology* 10.4 (Apr. 2022). DOI: 10.1002/ente.202100767.

[86] Qiuhua Du et al. “Application of the EMD method in the vibration analysis of ball bearings”. In: *Mechanical Systems and Signal Processing* 21.6 (Aug. 2007), pp. 2634–2644. DOI: 10.1016/j.ymssp.2007.01.006.

[87] Mahdi Hameed Al-Badrawi et al. *Statistical Properties and Applications of Empirical Mode Decomposition*. Tech. rep. 2017. URL: https://scholars.unh.edu/dissertation/2280.

[88] Joachim Blaafjell Holwech et al. *Empirical Mode Decomposition for Improved Noise Filtering and Classification of Two-Dimensional Data*. Tech. rep.

[89] Alexandros Karagiannis et al. “Noise-assisted data processing with empirical mode decomposition in biomedical signals”. In: *IEEE Transactions on Information Technology in Biomedicine* 15.1 (Jan. 2011), pp. 11–18. DOI: 10.1109/TITB.2010.2091648.

[90] Guomin Li et al. “Hybrid forecasting system considering the influence of seasonal factors under energy sustainable development goals”. In: *Measurement: Journal of the International Measurement Confederation* 211 (Apr. 2023). DOI: 10.1016/j.measurement.2023.112607.

[91] A. Antico et al. “Analysis of hydroclimatic variability and trends using a novel empirical mode decomposition: Application to the Paraná River Basin”. In: *Journal of Geophysical Research* 119.3 (Feb. 2014), pp. 1218–1233. DOI: 10.1002/2013JD020420.

[92] Yunus A Cengel. *Steady versus Transient Heat Transfer 63 Multidimensional Heat Transfer 64 Heat Generation 66*. Tech. rep.

[93] Georgios Galanopoulos et al. “A novel strain-based health indicator for the remaining useful life estimation of degrading composite structures”. In: *Composite Structures* 306 (Feb. 2023). DOI: 10.1016/j.compstruct.2022.116579.

[94] Naipeng Li et al. “An Improved Exponential Model for Predicting Remaining Useful Life of Rolling Element Bearings”. In: *IEEE Transactions on Industrial Electronics* 62.12 (Dec. 2015), pp. 7762–7773. DOI: 10.1109/TIE.2015.2455055.

[95] Jia Tang et al. “A Health Monitoring Method Based on Multiple Indicators to Eliminate Influences of Estimation Dispersion for Lithium-Ion Batteries”. In: *IEEE Access* 7 (2019), pp. 122302–122314. DOI: 10.1109/ACCESS.2019.2936213.

[96] Xuefeng Kong et al. “Remaining useful life prediction for degrading systems with random shocks considering measurement uncertainty”. In: *Journal of Manufacturing Systems* 61 (Oct. 2021), pp. 782–798. DOI: 10.1016/j.jmsy.2021.05.019.

[97] Sofia Koukoura. *Failure and Remaining Useful Life Prediction of Wind Turbine Gearboxes*. Tech. rep.

[98] A. Mosallam et al. “Data-driven prognostic method based on Bayesian approaches for direct remaining useful life prediction”. In: *Journal of Intelligent Manufacturing* 27.5 (Oct. 2016), pp. 1037–1048. DOI: 10.1007/s10845-014-0933-4.

[99] Pangun Park et al. “Remaining useful life estimation of bearings using data-driven ridge regression”. In: *Applied Sciences (Switzerland)* 10.24 (Dec. 2020), pp. 1–17. DOI: 10.3390/app10248977.

[100] Julius O Smith III. *Mathematics of the Discrete Fourier Transform (DFT)*. Tech. rep. 2002. URL: http://www-ccrma.stanford.edu/~jos/mdft/..

[101] Reinout Heijungs. “On the number of Monte Carlo runs in comparative probabilistic LCA”. In: *International Journal of Life Cycle Assessment* 25.2 (Feb. 2020), pp. 394–402. DOI: 10.1007/s11367-019-01698-4.

[102] Egbo Mary Nkechi et al. “A Monte Carlo Simulation Comparison of Methods of Detecting Outliers in Time Series Data”. In: *Journal of Statistics Applications and Probability* 11.3 (Sept. 2022), pp. 819–832. DOI: 10.18576/jsap/110306.

[103] *Explained: Sigma*. Feb. 2012. URL: https://news.mit.edu/2012/explained-sigma-0209.

[104] Jannis Tautz-Weinert. *Improved Wind Turbine Monitoring Using Operational Data*. Tech. rep. 2018. URL: http://awesome-h2020.eu/.

[105] James M Lucas et al. *Technomeirics session of the 33rd Annual Fall*. Tech. rep.

[106] Elisha De Mello et al. “Data driven case study of a wind turbine main-bearing failure”. In: *Journal of Physics: Conference Series*. Vol. 2018. 1. IOP Publishing Ltd, Sept. 2021. DOI: 10.1088/1742-6596/2018/1/012011.

[107] Mary Ann Branch et al. “Subspace, interior, and conjugate gradient method for large-scale bound-constrained minimization problems”. In: *SIAM Journal of Scientific Computing* 21.1 (1999), pp. 1–23. DOI: 10.1137/S1064827595289108.

A

Appendix

A.1. SCADA data measurements

Absolute_wind_direction_corrected: (°)	Gearbox_bearing_1_temperature: (°C)	Active_power: (kW)
Absolute_wind_direction: (°)	Gearbox_bearing_2_temperature: (°C)	Apparent_power: (kVA)
Nacelle_angle_corrected: (°)	Gearbox_inlet_temperature: (°C)	Converter_torque: (Nm)
Nacelle_angle: (°)	Gearbox_oil_sump_temperature: (°C)	Generator_converter_speed: (rpm)
Pitch_angle: (°)	Generator_bearing_1_temperature: (°C)	Generator_speed: (rpm)
Vane_position_1: (°)	Generator_bearing_2_temperature: (°C)	Grid_frequency: (Hz)
Vane_position_2: (°)	Generator_stator_temperature: (°C)	Grid_voltage: (V)
Vane_position: (°)	Hub_temperature: (°C)	Pitch_angle_setpoint: (unitless)
	Nacelle_temperature: (°C)	Power_factor: (unitless)
	Outdoor_temperature: (°C)	Reactive_power: (kVAr)
	Rotor_bearing_temperature: (°C)	Rotor_speed: (rpm)
		Torque: (Nm)
		Wind_speed: (m/s)
		Wind_speed_1: (m/s)
		Wind_speed_2: (m/s)

Table A.1: Case study 1 - Sensor measurements available in the SCADA dataset

wtc_YawPos_mean(°)	wtc_AmbieTmp_mean(°C)	wtc_ActPower_mean(kW)
wtc_YawPos_stddev(°)	wtc_AmbieTmp_stddev(°C)	wtc_ActPower_stddev(kW)
wtc_PitcPosA_mean(°)	wtc_A3RigTmp_mean(°C)	wtc_AcWindSp_stddev(m/s)
wtc_PitcPosA_stddev(°)	wtc_A3RigTmp_stddev(°C)	wtc_AcWindSp_stddev(m/s)
wtc_PitcPosB_mean(°)	wtc_MainBTmp_mean(°C)	wtc_GenRpm_mean(RPM)
wtc_PitcPosB_stddev(°)	wtc_MainBTmp_stddev(°C)	wtc_GenRpm_stddev(RPM)
wtc_PitcPosC_mean(°)		wtc_MainSRpm_mean(RPM)
wtc_PitcPosC_stddev(°)		wtc_MainSRpm_stddev(RPM)
wtc_NacelPos_mean(°)		wtc_ScInOper_timeon(s)
wtc_NacelPos_stddev(°)		

Table A.2: Case study 2 - Sensor measurements available in the SCADA dataset

A.2. Case Study 1 wind turbine main bearing temperatures

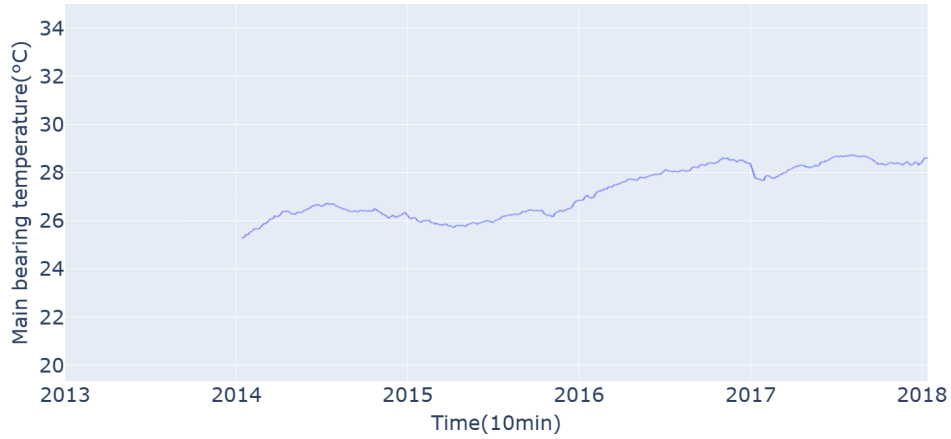

Figure A.1: Case Study 1 - Yearly rolling average of the Turbine A main bearing temperature

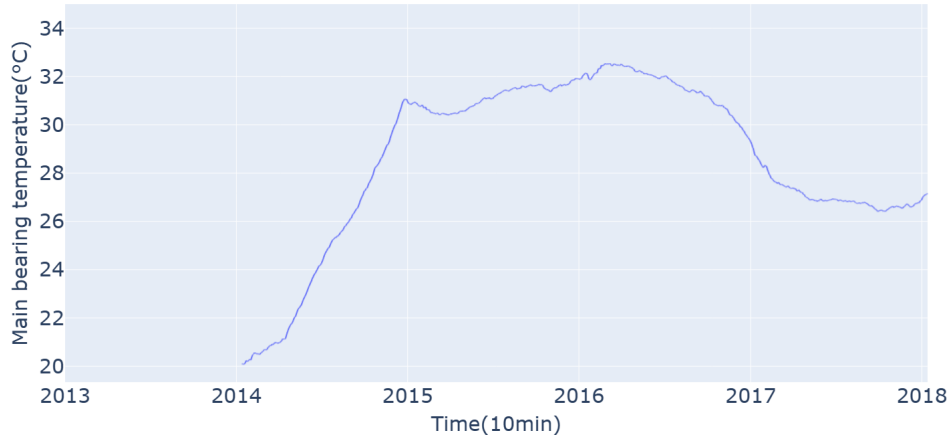

Figure A.2: Case Study 1 - Yearly rolling average of the Turbine B main bearing temperature

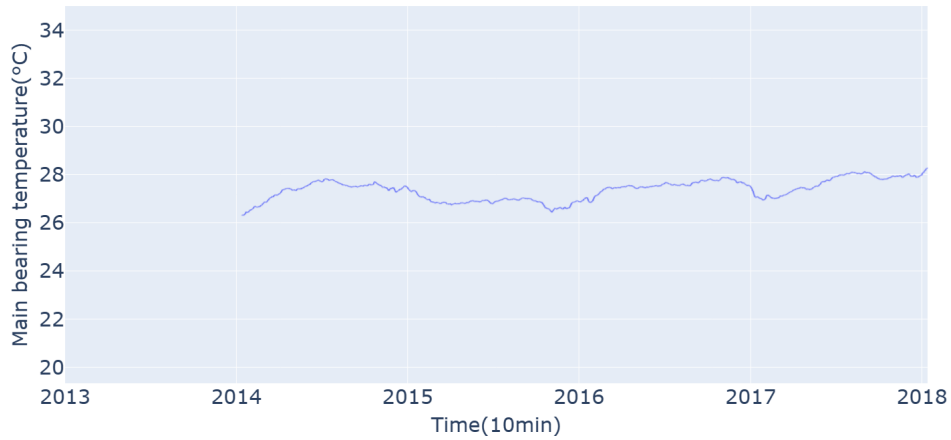

Figure A.3: Case Study 1 - Yearly rolling average of the Turbine C main bearing temperature

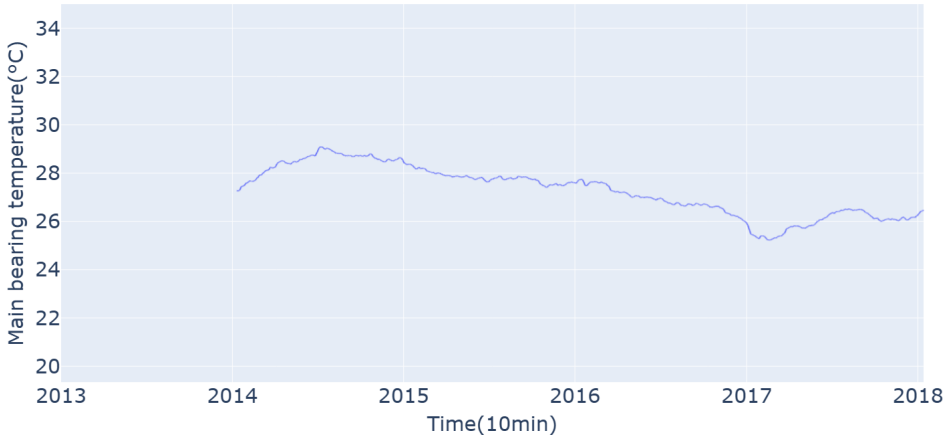

Figure A.4: Case Study 1 - Yearly rolling average of the Turbine D main bearing temperature

A.3. Various group divisions

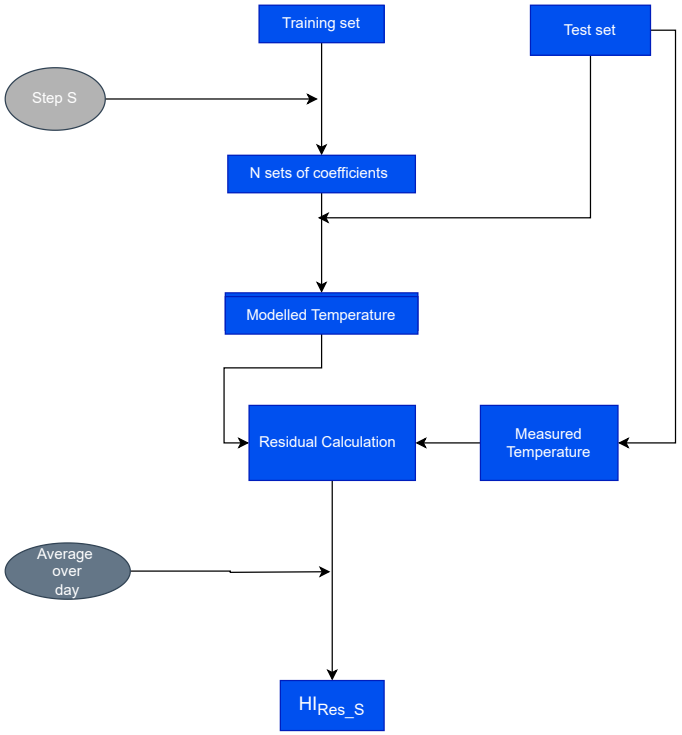

Figure A.5: Case Study 1 - implementation of Step S with N groups division to calculate HI_{Res_S}

The seasonality step proposed in Section 4.3.1 proposes to divide the dataset into N groups based on the time period of the year. Various so that each group has a corresponding set of coefficients. This section explores different data divisions, such as:

- No division-baseline approach- 1 set of coefficients
- 2 groups -(colder month/ hotter month)- 2 sets of coefficients
- 4 groups -(Winter/Spring/Summer/Fall)- 4 sets of coefficients
- 12 groups- (12 month)- 12 sets of coefficients

Figure A.5 illustrates a flowchart for obtaining HI_{Res_S} based on N number of group division. First, this section compares the performance of different data division models based on the RMSE value of the testing set. Next, this section compares cross correlation between different data divisions HI_{Res_S} and ambient temperature.

Figure 5.23 shows the RMSE metric of various models on the testing set to compare model performance for various data divisions. The variability in performance metrics across different group divisions is minimal, with variations observed only up to the third decimal of RMSE values. The slight improvement, while statistically insignificant, is attributed to the inclusion of a larger number of models. It's important to note that the use of multiple equations primarily aims to reduce the impact of seasonality rather than improving fit quality.

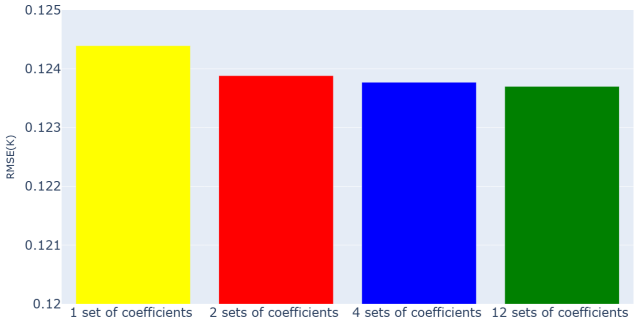

Figure A.6: Case Study 1 - RMSE of the testing set at various group divisions

Figure A.7 shows the correlation of the various HI_{Res_S} with the ambient temperature for various group divisions. The figure shows a significantly reduced cross-correlation with ambient temperature when increasing the number of models. Monthly sets of coefficients, which represent each month having a separate model, correspond to the lowest cross-correlation with ambient temperature and lowest RMSE. Moreover, the monthly data division provides the lowest RMSE. Thus, the twelve-month division was selected, and the monthly sets of coefficients are shown in Table A.3.

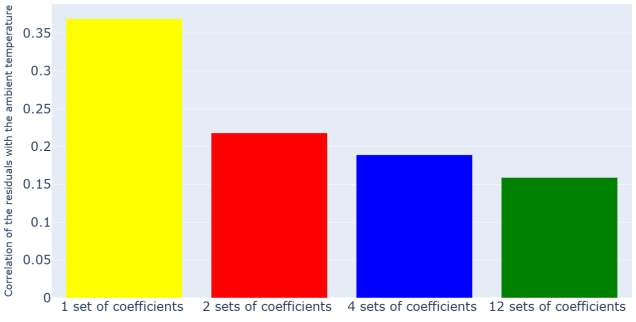

Figure A.7: Case Study 1 - Cross-correlation of the HIs with the ambient temperature at various group divisions

It should be pointed out that this method of choosing data set division is not optimal. It is suggested that the number of models be tuned based on the failed case study to determine the effect of decreasing seasonality on the accuracy of the RUL predictions. Select the optimal number of sets of coefficients needed based on the accuracy of RUL predictions and computational insensitivity of the chosen group division.

Month	β_1	β_2	$\beta_3(K * s^2/rad^2)$	$\beta_4(K/kW)$
January	0.983	0.01687	0.05487	8.31401e-05
February	0.985	0.01482	0.05687	4.37707e-05
March	0.984	0.01568	0.05857	4.4055e-05
April	0.984	0.01599	0.07446	1.32073e-16
May	0.984	0.01547	0.07661	3.31832e-09
June	0.985	0.01510	0.07060	6.89188e-27
July	0.984	0.01538	0.06981	3.05456e-16
August	0.984	0.01590	0.07373	1.7773e-27
September	0.984	0.01585	0.06818	8.46872e-06
October	0.984	0.01578	0.07389	2.1686e-17
November	0.982	0.01739	0.07538	3.35381e-05
December	0.984	0.01582	0.06725	4.69846e-05

Table A.3: Case Study 1 - Main bearing temperature model monthly sets of coefficients of Equation 4.4

A.4. CEEMDAN decomposition

A.4.1. Case Study 1

Noise comparison

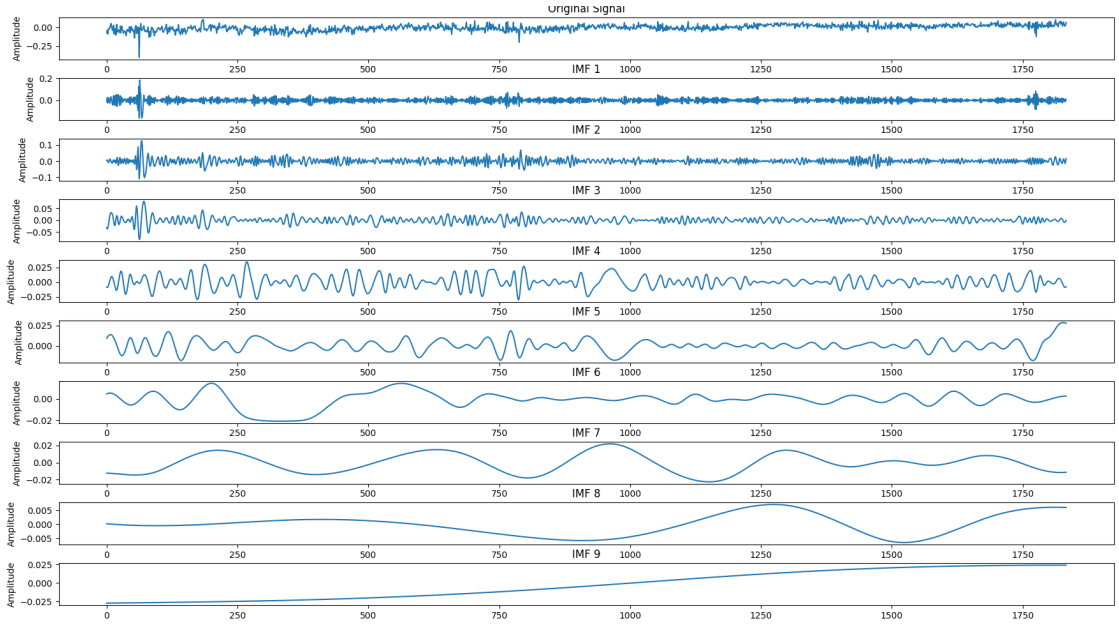

Figure A.8: Case Study 1 - $HI_{Res\_Baseline}$ CEEMDAN decomposition

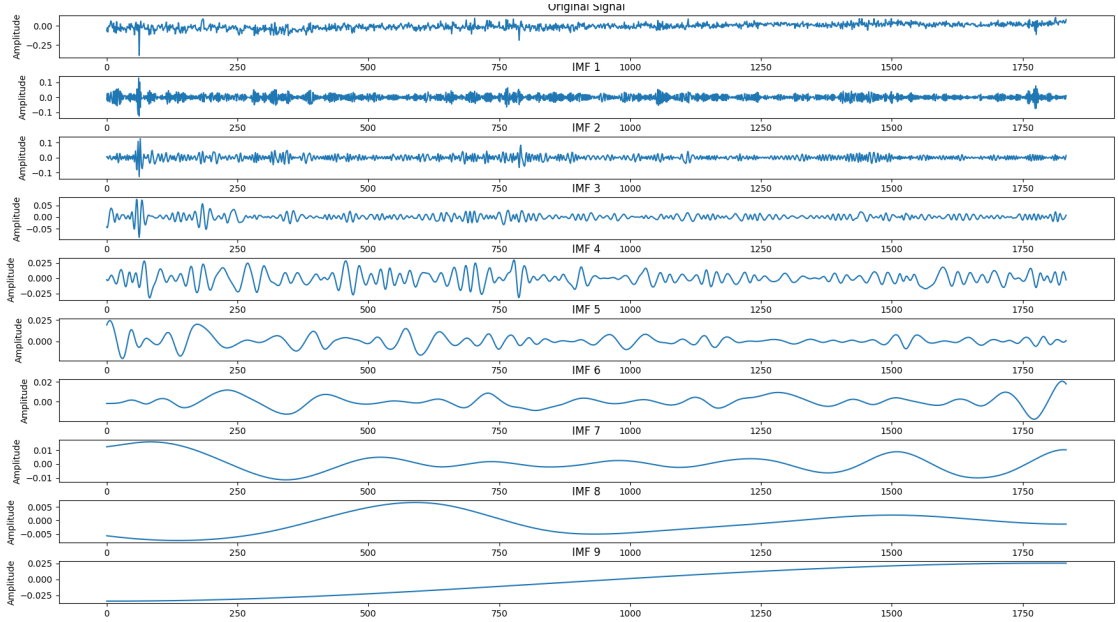

Figure A.9: Case Study 1 - HI_{Res_S} CEEMDAN decomposition

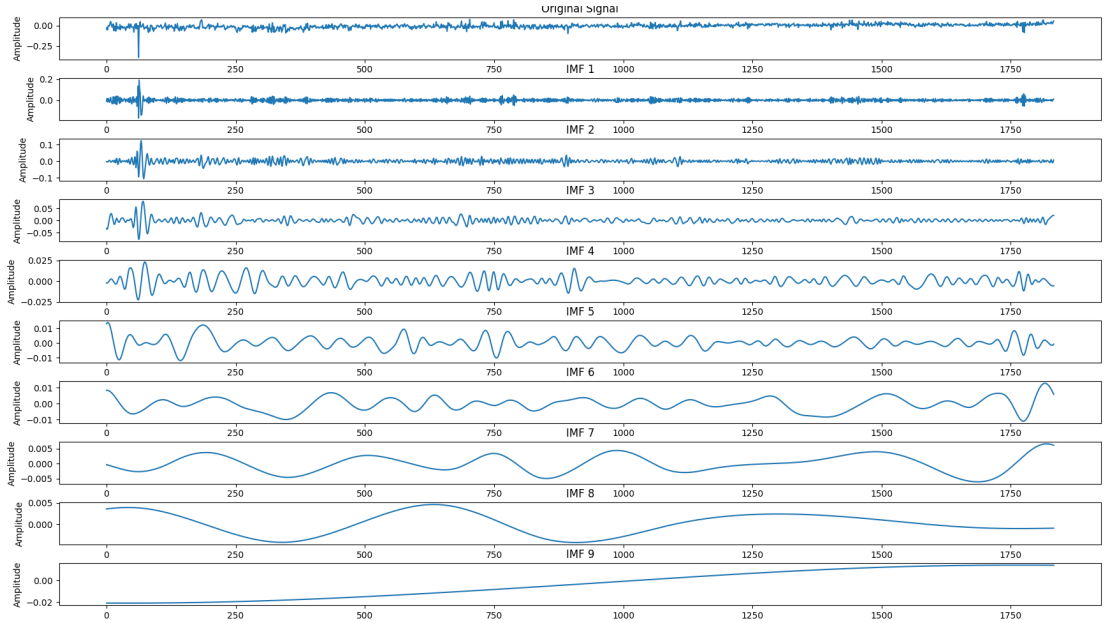

Figure A.10: Case Study 1 - $HI_{Res\_S\_M}$ CEEMDAN decomposition

Noise comparison, density of threshold region

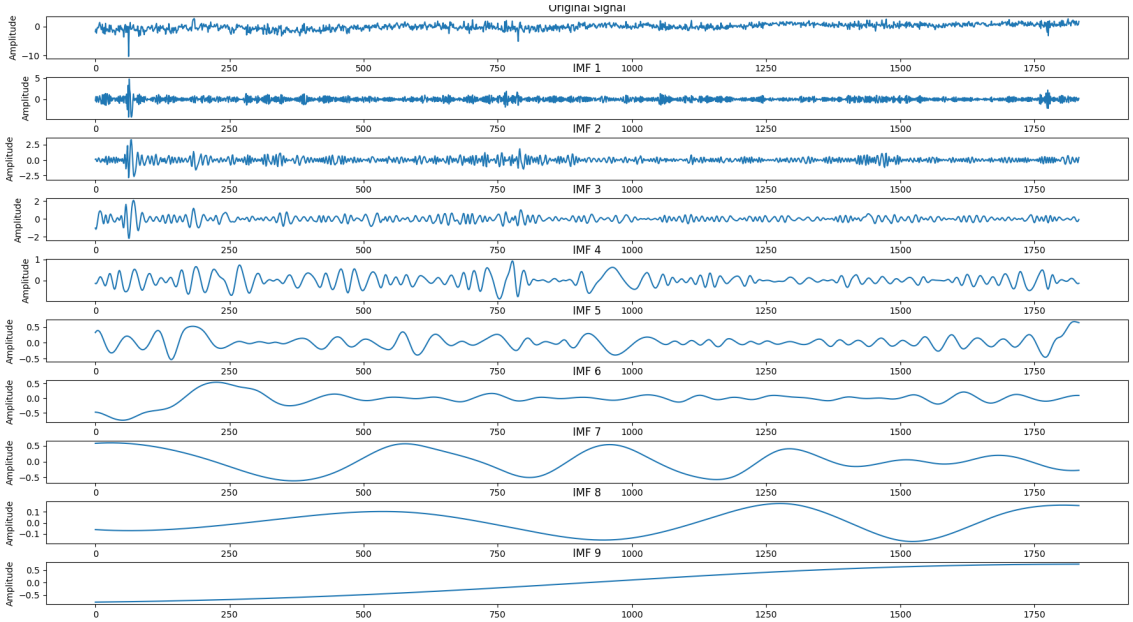

Figure A.11: Case Study 1 - Normalized $HI_{Res\_Baseline}$ CEEMDAN decomposition

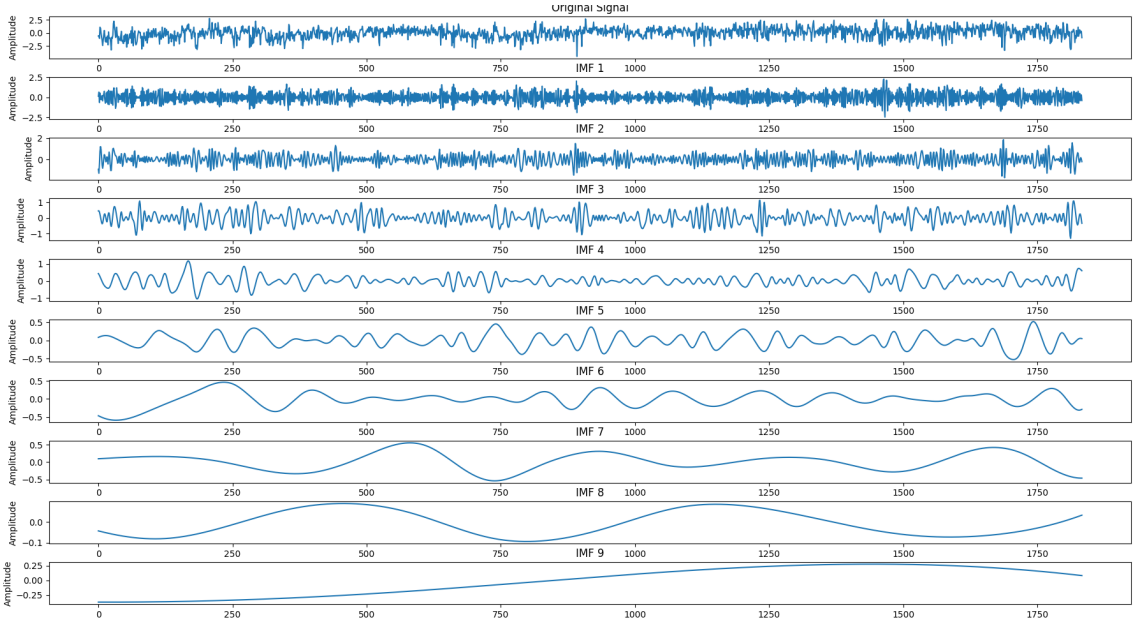

Figure A.12: Case Study 1 - Normalized HI_{Alt} CEEMDAN decomposition

Noise comparison, Binned HI

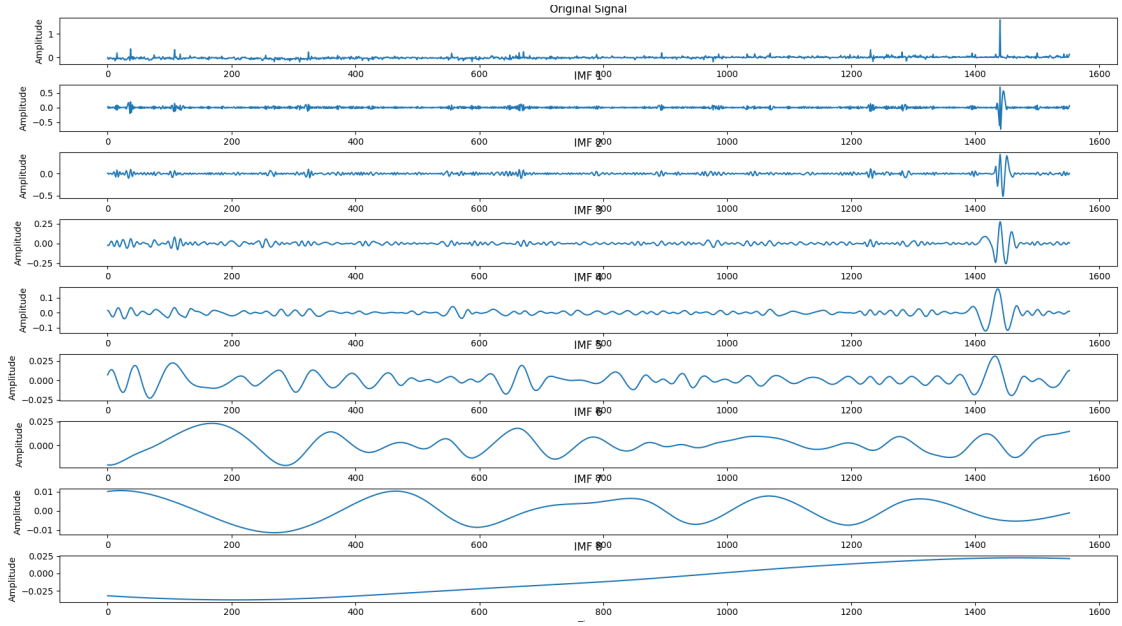

Figure A.13: Case Study 1 - $HI_{Res\_S\_M\_B}$ 13 RPM CEEMDAN decomposition

A.4.2. Case Study 2

Noise comparison

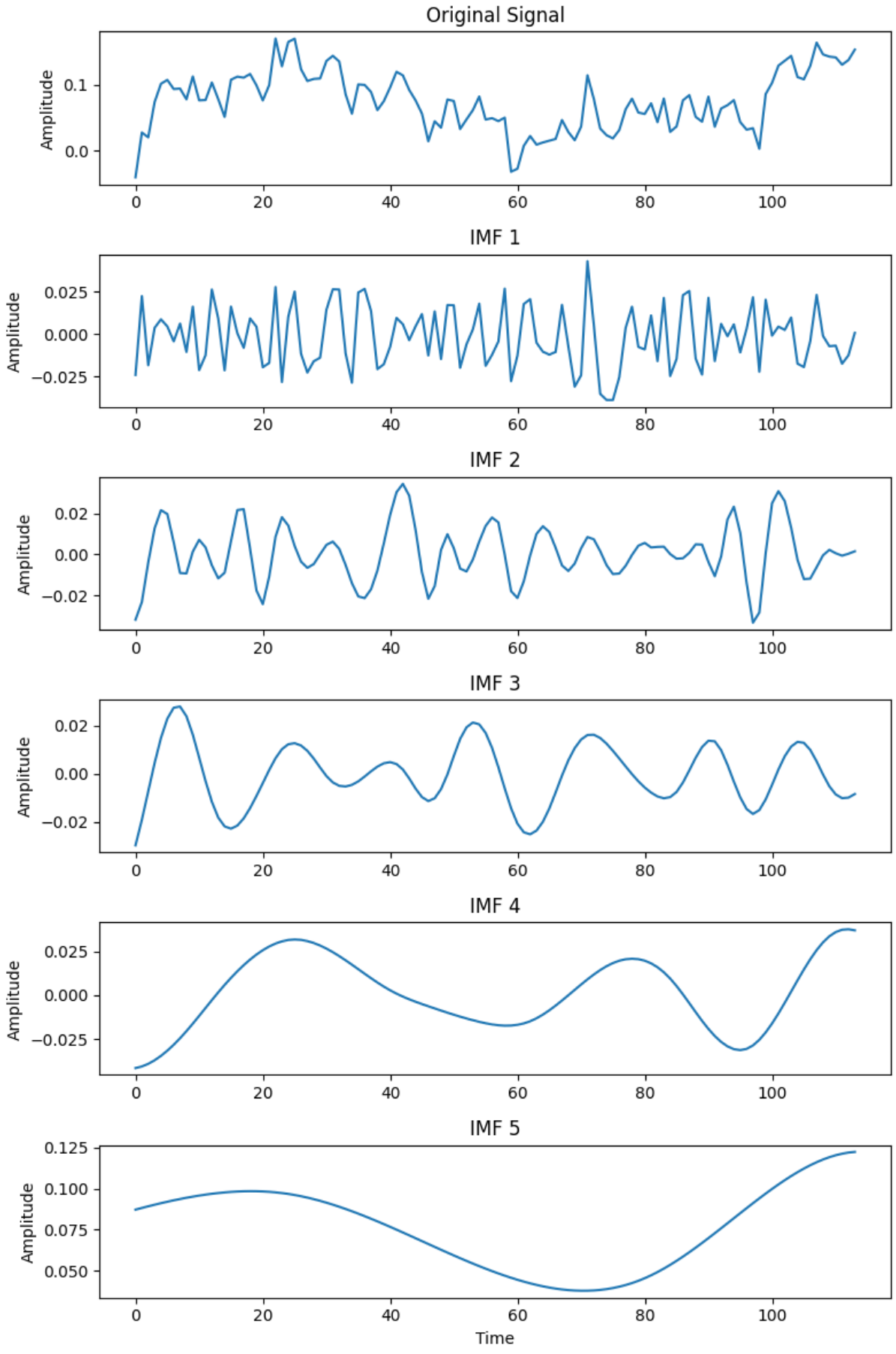

Figure A.14: Case Study 2 - $HI'_{Res\_Baseline}$ CEEMDAN decomposition

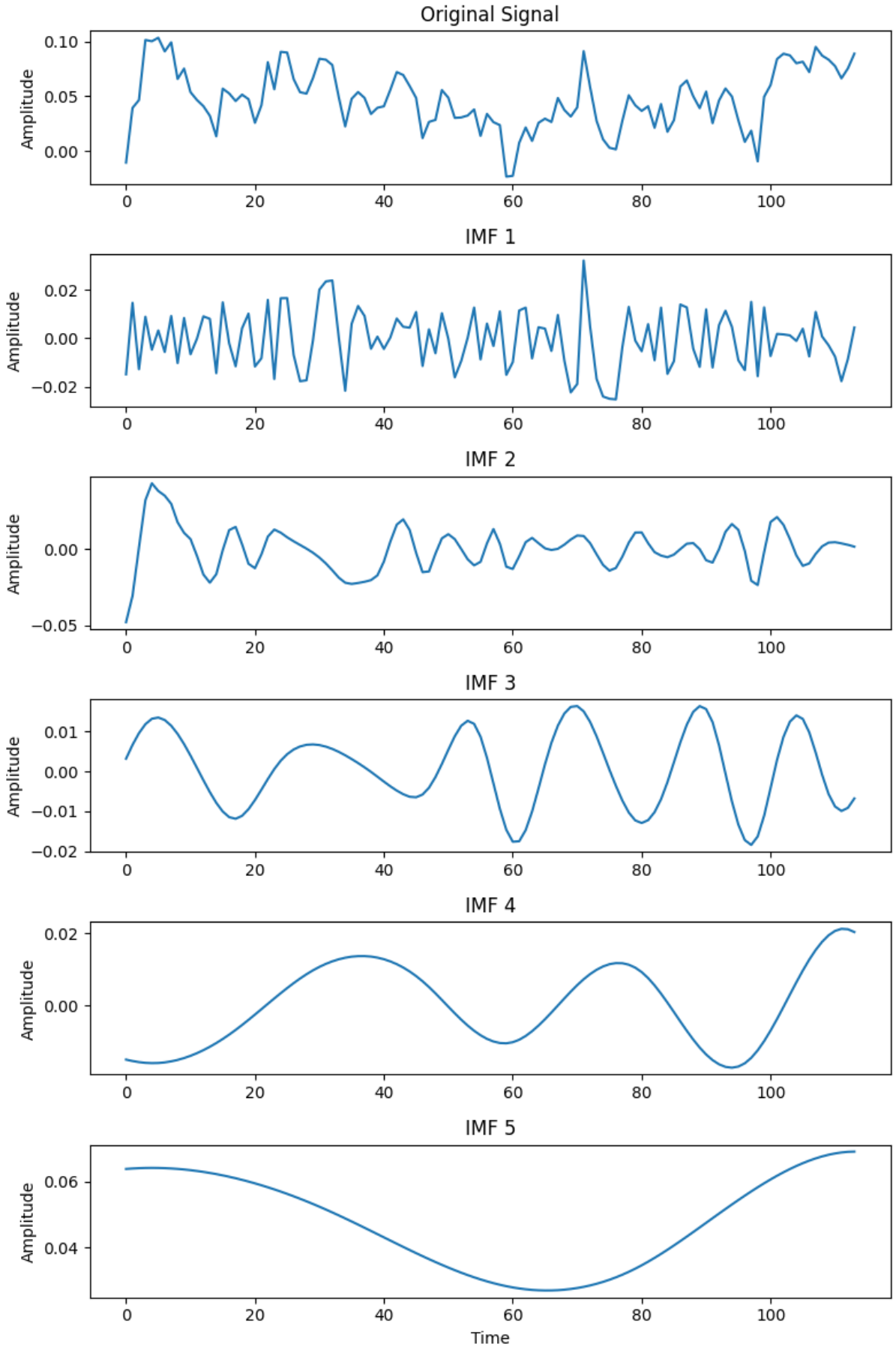

Figure A.15: Case Study 2 - HI'_{Res_M} CEEMDAN decomposition

Noise comparison, density of the threshold region

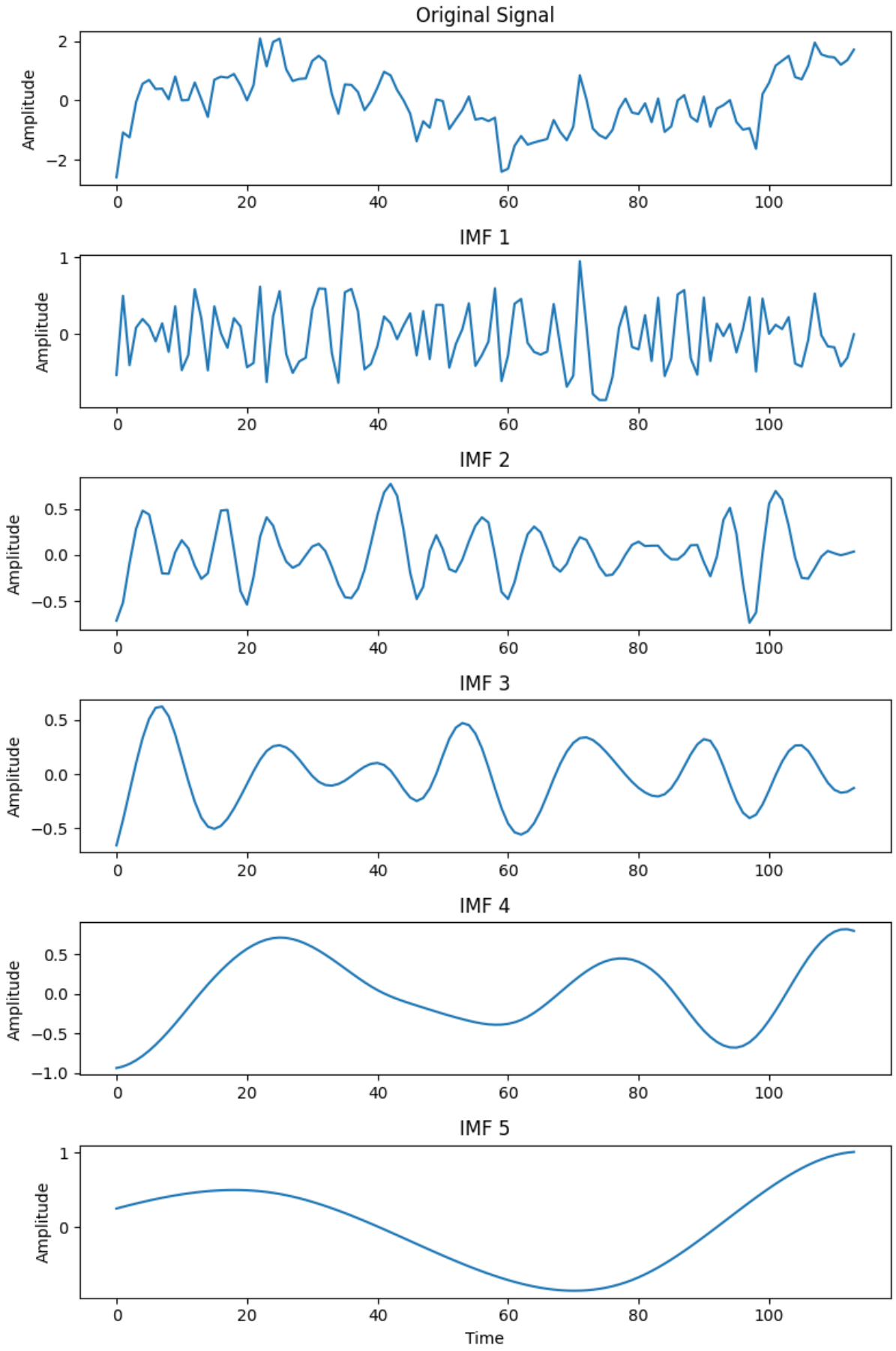

Figure A.16: Case Study 2 - Normalized $HI'_{Res\_Baseline}$ CEEMDAN decomposition

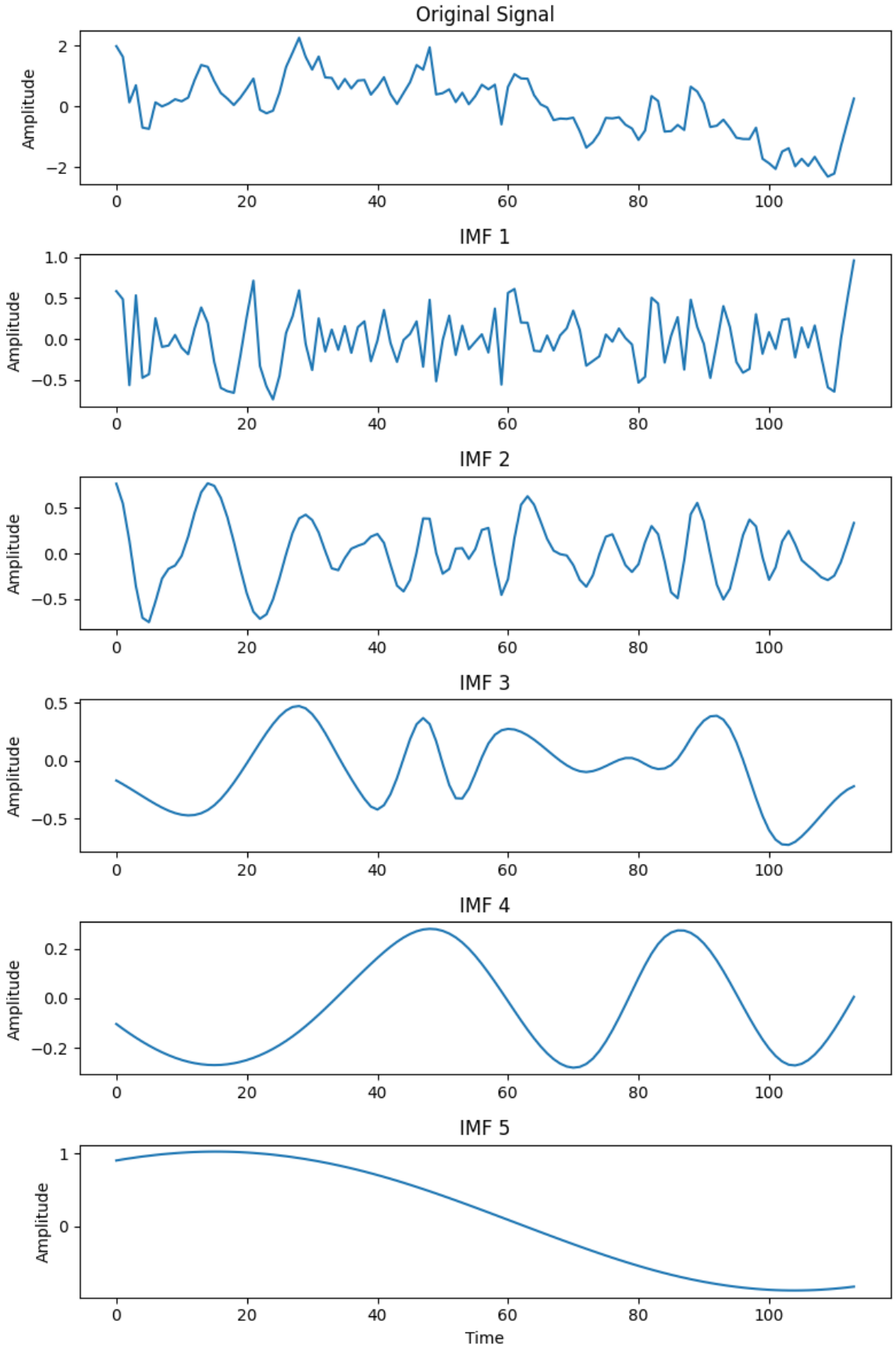

Figure A.17: Case Study 2 - Normalized HI'_{Alt} CEEMDAN decomposition

A.5. Non-linear least squares

In Case Study 2, utilizing the exponential term in the main bearing temperature model requires the application of non-linear least squares. The non-linear least squares algorithm can be shown as:

$$L(\beta) = \sum_{i=1}^{N} (y_i - \hat{y}_i)^2 = \sum_{i=1}^{N} (y_i - f(x_i, \beta))^2 \tag{A.1}$$

Where y_i is the actual value, $\hat{y}_i$ is the estimated value, x_i are independent values, and β represent regression parameters to be estimated [107]. The least squares function from the Python "scipy.optimize" library is used to perform regression. The applied function is based on the trust region method algorithm.

Trust region methods approximate function L with simpler function q, which is assumed as a valid approximation in the neighborhood around β; this neighborhood is referred to as trust region. The introduced trust-region sub-problem can be shown as follows:

$$\min_{s} \{q(s) \quad s \in \mathbb{N}\} \tag{A.2}$$

Where s is referred to as the trial step and calculated by minimizing over N. To obtain approximation q, the standard trust region method uses the first two terms of the Taylor approximation of Equation A.1 at β. Where trust region N can be described using a spherical or ellipsoidal shape. To estimate parameters, the current β then gets updated to $\beta + s$ when $L(\beta + s) < L(\beta)$ or β remains the same, and the trust region of N is reduced, and the trial step computation is repeated. Trust region algorithm iteratively refines estimated β until the solution converges.

A.6. Case Study 2 - HIs with different EWMA smoothing factors

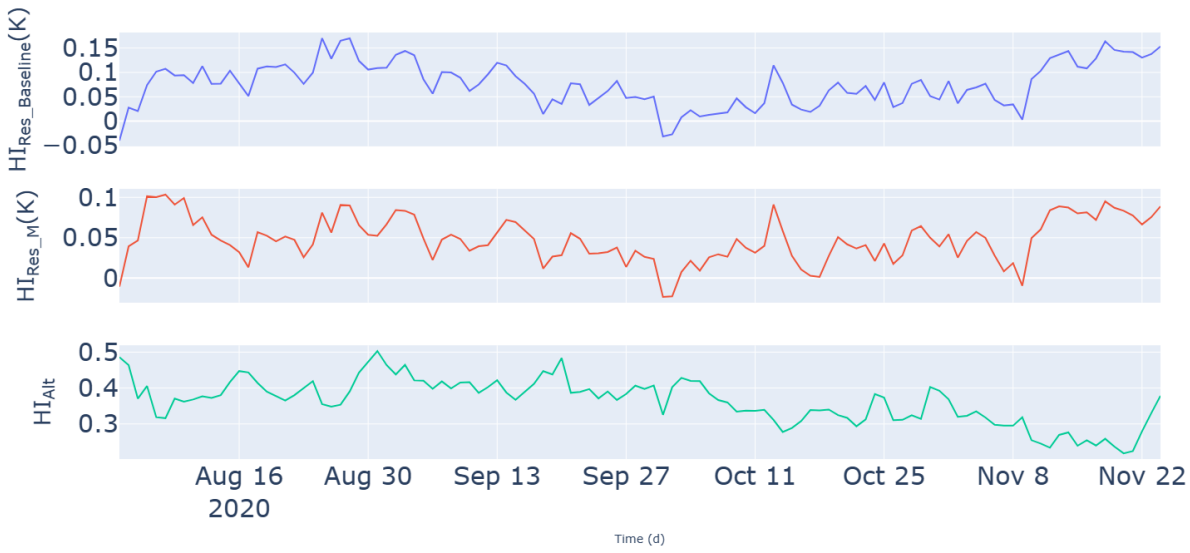

Figure A.18: Case study 2 - $HI'_{Res\_Baseline}$, HI'_{Res_M} and HI'_{Alt}obtained using EWMA smoothing factor λ= 0.2

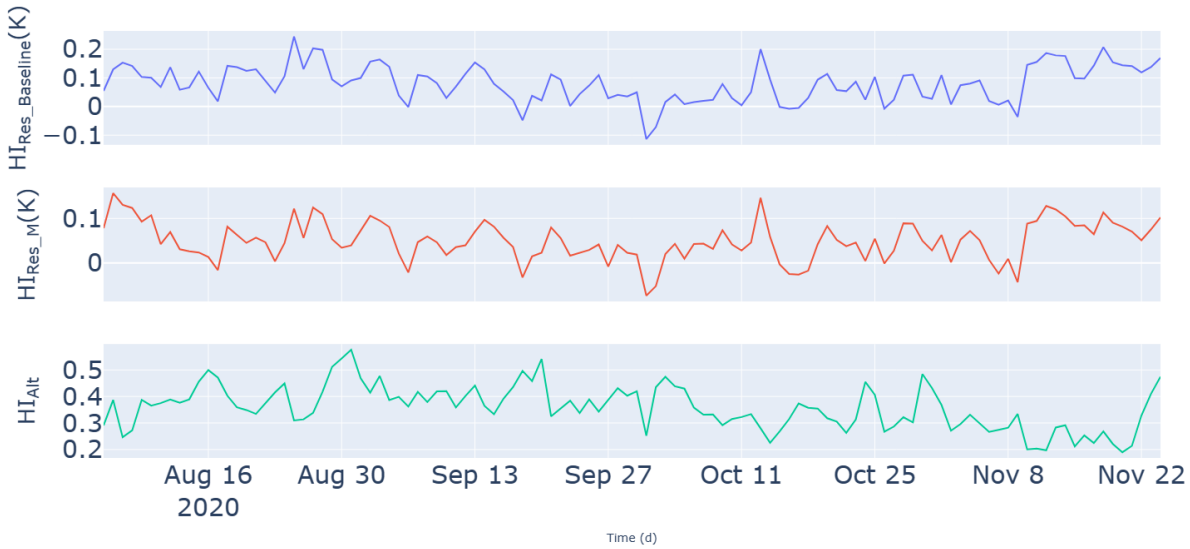

Figure A.19: Case study 2 - $HI'_{Res\_Baseline}$, HI'_{Res_M} and HI'_{Alt}obtained using EWMA smoothing factor λ= 0.4

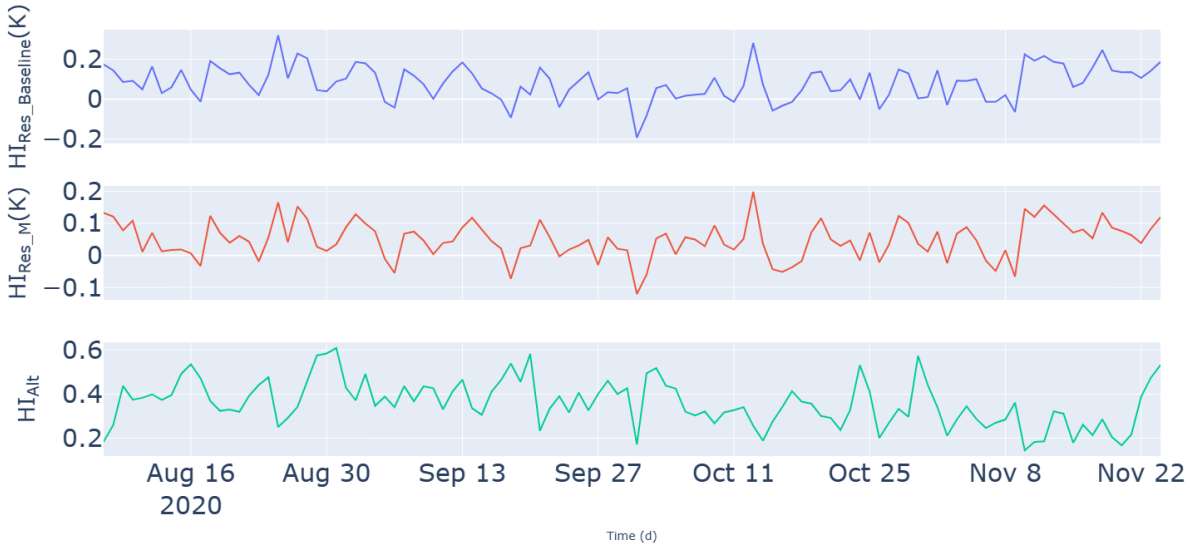

Figure A.20: Case study 2 - $HI'_{Res\_Baseline}$, HI'_{Res_M} and HI'_{Alt}obtained using EWMA smoothing factor λ= 0.6

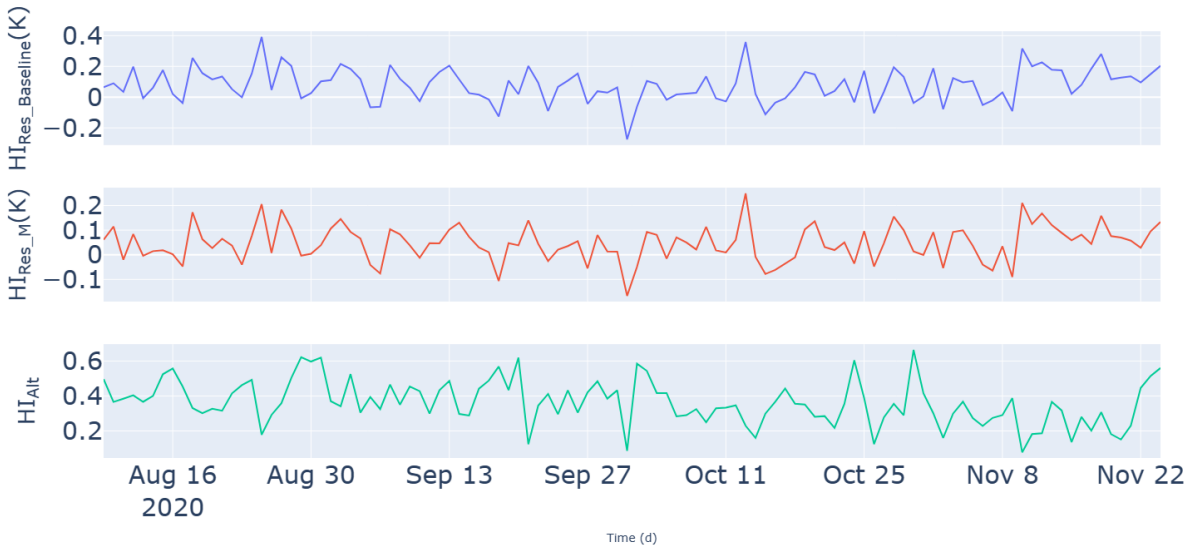

Figure A.21: Case study 2 - $HI'_{Res\_Baseline}$, HI'_{Res_M} and HI'_{Alt}obtained using EWMA smoothing factor λ= 0.8

A.7. Step B - Binning by the rotational speed

Step B was explored as an additional post-processing step to take variable operating conditions into account. The idea is that the residuals of a healthy turbine within each bin should have a consistent behavior, while a gradual change across binned residuals indicates degradation. Binning is performed by dividing the residuals according to the rotational speed values of the rotor. The reason for grouping the residuals based on the rotational speed of the rotor is that it is directly linked to the main bearing operation, unlike power or wind speed. Figure A.22 shows the procedure adopted for applying the binning step.

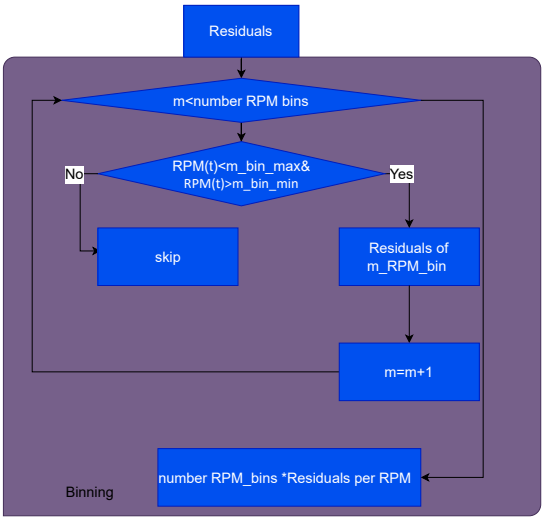

Figure A.22: Binning step (Step B)

Initially, the rotational speed values of the rotor are divided into bins using the ”groupby” function in Python. Subsequently, each residual is categorized into its corresponding bin, leading to different sets of residuals for each bin. It is important to note that the number and range of bins can be tuned based on a specific case study.

A.7.1. Case Study 1- Step B

Similar to the HIs obtained in Case Study 1, Figure A.23 illustrates a flowchart to obtain $HI_{Res\_S\_M\_B}$ where Step B is applied as a subsequent step after residual calculation. According to the method shown in Figure A.23, coefficients obtained from Step S are used to model the main bearing temperature of the test set employing Step M. Using the upper and lower thresholds obtained for each timestamp of the test set from Step M, residuals are calculated as described in Section 4.3.2.1. The residuals obtained are binned and averaged daily to obtain $HI_{Res\_S\_M\_B}$. Notably, unlike the previous HIs where a single time series was obtained, the binning process generates multiple time series.

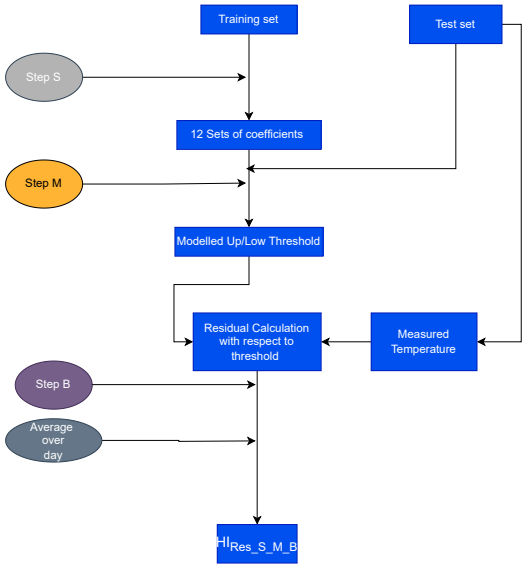

Figure A.23: Case Study 1 - implementation of Step S, Step M, and Step B to calculate $HI_{Res\_S\_M\_B}$

For the 2MW wind turbine under consideration, the operational range of rotational speeds lies between 11 and 17 rpm. Bins with a length of 1 RPM have been analysed. Consequently, the rotational speed range has been divided into seven bins, with each bin representing a 1 RPM interval. As an example, the $HI_{Res\_S\_M\_B}$ at 13 RPM is shown in Figure A.24.

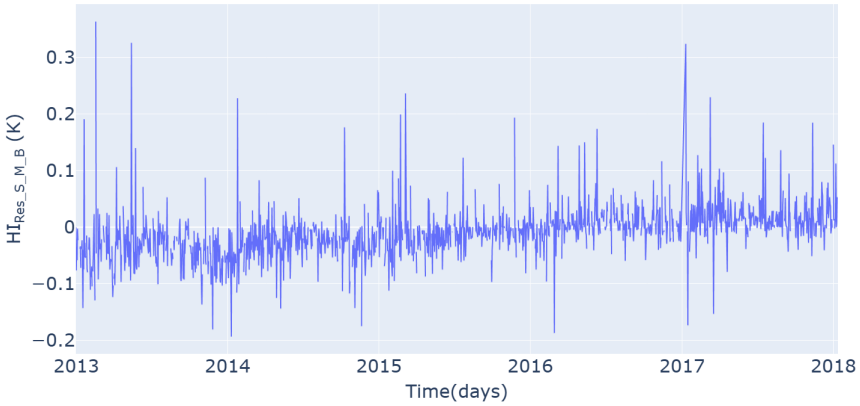

Figure A.24: Case Study 1, Test set - Step S, Step M, and Step B HI at 13 RPM, $HI_{Res\_S\_M\_B}$

Figure A.24 illustrates an upward trend similar to $HI_{Res\_Baseline}$ shown in Figure 5.10. However, gaps in data and a significant increase in outliers compared to $HI_{Res\_Baseline}$ should be noted. Similar to previous case studies, Figures A.25, A.26, and A.28 compare the HIs in terms of monotonicity and dispersion. The

horizontal red line represents the baseline HI ($HI_{Res\_Baseline}$) metric, and bars represent $HI_{Res\_S\_M\_B}$ at different RPM bins.

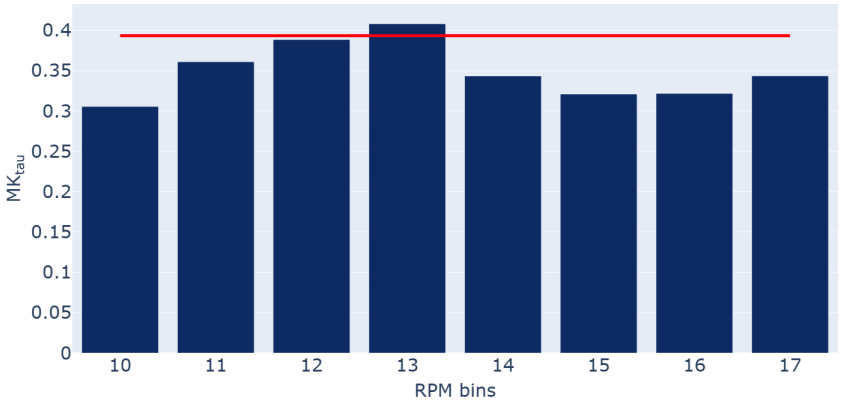

Figure A.25: Case Study 1 - $HI_{Res\_Baseline}$, $HI_{Res\_S\_M}$ at different RPMs, monotonicity comparison using MK τ

Figure A.25 illustrates no significant improvements in the monotonicity. With the exception of the 13 RPM bin, the values of $HI_{Res\_S\_M\_B}$ for monotonicity are generally lower than the Baseline HI ($HI_{Res\_Baseline}$). It is important to point out that bins except 11, 12, and 13 RPM bins show similar values. Thus, trends present across these RPM bins are similar.

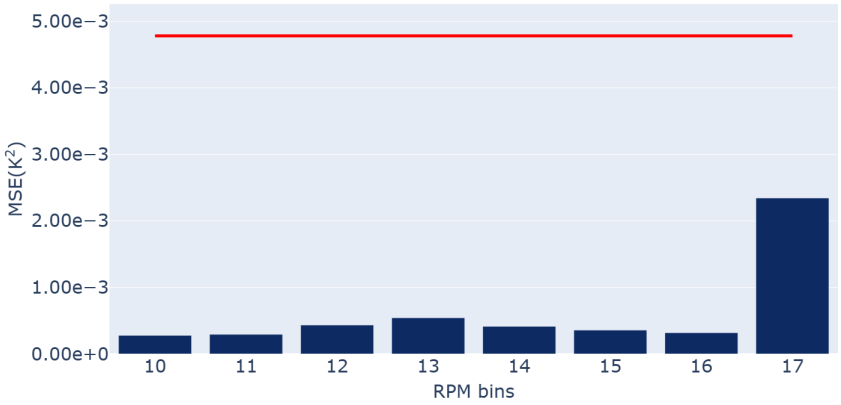

Figure A.26: Case Study 1 - $HI_{Res\_Baseline}$, $HI_{Res\_S\_M}$ at different RPMs, dispersion comparison using MSE

The lower value of the MSE metric illustrated in Figure A.26 indicates that the binned HIs are less dispersed than $HI_{Res\_Baseline}$. Notably, the MSE metric of the 17 RPM bin is significantly higher than that of other bins. The difference in the metrics is attributed to the 17 RPM bin having the lowest amount of data points compared to other bins (1100 days), which leads to an increased number of outliers (Figure A.27).

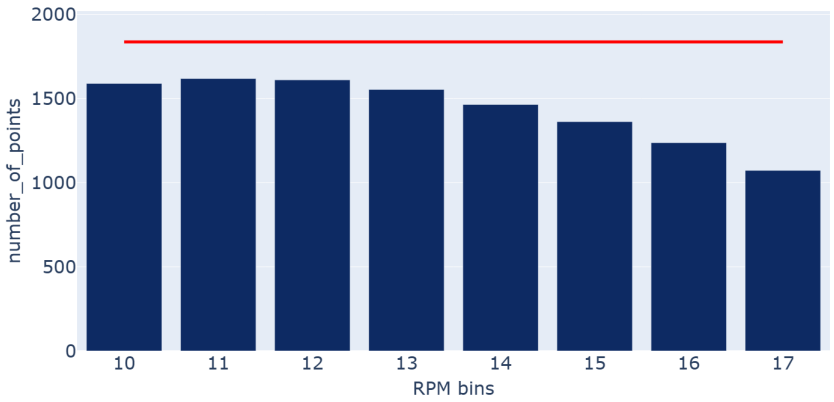

Figure A.27: Case Study 1 - $HI_{Res\_Baseline}$, $HI_{Res\_S\_M}$ at different RPMs, number of points

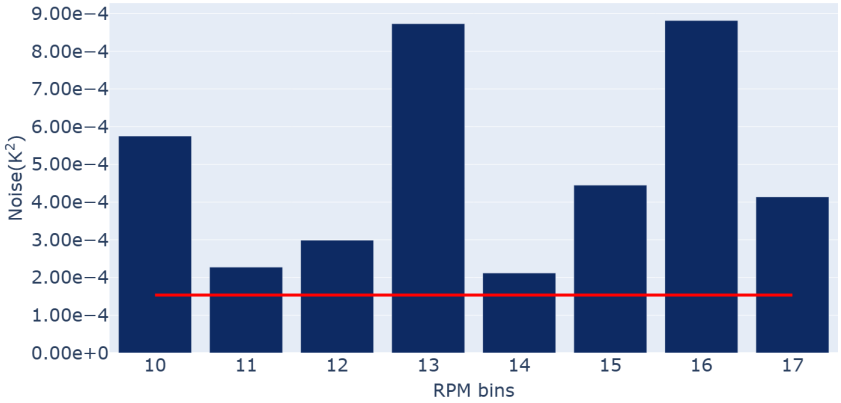

Figure A.28: Case Study 1- $HI_{Res\_Baseline}$, $HI_{Res\_S\_M}$ at different RPMs, dispersion comparison using Noise metric

In contrast, a comparison of the Noise metric shows that the binned HIs are more dispersed than $HI_{Res\_Baseline}$, as seen in Figure A.28. Gaps and a reduced amount of samples when considering only certain RPM throughout five years lead to outliers in obtained binned HIs. These gaps and outliers influence CEEMDAN decomposition and lead to high noise values for obtained HIs. As an example, $HI_{Res\_S\_M\_B}$ of 13 RPM bin are shown in Figure A.29 to demonstrate gaps present in the time series when considering only certain RPM.

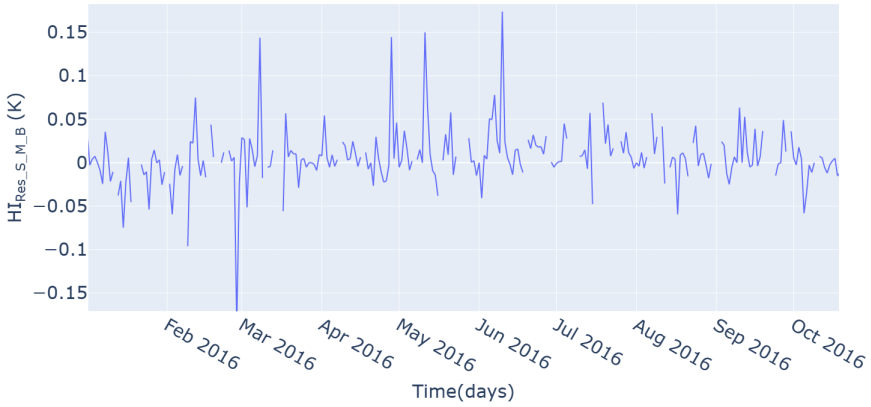

Figure A.29: Case Study 1, Test set - Step S, Step M, and Step B HI zoomed-in view at 13 RPM , $HI_{Res\_S\_M\_B}$

The motivation for including step B is to consider variable operating conditions when analyzing the degradation trend. This case study demonstrates that binning the data does not significantly impact the level of monotonicity. Moreover, binning also introduces gaps and outliers in the data due to the reduced amount of samples considered. Thus, the step B can be described as not beneficial. However, looking at MK metrics of the operational RPM range, it was observed that trends are similar across certain RPM bins. Thus, it would be interesting to explore how monitoring a certain range of RPMs is beneficial compared to monitoring the whole time series.